On control and estimation problems in antilock braking systems

Missie María del Rocío Aguado Rojas

université PARIS-SACLAY

NNT : 2019SACLS103

Thèse de doctorat

UNIVERSITÉ PARIS SUD
Comprendre le monde, construire l'avenir

On Control and Estimation Problems in Antilock Braking Systems

Thèse de doctorat de l'Université Paris-Saclay
préparée à l'Université Paris-Sud

Ecole doctorale n°580 Sciences et Technologies de l'Information et de la Communication (STIC)
Spécialité de doctorat : Automatique

Thèse présentée et soutenue à Gif-sur-Yvette, le 14 juin 2019, par

MISSIE MARÍA DEL ROCÍO AGUADO ROJAS

Composition du Jury :

Christine Chevallereau Directeur de Recherche, CNRS (Laboratoire des Sciences du Numérique de Nantes)	Présidente
Ilya Kolmanovsky Professeur, University of Michigan (Department of Aerospace Engineering)	Rapporteur
Sergio M. Savaresi Professeur, Politecnico di Milano (Dipartimento di Elettronica e Informazione)	Rapporteur
Françoise Lamnabhi-Lagarrigue Directeur de Recherche, CNRS (Laboratoire des Signaux et Systèmes)	Examinatrice
Jean-Claude Vivalda Directeur de Recherche, INRIA (Institut Élie Cartan de Lorraine)	Examinateur
Qinghua Zhang Directeur de Recherche, INRIA (Inférence Statistique pour la Surveillance et la Sécurité des Structures)	Examinateur
William Pasillas-Lépine Chargé de Recherche, CNRS (Laboratoire des Signaux et Systèmes)	Directeur de thèse
Antonio Loría Directeur de Recherche, CNRS (Laboratoire des Signaux et Systèmes)	Co-directeur de thèse

To my mom, my dad, and my little brother
(and my other two brothers as well).

Acknowledgements

I would like to express my deepest respect and most sincere gratitude to William Pasillas-Lépine and Antonio Loría. I am very lucky to have come across two people who are not only brilliant, passionate, and thorough researchers, but who are also really kind and good-hearted human beings. I could not have asked for better supervisors. Thank you for your guidance, support, patience, encouragement, and motivation, for all the witty jokes, for always making yourselves available to me, and for making me feel welcome in your offices and in your home.

Along the same lines, I would like to express my sincere appreciation to Elena Panteley, who has been always affable and kind to me, and who has often offered disinterested advice to help me along the way.

I owe special thanks and a great debt to Paul Maya, without whose friendship and support I would have probably never made it to the PhD.

I thank Alexandre de Bernardinis for the fruitful collaboration and his help in performing many of the experiments presented in this thesis.

I thank the Mexican *Consejo Nacional de Ciencia y Tecnología* (CONACYT) and *Secretaría de Educación Pública* (SEP) for funding this thesis.

I thank my L2Sian friends: Pablo, Rafa, Juan, Mohamed, and Mattia for creating such a nice work environment, for guiding me through our university's Kafkaesque administrative procedures, and for sharing with me all those great moments within and outside the L2S.

Finally, but most importantly, I thank my family —those who travelled more than 9000 km to attend my 45-minute presentation, and those who were not able to travel but wished they had attended as well— for being *my* amazing family.

To all of you, thank you / gracias / merci.

Missie Aguado
Gif-sur-Yvette, July 2019

Contents

1 Introduction

1.1 Background and motivation

Road accidents constitute an important public health and development problem with significant socioeconomic costs. According to the World Health Organization [126], more than 1.35 million people worldwide die on the road each year, and as many as 50 million more sustain serious injuries and live with long-term adverse health consequences. An ambitious target to reduce these numbers by 50% by 2020 was set in the context of the 2030 Agenda for Sustainable Development. The key measures to be implemented towards achieving the target include [125]: to establish and enforce speed limits and other traffic laws, to provide safe infrastructure for all road users, and to establish and enforce regulations on motor vehicle safety standards. Universal deployment of improved vehicle safety technologies for both passive and active safety is encouraged, with an emphasis on crash avoidance technologies with proven effectiveness, such as the antilock braking system (ABS).

Introduced by Bosch in 1978 for production passenger cars, the ABS is the core of today's active safety systems. Its working principle is simple. In an emergency braking situation caused, for example, by abrupt reactions from the driver due to an unexpected hazard, or even when driving on wet or slippery road surfaces, the brake force applied by the driver might be greater than what the tyre can handle thereby causing the wheels to lock up. Consequently, the tyres can no longer transfer lateral traction forces and the vehicle becomes unstable and uncontrollable since it no longer reacts to the steering input of the driver. In contrast to this, in a vehicle equipped with an ABS, wheel-speed sensors measure the angular speed of the wheels and pass this information to the ABS control unit. If the latter detects that one or more wheels tend to lock, it intervenes within milliseconds by modulating the braking pressure at each individual wheel. In doing so, the ABS prevents the wheels from locking and ensures safer braking while preserving stability and steerability of the vehicle. Generally, the stopping distance is also reduced.

This thesis addresses three problems related to the ABS in the context of the wheel dynamics: the estimation of the tyre extended braking stiffness (XBS) during an emergency braking situation, the control of the ABS based on the estimation of the XBS, and the estimation of the angular velocity and acceleration of the wheel from the measurements of an incremental encoder with imperfections. The general objective of this work is to develop tools aimed at improving

the performance of braking systems by using techniques adapted from nonlinear control theory. A brief description of the results obtained on each of these problems is presented in the following section.

1.2 Overview and contributions of the thesis

1.2.1 Extended braking stiffness estimation

As vehicle safety-oriented control systems become more advanced, their dependence on accurate information on the state of the vehicle and its surroundings increases. For instance, the performance of driver-assistance technologies such as the ABS is greatly influenced by the characteristics of the friction force between the tyre and the road. Therefore, by taking into account the external driving conditions of the vehicle, the effectiveness of such active safety systems can be greatly improved [1]. Tyre-road friction, however, cannot be directly measured in real-time; hence its estimation has been an intensive research area in the last years. Numerous different approaches to estimate the tyre-road friction coefficient and its maximum value have been proposed in the literature —see, e.g. [80, 92], and references therein. In several of these works it is proposed to estimate the peak tyre-road friction under the premise that the tyre braking stiffness indicates the peak value of the friction-slip curve [14]. The braking stiffness is the slope of the friction with respect to the wheel slip at the zero-slip operating point [33]. In this thesis we are interested in a generalization of this concept known as *extended braking stiffness* (XBS), which may be defined as the slope of the friction-slip curve at *any* operating point —see [111] and [118].

The interest of estimating the XBS stems from its potential for improving the design of ABS control algorithms. In contrast to the optimal value of wheel slip (the value for which the maximum friction coefficient is attained), which depends on the road conditions and is usually unknown, the optimal value of XBS is always known and equal to zero. The estimation of this variable could serve, for example, to perform closed-loop wheel acceleration control in order to improve the robustness of the ABS with respect to changes in the road conditions. It could also serve to design an ABS control algorithm in order to maintain the XBS in a neighbourhood around zero.

Contributions of this thesis

The first part of this manuscript focuses on the construction of an adaptive observer for the XBS. We start from a model of the wheel acceleration dynamics introduced in [41] in which the XBS appears as one of the state variables and that is, in turn, based on Burckhardt's friction model [12]; it is assumed that the parameters in this model that are related to the road conditions are constant but unknown. The system's measured output is defined as the difference between the longitudinal acceleration of the vehicle and the wheel's. The vehicle speed is assumed to be known and considered as an external variable of the model.

To design the observer, we first introduce a change of coordinates that renders the system linear in the unknown parameters and thus allows us to use observer design methods that are available for this type of systems. Then, inspired from the works of Zhang [129] and Hoàng et al. [41], we introduce a switched adaptive observer, that is, an adaptive observer whose estimation gains switch between two possible values based on the sign of the system's measured output. This choice allows us to analyze the stability properties of the observer in a transformed time-scale, wherein the dynamics of the observation error can be regarded as a switched system. We establish sufficient conditions on the observer gains which guarantee that for the dynamics of the observation error the origin is asymptotically stable, provided that the switching signal (the sign of the system's measured output) has a minimal dwell-time. Moreover, we establish conditions guaranteeing that the time-scale transformation, which is a function of the speed of the vehicle and the output of the system, is well defined. Furthermore, we show that if there exists a minimal dwell-time in the original time-scale, then there also exists a minimal dwell-time in the transformed time-scale. These conditions are summarized in the form of assumptions that we consider reasonable during an ABS braking situation: the first one is that the speed of the vehicle is positive, bounded, and separated from zero; the second one is that the output of the system is persistently exciting, crosses zero only at isolated points, and any two such points are separated by a minimal positive time interval.

The performance of the proposed observer has been tested on experimental data acquired from a tyre-in-the-loop test rig during the evaluation of ABS strategies. The test rig consists of a 2.5 m diameter steel drum that rotates on its axis in order to emulate the displacement of the vehicle and a tyre rolling on top of the drum. The results show that the adaptive observer is more robust to measurement noise and provides a better estimation of the XBS than the previous approaches. We have tested the performance of the observer under changes in the road conditions (a perturbation that cannot be implemented in the test rig) via numerical simulations. To that end, we employ a two-axle vehicle model that includes phenomena that were neglected during the design stage, such as the suspension dynamics, load transfer, and tyre relaxation length. Furthermore, we consider that the vehicle speed is estimated from the measurements of the angular velocities of the wheels and the longitudinal acceleration of the vehicle. The results show that even if the speed of the vehicle is underestimated by 20%, the observer still provides a reasonable estimation of the XBS. Notably, the zero-crossing of the estimate coincides with that of the real XBS, which is important because the observer is able to properly detect when the system transitions from one region of the tyre to the other. In the second part of the thesis, we employ this feature to reformulate the (control) objective of the ABS in terms of the XBS.

The results described in this section were partially presented in the articles [C.3] and [J.2] listed in Section 1.3, farther below.

1.2.2 ABS CONTROL BASED ON XBS ESTIMATION

The main objectives of the ABS are to prevent the wheels from locking in order to maintain the stability and steerability of the vehicle during heavy braking, and to maximally exploit the tyre-road friction coefficient in order to achieve the shortest possible braking distance [18, 108]. Most commercial ABS use a regulation logic based on wheel deceleration thresholds (see, e.g. [57, 31, 94]). The principle of these algorithms is based on generating limit cycles in a desired range of longitudinal wheel slip. The main force of these controllers is that they are able to keep wheel slip in a neighborhood of the optimal point without using explicitly its value and they are robust with respect to changes in tyre parameters and road conditions. Their main drawback, however, is that they are often based on purely heuristic arguments and the tuning of the deceleration thresholds is not an easy task [15]. Moreover, the wheel-slip cycling range cannot be explicitly chosen; instead, it has to be selected indirectly through the wheel deceleration thresholds. Our goal is thus to design an ABS algorithm that allows the cycling range to be chosen in a more direct manner.

CONTRIBUTIONS OF THIS THESIS

The second part of the thesis is dedicated to the design of an ABS control algorithm based on the estimation of the XBS. We first design a continuous controller whose objective is to regulate the system to the origin. We illustrate via numerical simulations that when the output of the system converges towards zero, it does not satisfy the persistency of excitation condition and the trajectories of the observer do not converge to the real trajectories of the system. To circumvent this issue, we then design a hybrid control algorithm in which the reference for the acceleration of the wheel switches depending on the value of the XBS. The objective is to make the system converge to a limit cycle around the origin so that the system's trajectories satisfy the persistency of excitation condition. The algorithm has two phases. We assume that the initial conditions of the system are such that the wheel acceleration and the XBS are negative, that is, the system has entered the unstable region of the tyre; if it goes too far into this region, the wheel will lock down. During the first phase the reference of the wheel acceleration is set to a positive value; the aim is to make the wheel return to the stable region of the tyre. Once the acceleration becomes positive, the XBS starts to increase until it crosses a certain threshold that triggers the activation of phase 2. During the second phase the reference of the wheel acceleration is set to a negative value; the aim is to prevent the wheel from going too far into the stable region, as it would result in a loss of friction force and thus in an increase of the braking distance. After the change in the sign of the acceleration, the wheel returns into the unstable region of the tyre. The XBS stars to decrease until it crosses a threshold that triggers again the activation of phase 1.

To analyze the stability of the obtained limit cycle, we make use of Poincaré's first return map, that transforms the analysis of periodic orbits of a system into the analysis of fixed points of a map. In this first stage, we neglect the dynamics

of the observer and consider that the XBS is known. To construct the first return map we take the transition at which phase 1 is triggered as the equivalent of a transverse section. Based on this analysis we obtain sufficient conditions to guarantee the asymptotic stability of the limit cycle.

The performance of the hybrid control algorithm has been tested via numerical simulations. The results confirm the asymptotic stability of the limit cycle for the case in which the XBS is known. Moreover, for the case in which the switched adaptive observer is used to estimate the XBS, the system's trajectories satisfy the persistency of excitation condition, hence the XBS is correctly estimated and the closed-loop system achieves a good performance during braking. The stability analysis of the limit cycle including the observer dynamics will be developed in future works.

The results described in this section were partially presented in the article [C.4] listed in Section 1.3.

1.2.3 Angular velocity and acceleration estimation

In the design of the XBS observer and the ABS controller previously discussed, it is assumed that the angular velocity and the angular acceleration of the wheel are measured. Although this assumption holds in vehicles equipped with ABS, in practice some issues related to these measurements ought to be taken into account. The most commonly used technology to measure rotational velocity and acceleration is based on incremental encoders (see, e.g. [24, § 6.2]). They consist, mainly, in a toothed wheel (or a slotted disc) attached to the rotating shaft and a fixed pick-off sensor that detects the passing of the teeth and outputs a square wave signal in which each edge corresponds to the edge of one tooth. An ideal encoder is characterized by identical and equidistant teeth (or slits) distributed over the encoder's code-track. Real encoders, however, are subject to imperfections such as non-identical or non-equidistant teeth, and eccentricity of the code-track with respect to the rotating shaft. These imperfections introduce variations in the locations of the edges of the output pulses that can be can be modelled as two independent additive perturbations —see [51, 52, 53]. When viewed over the circumference of the encoder's code-track, non-ideal teeth produce random high-frequency variations, whereas eccentricity of the code-track produces a systematic low-frequency variation. Moreover, because the error caused by sensor imperfections is periodic in one mechanical revolution, the measurements of velocity and acceleration contain periodic perturbations whose frequency coincides with that of the rotating shaft. The literature review on the subject of the removal of these perturbations shows that, even though the encoder imperfections are well known, only a small number of approaches using real-time filters have been proposed, all in the context of vehicle control. All these works propose the use of a notch filter to attenuate the first harmonic component of the perturbations.

The third part of this manuscript focuses on the construction of an algorithm for estimating the angular velocity and acceleration of the wheel capable of removing the perturbations caused by the encoder imperfections. First, we introduce three models that capture the effects of sensor imperfections on the measured signals. Our analysis shows that even if the error present in the measured position may be neglected depending on the application, such is not the case for the other signals. Notably, the measured velocity contains an error term that is proportional to the real velocity, whereas the measured acceleration contains an error term that is proportional to the real acceleration and another one that is proportional to the square of the real velocity. By combining these models with the features of the method known as time-stamping algorithm, we propose a three-stage algorithm to identify and remove the periodical perturbations introduced by the encoder imperfections. In contrast to the previous works, in which only the first harmonic component of the perturbations is filtered out, the aim of our approach is to identify a given number of harmonic components and to use that information to recover more reliable estimates of the velocity and acceleration of the shaft. In the first stage we use a high-pass filter to separate the high-frequency perturbations from the real signals. By using the three models previously introduced and the least-squares recursive algorithm, in the second stage we identify the parameters that describe the output of the first stage. In the third stage we use the identified parameters to construct our estimations.

The estimation algorithm was tested using an experimental setup composed by two synchronous motors coupled via a torque transducer and a 60 pulses-per-revolution encoder, and a second encoder of 1024 pulses-per-revolution attached to the same shaft that is used as reference. The results show that our algorithm is able to reduce significantly the amplitude of the harmonic components caused by sensor imperfections and does not introduce noticeable phase-lags, as opposed to a notch filter with which only the first harmonic component is significantly reduced and that can introduce an important phase-lag depending on the filter's damping ratio. With the proposed method, using a low-resolution encoder it is possible to obtain smoother signals and similar to those obtained using a high-resolution encoder.

The results described in this section were presented in the articles [C.1], [C.2], and [J.1] listed in the next section.

1.3 RELATED PUBLICATIONS

This section lists the publications written in the framework of this thesis.

JOURNAL ARTICLES

[J.1] M. Aguado-Rojas, W. Pasillas-Lépine, A. Loría, and A. De Bernardinis. Acceleration estimation using imperfect incremental encoders in automotive applications. *IEEE Transactions on Control Systems Technology*. In press. DOI: 10.1109/TCST.2019.2896199.

[J.2] M. Aguado-Rojas, W. Pasillas-Lépine, and A. Loría. Extended-braking-stiffness estimation under varying road-adherence conditions. *IEEE Transactions on Control Systems Technology*. In press. DOI: 10.1109/TCST.2019.2918483.

CONFERENCE ARTICLES

[C.1] M. Aguado-Rojas, W. Pasillas-Lépine, A. Loría, and A. De Bernardinis. Angular velocity estimation from incremental encoder measurements in the presence of sensor imperfections. *IFAC-PapersOnLine*, Vol. 50, Issue 1, pp. 5979–5984, 2017.
Presented at the *20th IFAC World Congress* (Toulouse, France).
DOI: 10.1016/j.ifacol.2017.08.1260

[C.2] M. Aguado-Rojas, W. Pasillas-Lépine, A. Loría, and A. De Bernardinis. On the compensation of incremental encoder imperfections for motion control: a DC motor case-study. *IFAC-PapersOnLine*, Vol. 51, Issue 13, pp. 627–632, 2018.
Presented at the *2nd IFAC Conference on Modelling, Identification and Control of Nonlinear Systems* (Guadalajara, Mexico).
DOI: 10.1016/j.ifacol.2018.07.350

[C.3] M. Aguado-Rojas, W. Pasillas-Lépine, and A. Loría. A switched adaptive observer for extended braking stiffness estimation. *2018 Annual American Control Conference* (Milwaukee, USA), pp. 6323–6328.
DOI: 10.23919/ACC.2018.8430681

[C.4] M. Aguado-Rojas, W. Pasillas-Lépine, and A. Loría. A hybrid controller for ABS based on extended-braking-stiffness estimation. *9th IFAC Symposium on Advances in Automotive Control* (Orleans, France), 2019. In press.

1.4 ORGANIZATION OF THE MANUSCRIPT

The rest of the manuscript is organized in two parts. The first one addresses the estimation of the XBS and the related ABS control algorithm. The second part addresses the estimation of the angular velocity and acceleration of the wheel.

PART I

Chapter 2 provides an introduction to the ABS and its principle of operation. The quarter-car model is presented, followed by a simplified version of it which describes the wheel dynamics during an ABS braking maneuver. Based on

this simplified model and on Burckhardt's tyre-road friction coefficient, a third model which describes the wheel dynamics in terms of the XBS is then presented. The chapter concludes with a literature review on the estimation of the XBS.

Chapter 3 contains our contributions on the estimation of the XBS. In this chapter are presented: the change of coordinates that renders the system linear in the unknown parameters, the switched adaptive observer, the stability analysis of the observer under known and unknown parameters, the analysis of the well-posedness of the time-scale transformation and the existence of a minimal dwell-time, simulation results considering the single-wheel system, experimental results, and simulation results considering a two-axle vehicle model.

Chapter 4 contains our contributions on the control of ABS based on the XBS estimation. This chapter includes: the design of a continuous control algorithm, simulations results to show that the system might not be persistently exciting when using a continuous control algorithm, the design of the hybrid control algorithm, the stability analysis of the limit cycle considering known XBS, and simulation results considering the single-wheel system with and without XBS estimation.

PART II

Chapter 5 provides an introduction to incremental encoders and their imperfections. First, a general description of the encoders used in the ABS is presented, followed by the algorithm employed in this work to reconstruct angular velocity and acceleration from the measurements of an incremental encoder. The most common encoder imperfections are then described and their effects modelled. Experimental results to illustrate the effects of encoder imperfections are presented as well. The chapter concludes with a literature review on the compensation of encoder imperfections.

Chapter 6 contains our contributions on the compensation of encoder imperfections. This chapter includes: the development of three models that capture the effects of sensor imperfections on the measured signals, the three-stage estimation algorithm, experimental results, and simulation results of the use of the estimation algorithm in closed-loop with an ABS control algorithm.

Chapter 7 contains some concluding remarks of this work and recommendations for future work.

Appendices A and B provide an introduction to some of the tools employed in this work, namely, the Poincaré map and the Lambert W function. Appendix C discusses some implementation aspects related to Part II of this thesis.

Part I

Extended-braking-stiffness estimation and ABS control

2 PRELIMINARIES ON WHEEL DYNAMICS AND THE ABS

In this chapter we introduce the ABS and present the model used in this thesis to describe the braking dynamics. We present as well a literature review on the topics addressed in the first part of this thesis, namely, on the estimation of the extended braking stiffness and on control algorithms for the ABS.

2.1 WHEEL DYNAMICS

To describe the vehicle braking dynamics, let us present a simple quarter-car model (also called single-corner model) that considers only the forces acting on the longitudinal direction. Despite its simplicity, this model is widely encountered in the literature of active braking control systems, as it is known to provide a simple, yet sufficiently rich, description of the braking dynamics [101, § 2.3]. Moreover, even though load transfer and combined slip are ignored, all the basic phenomena related to ABS already appear in the model and the predicted limit cycles are considerably close to those obtained using more realistic models or experimental setups (cf. [31]).

The quarter-car model is composed of a wheel with angular velocity ω and a vehicle with longitudinal velocity v_x. The dynamics of the system is described by

$$J\dot{\omega} = -RF_x + T \tag{2.1a}$$

$$m\dot{v}_x = F_x, \tag{2.1b}$$

where J is the rotational inertia of the wheel, R is its effective rolling radius[1], F_x is the longitudinal tyre-road friction (or contact) force, m is the single-corner mass, and $T = T_e - T_b$ is the torque applied to the wheel, composed by the engine torque T_e and the brake torque T_b. In what follows it is assumed that the clutch is open during an ABS braking maneuver so the engine torque can be neglected. The brake torque is modelled as $T_b = \gamma_b P_b$, where γ_b is an overall braking system gain known as the brake efficiency and P_b denotes the brake pressure.

[1] See [10, § 5.2.2] for the definition of the tyre radii.

The longitudinal friction force F_x is modelled as

$$F_x = F_z\,\mu(\lambda),$$

where F_z is the tyre normal load and $\mu(\lambda)$ denotes the tyre-road friction (or adhesion) coefficient, which describes the tyre capability of transferring the vertical load to the ground. It depends nonlinearly on the longitudinal wheel slip λ defined as

$$\lambda = \frac{R\omega - v_x}{v_x},$$

which denotes the normalized relative velocity between the vehicle (with longitudinal speed v_x) and the wheel (with linear speed $R\omega$ at the wheel-ground contact point). A zero slip corresponds to a pure rolling wheel, while the presence of a non-zero slip is due, in general, to traction and braking forces exerted on the tyre. In particular, the region $\lambda < 0$ corresponds to braking and the region $\lambda > 0$ corresponds to traction. The point $\lambda = -1$ represents a locked wheel.

The typical behavior of the tyre-road friction coefficient is shown in Fig. 2.1. It is a smooth function, symmetric about the origin, that satisfies $\mu(0) = 0$ and $\frac{\mathrm{d}\mu(0)}{\mathrm{d}\lambda} > 0$. It has a single maximum at $\lambda = \lambda^*$ and hence a single minimum at $\lambda = -\lambda^*$. The part of the curve with positive slope is called the stable region of the tyre and the part with negative slope is called the unstable region —see [109]. When braking in the stable zone of the tyre, the wheel deceleration is limited to relatively low rates so that when the driver presses harder on the brake pedal, the vehicle brakes harder without the wheels locking up. In the unstable zone, however, the driver only needs to apply slightly more pressure to the brake pedal to induce instantaneous wheel lock-up. Note that for $\lambda = 0$ (pure rolling wheel) no longitudinal force can be transmitted to the ground, while for $\lambda = -1$ (locked wheel) there is a loss of longitudinal force of up to 20–30% with respect to the peak value.[2]

Several models of the tyre-road friction coefficient are available in the literature —see, e.g. [66] and references therein. In general, they can be classified into empirical and analytical models. Empirical (also called static or pseudo-static) models are derived heuristically from experimental data based on curve-fitting techniques. They usually formulate the tyre-road friction characteristics through a function of μ in terms, mainly, of λ, and in some cases, v_x and F_z. In this category, one can find approaches based on piecewise linear functions (see, e.g. [84, 62] and [94, p. 79]), exponential functions [12, 2], polynomials [55] and rational fractions [56, 89], and trigonometric functions [85, § 4.3]. Analytical (also called dynamic) models describe the tyre-road friction characteristics through differential equations. They attempt to capture transient phenomena

[2]Because we are interested in the braking dynamics, in this work we focus on the region $\lambda < 0$. Hence, in what follows we designate the minimum at $\lambda = -\lambda^*$ as the optimal operating point and —with an abuse of language— we refer to the friction $\mu(-\lambda^*)$ as the *maximum* friction (during braking) and to the corresponding tyre force $F_x = F_z\,\mu(-\lambda^*)$ as the *maximum* (braking) force.

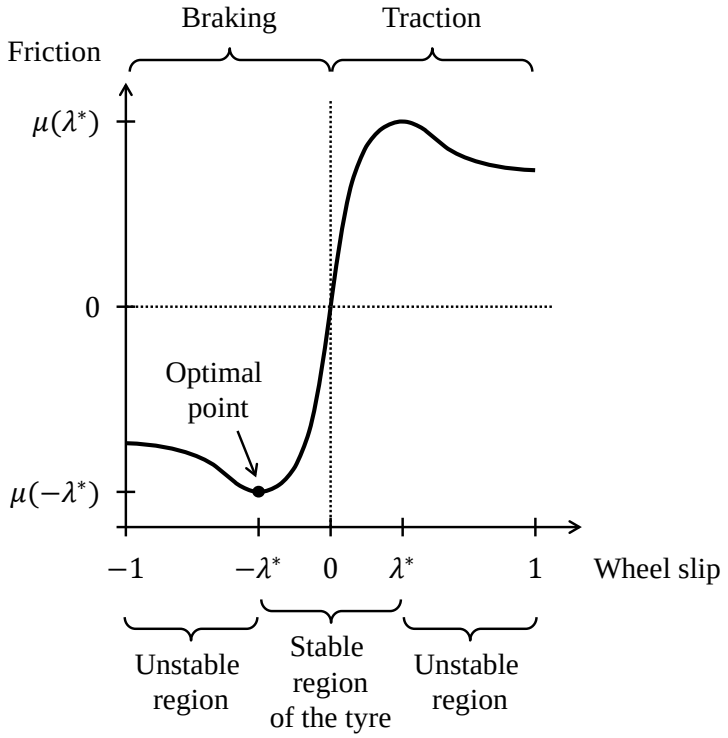

Figure 2.1: Typical shape of the friction-vs-slip curve.

such as hysteresis and the Stribeck effect. Some of the most well-known models in this category are the Dahl model [22], the Bliman-Sorine model [9], and the LuGre model [13, 25]. In this work, Burckhardt's empirical model based on exponential functions will be used.

2.2 Overview of the antilock braking system

2.2.1 History

In August 1978 Daimler-Benz presented to the press its market-ready *Anti-Blockier-System* (wherefrom the acronym ABS was coined), which was developed in collaboration with Bosch and introduced in their Mercedes W116 S-Class sedans [23]. This event represented a milestone in the development of automotive technologies and is usually acknowledged as the beginning of the *modern age* of ABS. Nevertheless, the development of the ABS can be traced back several decades.

As early as 1928, a German engineer named Karl Wessel registered a patent for a mechanical braking force regulator for automobiles [123], but it did not get beyond the drawing-board stage. According to [6], Wessel offered the patent to Bosch but the company, preferring to develop a system of its own, in 1936 filed in a patent for a "mechanism to prevent locking of the wheels of a motor vehicle" [107]. The device, however, never reached the production line. In the following years, antiskid brake systems were successfully deployed in other

areas of engineering. In the aviation industry, for example, Crane introduced in 1947 the Hydro-Aire Hytrol Mark I antiskid system developed for the Boeing/USAF B-47 [78]. In the railway industry, Knorr-Bremse introduced in 1953 its KE brake [58], which regulated the braking force by varying the air pressure in the brake cylinder, that led to the development of the Wheel Slide Protection system for rail vehicles, which is analogous to the ABS for automobiles. The transfer of these technologies to passenger cars, however, proved to be significantly more difficult than expected because the demands on the sensors and the signal-processing were much higher for cars than for airplanes or trains [23].

In the early 1950s, the British Road Research Laboratory attempted to retrofit the Dunlop Maxaret antiskid system from airplanes to automobiles, but it was until 1966 that the device reached the market. One of the most famous installations of the automobile Maxaret was on the Jensen FF sportscar. The system effectively prevented wheel lock-up, but it was prohibitively expensive [49]. Meanwhile, during the 1960s and early 1970s, several precursors of the ABS were developed in partnership between brake producers and automobile manufacturers: Kelsey-Hayes partnered with Ford, Bendix with Chrysler, Alfred Teves with BMW, Bendix-DBA with Citröen, and Teldix with Daimler-Benz. These systems used analogue computers and vacuum-actuated modulators which cycled very slowly. Hence, even though the level of safety and the lateral stability of the vehicle improved, the actual stopping distance was significantly increased [101, § 1.2].

It was not until digital technology became available in the 1970s that a reliable ABS could be developed. In 1975 Bosch acquired Teldix and, three years later, revolutionized braking systems with the use of digital electronics and microprocessors. When "the first electronic four-wheel multi-channel anti-lock brake system" was finally presented by Daimler-Benz and Bosch in 1978, it became the benchmark for subsequent generations of antilock braking systems [48].

2.2.2 How does it work?

The ABS (see [94, pp. 74–93] and [74, § 30.1.3]) is based on three components besides those of the conventional braking system: the wheel-speed sensors, the electronic control unit, and the hydraulic modulator. The wheel-speed sensors convert the angular displacement of the wheels into electrical signals which are continuously transmitted to the control unit. Based on these signals, the electronic control unit determines the angular velocity and acceleration/deceleration of the wheels and it calculates an approximation of the wheel slip in order to detect whether any of the wheels is about to lock up. If imminent wheel-locking is detected, the electronic control unit regulates the brake pressure of the concerned wheel via the hydraulic modulator.

The hydraulic modulator incorporates a series of solenoid valves that can open or close the hydraulic circuits between the master cylinder and the brakes. There is one pair of valves for each brake: an inlet valve between the master cylinder and the brake that controls pressure application, and an outlet valve

between the brake and the return pump that controls pressure release. Depending on their position, the solenoid valves can take one of three settings:

- Apply pressure: the inlet valve is open, hence the brake pressure generated in the master cylinder when the brakes are applied is transmitted directly to the brakes at each wheel. This setting corresponds to a normal braking situation.
- Hold pressure: if the wheel slip increases so that the wheel tends to lock-up, then the inlet valve is closed. The connection between the master cylinder and the brakes is shut off so that any increase of pressure in the master cylinder (should the driver push the brake further) does not lead to an increase of pressure at the brakes.
- Release pressure: if the wheel slip further increases despite the previous setting, then the outlet valve is opened while the inlet valve is still closed. This allows the return pump to draw brake fluid from the brakes in a controlled manner and thus reduce the pressure at the brakes to avoid wheel lock-up.

Note, from the description of the above settings, that the ABS cannot actively increase the brake pressure. That is, the brake pressure at the wheels can only be as large as that generated by the driver. It should be noted as well that, even though the hydraulic modulator can only take three settings, the rate of the pressure increase/decrease can be controlled by actuating the valves using pulse-width-modulation techniques.

2.2.3 TYPICAL CONTROL CYCLES

The typical control cycles of the Bosch ABS are illustrated in Fig. 2.2. The graphics show the behaviour of the longitudinal speed of the vehicle 'v_{F}', the linear speed of the tyre 'v_{R}', the wheel acceleration, and the brake pressure when the ABS sequence is activated on a high-adherence road surface. The different phases are activated by the wheel acceleration/deceleration thresholds '$-a$', '$+a$', and '$+A$', and the slip threshold 'λ_1'. This notation is used here in order to keep consistency with the original reference [94]. It should be noted, however, that the values of the thresholds are independent from each other and '$-a$' is not the opposite of '$+a$'.

The evolution of the cycles is as follows. During the initial stage of braking (phase 1) the hydraulic modulator is on the 'apply pressure' setting. Both the wheel and the vehicle decelerate as the driver increases the brake pressure. Meanwhile, by extrapolating the velocities of a diagonal pair of wheels (for example, the front-left and the rear-right wheels), the electronic control unit calculates a reference velocity 'v_{Ref}' which represents the velocity under ideal braking conditions. When the wheel deceleration crosses the threshold '$-a$' the hydraulic modulator switches to the 'hold pressure' setting (phase 2). At this point the pressure is kept constant and not immediately released because the threshold '$-a$' might have been exceeded within the stable region of the tyre (horizontal axle motions can falsely indicate that the wheel has entered the unstable region), hence a pressure reduction would cause potential brak-

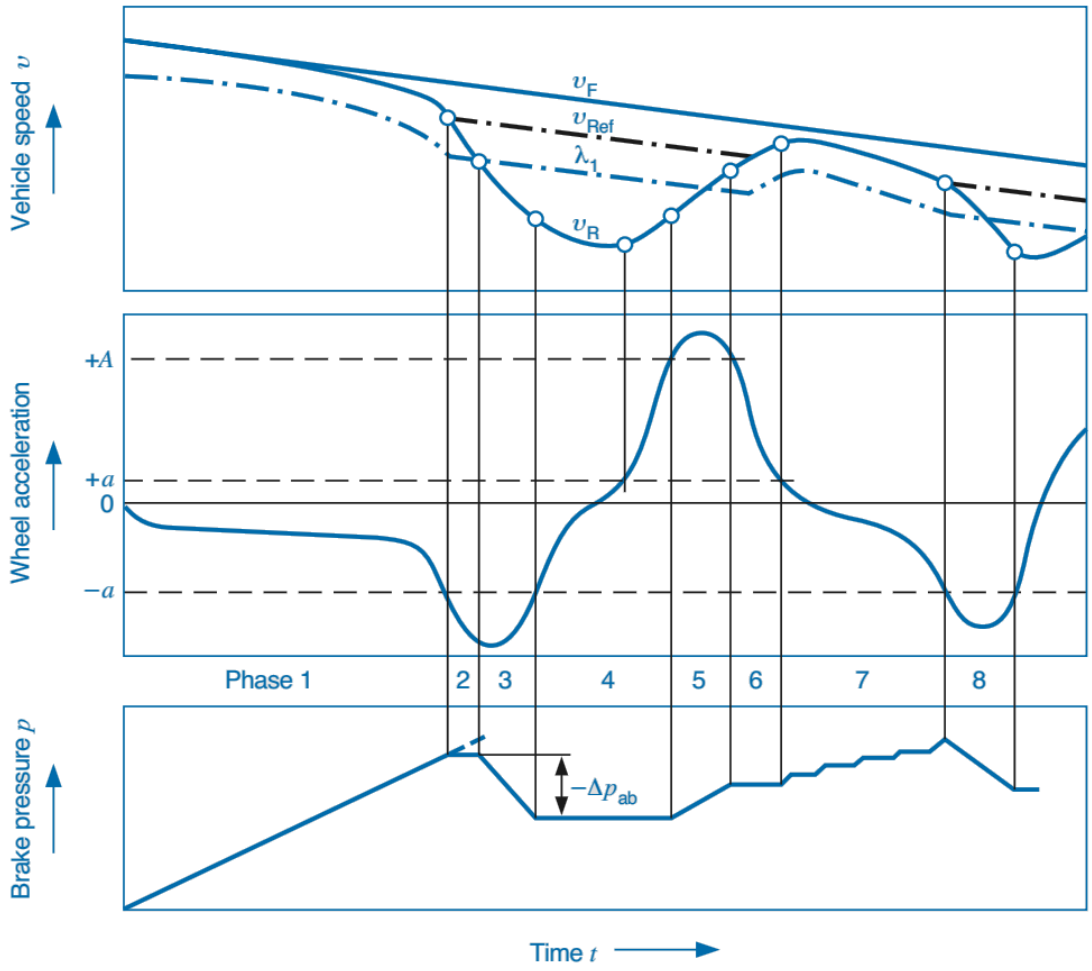

Figure 2.2: Typical control cycles of the ABS when braking on a high-adherence road surface. Source of illustration: [94, p. 82].

ing distance to be wasted. During this phase 'v_{Ref}' is reduced according to a defined linear gradient and is used for determining the threshold 'λ_1', which lies below the curve of 'v_{Ref}'. It is only after the wheel velocity has dropped below the threshold 'λ_1' that the hydraulic modulator switches to the 'release pressure' setting (phase 3). This setting is maintained for as long as the wheel deceleration remains below '$-a$'.

When the wheel deceleration crosses again the threshold '$-a$' the hydraulic modulator switches to the 'hold pressure' setting (phase 4). During this phase the wheel acceleration increases and becomes positive. When it crosses the relatively high threshold '$+A$' the hydraulic modulator switches to the 'apply pressure' setting (phase 5), which is maintained for as long as the wheel acceleration remains above '$+A$'. When the wheel acceleration crosses again the threshold '$+A$' the hydraulic modulator switches to the 'hold pressure' setting (phase 6). At the end of this phase the wheel acceleration drops below the threshold '$+a$', which indicates that the wheel has returned to the stable zone of the tyre and is now slightly underbraked. Hence, the brake pressure is increased again but slowly and in a stepwise manner (phase 7). This is done by appropriately alternating between the 'apply pressure' and the 'hold pressure' settings until the wheel acceleration drops below the threshold '$-a$' again. The idea behind the stepwise (and thus slow) increase in the brake pressure is to induce a slow increase of the wheel slip, so that the brake force stays close to its maximum value for some time. The second cycle of the ABS sequence starts when the wheel deceleration drops below the threshold '$-a$' at the end of this phase. At this point the hydraulic modulator switches directly to the 'release pressure' setting (phase 8, or second phase 3) without using a 'λ_1' threshold, as it is assumed that no "false alarms" (of the wheel entering the unstable region of the tyre) occur after the first cycle.

2.2.4 Literature review on ABS control algorithms

Since the introduction of the ABS, numerous control strategies for it have been proposed in the literature. They are usually classified in two main families, namely, wheel slip regulation controllers and logic-based switching controllers.

On the one hand, wheel slip controllers formulate the braking control as a classical regulation problem and they are often based on a clear mathematical background. Among this group, one can find approaches based on linearized models [102], nonlinear PI/PD/PID control [46, 113, 15], gain scheduling [47, 109], sliding modes [27, 120], Lyapunov-based designs [127, 3, 114, 90, 128], and fuzzy-learning techniques [63, 69].The main interest of these controllers is that, in order to regulate the wheel slip to a desired target, they apply a brake torque that converges to a specific value. That is, they avoid the oscillatory behavior of logic-based switching controllers and thus achieve shorter braking distances. Nevertheless, these approaches require accurate measurement or estimation of the vehicle speed in order to compute the wheel slip and they assume that the optimal value of the wheel slip is known (or estimated), conditions which are difficult to satisfy.

Logic-based switching controllers, on the other hand, make the system cycle around the optimal braking point by switching between different phases, each one associated with a certain control action. The main interest of these controllers is that, in general, they do not require measurements of the vehicle speed or the wheel slip, they do not assume knowledge of the optimal wheel slip, and they are robust with respect to changes in tyre parameters and road conditions. However, as a result of the oscillatory behaviour, they are not optimal in terms of the achieved braking distance and they may encounter problems when the tyre-road friction curve does not present a clear maximum.

Logic-based switching controllers can be divided in two subgroups depending on the variable used to trigger the different phases. The first subgroup comprises the controllers which are based mainly on wheel deceleration thresholds [94, 65, 62, 122, 89, 31, 20]. This type of controllers is the most widely used in today's commercial vehicles. Nevertheless, the main drawback of (most of) these approaches is that they are usually derived from purely heuristic arguments and include numerous special rules to handle different driving conditions, making it difficult to analyze their stability. Moreover, because the influence of the different parameters on the system's global performance is not always clear, they have poor interchangeability between different models of vehicles and their tuning has to be performed through extensive, costly, and time-consuming tests. The second subgroup gathers the controllers which employ thresholds that depend on variables other than the wheel deceleration, such as longitudinal friction force [18], brake torque and wheel slip [115], and brake torque [60]. By reformulating the control objective of the ABS in terms of such variables, these approaches provide a clear analysis of the behaviour of the system and yield conditions which guarantee the existence and asymptotic stability of the system's limit cycle. Their main drawback, however, is that they require the availability of additional sensors.

The ABS control algorithm developed in this work belongs to the second subgroup. Our approach, however, is based on an observer rather than on an additional sensor.

2.3 WHEEL SLIP AND ACCELERATION DYNAMICS

Define as state variables the wheel slip $x_1 = \lambda$ and the wheel acceleration offset

$$x_2 = R\dot{\omega} - a_x(t), \tag{2.2}$$

i.e. the difference between the linear acceleration of the tyre, $R\dot{\omega}$, and the longitudinal acceleration of the vehicle $a_x(t) = \dot{v}_x(t)$. The dynamics of x_1 and x_2 is described by

$$\begin{aligned}
\dot{x}_1 &= \frac{1}{v_x(t)}(-a_x(t)x_1 + x_2) \\
\dot{x}_2 &= -\frac{R^2}{J}F_z\frac{\mu'(x_1)}{v_x(t)}(-a_x(t)x_1 + x_2) - \frac{R}{J}\gamma_b\dot{P}_b - \dot{a}_x(t),
\end{aligned}$$

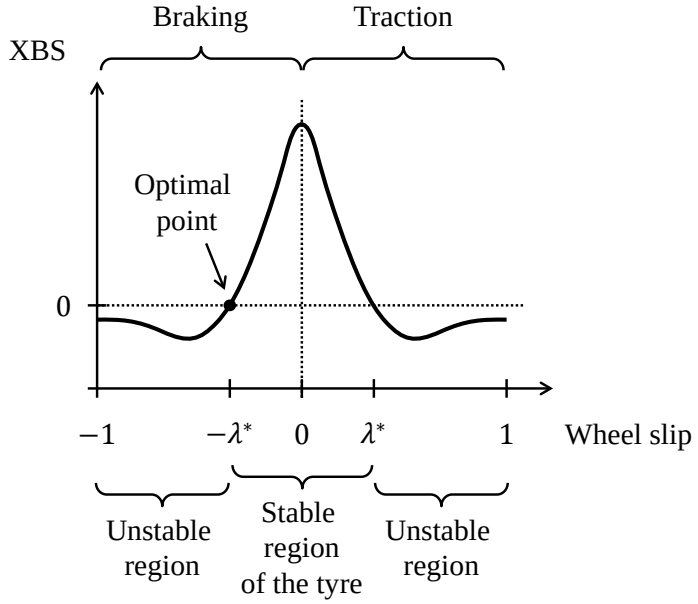

Figure 2.3: Typical shape of the XBS-vs-slip curve.

where $\mu'(\cdot)$ is called the tyre extended braking stiffness (XBS).

The XBS is defined as the slope of the tyre-road friction curve (Fig. 2.1) with respect to the wheel slip, i.e.

$$\mu'(\lambda) = \frac{\mathrm{d}\mu(\lambda)}{\mathrm{d}\lambda}.$$

It can be interpreted as a measure of the residual longitudinal friction available to the driver, hence it indicates whether the current slip is close to its optimal value. The typical shape of the XBS is illustrated in Fig. 2.3. Note that, in contrast to the maximum friction coefficient $\mu(\lambda^*)$, which depends on the road conditions and is usually unknown, the XBS that corresponds to the optimal wheel slip is always known and equal to zero, i.e. $\mu'(\lambda^*) = 0$.

From physical considerations, in what follows v_x is assumed to be positive, bounded, and separated from zero, i.e.

$$v_{x\min} \leq v_x(t) \leq v_{x\max}, \qquad \forall\, t \geq 0. \tag{2.3}$$

The first inequality above is justified by the fact that, according to certain manufacturers, if the wheels lock up below a minimum limit of approximately 2.5 km/h, the distance traveled before the vehicle comes to a halt is not critical [94, p. 76]. The second inequality, of course, is justified by physical constraints.[3]

During an ABS braking maneuver, the longitudinal acceleration of the vehicle remains almost constant and close to the maximal value a_x^* allowed by the road conditions, and the wheel slip remains relatively small. Under these conditions, the approximations $\dot{a}_x(t) \simeq 0$ and $(-a_x(t)x_1 + x_2) \simeq x_2$ are sensible.

[3]Interestingly, the current record for the maximum speed reached by a production vehicle is 447.19 km/h [59].

Road condition	c_1	c_2	c_3
Dry asphalt	1.2801	23.99	0.52
Wet asphalt	0.857	33.822	0.347
Dry concrete	1.1973	25.168	0.5373
Dry cobblestones	1.3713	6.4565	0.6691
Wet cobblestones	0.4004	33.708	0.1204
Snow	0.1946	94.129	0.0646
Ice	0.05	306.39	0

Table 2.1: Burckhardt's model parameters for various road surfaces [57, p. 322].

While the equalities are true only when $v_x(t)$ is constant, the approximations remain reasonable during the activation of the ABS. This leads to the simplified dynamics

$$\dot{x}_1 = \frac{1}{v_x(t)} x_2 \tag{2.4a}$$

$$\dot{x}_2 = -\frac{R^2}{J} F_z \frac{1}{v_x(t)} \mu'(x_1) x_2 - \frac{R}{J} \gamma_b \dot{P}_b, \tag{2.4b}$$

in which the longitudinal speed of the vehicle $v_x(t)$ is considered as an external variable of the model.

2.4 XBS DYNAMICS

Given a suitable choice for the tyre-road friction model, system (2.4) can be used to develop a simple second-order model in which the XBS appears directly as a state variable.

Here, the friction coefficient is described using the model proposed by Burckhardt [12]

$$\mu(\lambda) = c_1(1 - \exp(-c_2\lambda)) - c_3\lambda, \tag{2.5}$$

where the parameters c_1, c_2, and c_3 are "constants" that depend on the road conditions, on the tyre characteristics, and on the vehicle operational conditions. Hence, by changing the values of these three parameters, many different conditions can be modelled. Fig. 2.4 illustrates the shape of the curve $\mu(\lambda)$ obtained using the above model for different road conditions (only the region $\lambda > 0$ is shown). This model retains a good degree of accuracy in the description of the friction coefficient (cf. Fig. 2.1) and it is particularly suitable for analytical purposes [101, § 2.2.1].

To develop the model of the XBS dynamics let the wheel acceleration offset (2.2) and the XBS be defined as new state variables, that is,

$$z_1 = x_2$$
$$z_2 = \mu'(x_1).$$

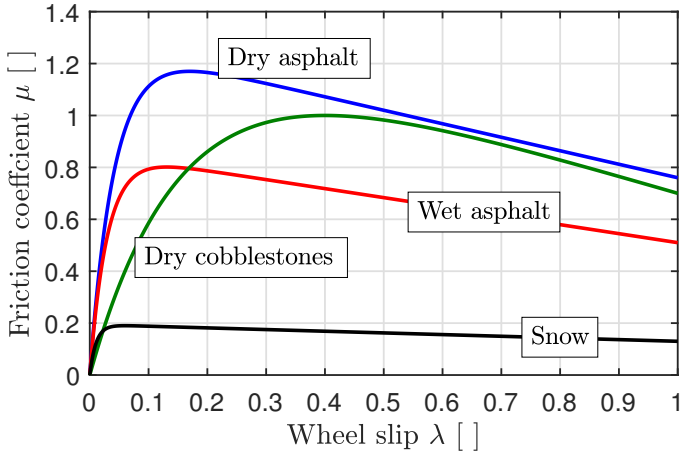

Figure 2.4: Typical tyre-road friction curves obtained using Burckhardt's model for different road surface conditions. The corresponding parameter values are given in Table 2.1. Note that for $\lambda > 0$ all the parameters are positive, whereas for $\lambda < 0$ the parameters c_1 and c_2 are negative and c_3 is positive.

From (2.5), recalling that $x_1 = \lambda$, we have

$$\mu'(x_1) = c_1 c_2 \exp(-c_2 x_1) - c_3$$
$$\mu''(x_1) = -c_2 c_1 c_2 \exp(-c_2 x_1)$$

from which the following relation can be established

$$\mu''(x_1) = -c_2 \mu'(x_1) - c_2 c_3.$$

The above relation, along with system (2.4), leads to the dynamics

$$\dot{z}_1 = -\frac{a}{v_x(t)} z_1 z_2 - bu \tag{2.6a}$$
$$\dot{z}_2 = (cz_2 + d)\frac{1}{v_x(t)} z_1, \tag{2.6b}$$

where $a = (R^2/J)F_z$ and $b = (R/J)\gamma_b$ are assumed to be known constant parameters, the control input $u = \dot{P}_b$ is the derivative of the brake pressure, and $c = -c_2$ and $d = -c_2 c_3$ are parameters that depend on the road conditions, thus they are assumed to be constant but unknown.

The vehicle speed $v_x(t)$ is considered as a known external variable that satisfies (2.3). The wheel acceleration offset defined in (2.2) can be computed from the measurements of the wheel angular acceleration and the vehicle longitudinal acceleration. Hence, z_1 is regarded as the system's measured output. Moreover, from physical considerations, it is assumed that u is bounded and it is such that the state trajectories of (2.6) are bounded. The first objective of this thesis is to design an observer to estimate the (unmeasurable) XBS, z_2, under unknown road conditions from the measurements of the wheel acceleration offset, z_1. To put our contribution in perspective we give first, in Section 2.5, a short account of the state of the art. Our main results are presented in Chapter 3.

2.5 LITERATURE REVIEW ON XBS ESTIMATION

The concept of maximizing the braking force in an ABS based on the slope of the braking force with respect to the wheel slip was first introduced by Sugai et al. in [111], where the XBS is identified by forcing a vibration via the brake actuator and analyzing the frequency characteristics of a resonance system composed of the vehicle body, the wheel and the road surface. The term *extended braking stiffness* was later coined by Umeno et al. in [119], where the XBS is estimated via the instrumental variable method based on the frequency characteristics of a tyre vibration model linearized around a constant-velocity operating point. In [83], the XBS is (implicitly) assumed to be a constant parameter and estimated by applying the recursive least squares algorithm to wheel rotational velocities. In [121], in order to estimate the maximum friction coefficient, the concept of XBS is used to signal the entrance of the tyre into a different road surface and to distinguish one type of road from another. The XBS is estimated using elementary diagnostics tools and algebraic methods to filter and estimate derivatives of noisy signals (whose main difficulty is to achieve a good trade-off between filtering and reactivity), and the estimation results are accurate only within certain validity range.

In [41], Hoàng et al. introduced two different models of the wheel acceleration dynamics in which the XBS appears as one of the state variables. The first one is based on the well-known Burckhardt's friction model [12] and it allows to estimate the XBS under the assumption that the road parameters are partially known. To cope with uncertainty on all the road parameters, the second model is based on a re-parametrization of Burckhardt's model that is linear in the (new) unknown parameters. Assumed to be constant, these are regarded as static state variables and the XBS is estimated using an asymptotic state observer for the augmented system. The implementation of this observer, however, still requires knowledge on upper and lower bounds of the road parameters. As a consequence, the observer is not robust to large changes in road conditions, as conservative bounds must be chosen in order to take into account different types of roads.

In the next chapter we present a switched adaptive observer to estimate the XBS using the first model of [41]. In contrast to the latter, our approach does not require any a priori knowledge on the parameters related to the road conditions or their bounds. Instead of changing the friction model, a state-space transformation is used to preserve Burckhardt's standard parametrization and render the system linear in the unknown variables. The proposed observer has an overall better performance than that of [41] and provides a good estimation of the XBS even after large changes in road conditions.

3 EXTENDED-BRAKING-STIFFNESS ESTIMATION

In this chapter we address the problem of XBS estimation during an ABS braking maneuver under the conditions described in Sections 2.3 and 2.4. For convenience, we recall the dynamic model

$$\dot{z}_1 = -\frac{a}{v_x(t)} z_1 z_2 - bu \tag{3.1a}$$

$$\dot{z}_2 = (cz_2 + d)\frac{1}{v_x(t)} z_1, \tag{3.1b}$$

where z_1 is the wheel acceleration offset (and the system's measured output) and z_2 is the XBS.

3.1 OBSERVER DESIGN

The system (3.1) is linear in the unmeasured state z_2; hence, at first sight, one could rely on theory of observer design for such systems —see, e.g. [8, 73], as well as [129, 130, 67]. However, the schemes in these references do not apply directly because c and d are assumed to be unknown; the term cz_2 is nonlinear in two of the unknown variables. To cope with this difficulty, we introduce the linear change of coordinates

$$\begin{aligned} w_1 &= z_1 \\ w_2 &= z_2 + \frac{c}{a} z_1 \end{aligned}$$

that transforms the system (3.1) into

$$\begin{aligned} \dot{w}_1 &= \frac{w_1}{v_x(t)}(cw_1 - aw_2) - bu \\ \dot{w}_2 &= -\frac{bc}{a} u + \frac{w_1}{v_x(t)} d. \end{aligned}$$

In the new coordinates, the previous equations become

$$\dot{w} = A(t, y)w + Bu + \Psi(t, u, y)\theta \tag{3.2a}$$

$$y = Cw, \tag{3.2b}$$

with $w = \begin{bmatrix} w_1 & w_2 \end{bmatrix}^\top$,

$$A(t,y) = \frac{y}{v_x(t)} \begin{bmatrix} 0 & -a \\ 0 & 0 \end{bmatrix} := \frac{y}{v_x(t)} A', \tag{3.3}$$

$$B = \begin{bmatrix} -b \\ 0 \end{bmatrix}, \quad C = \begin{bmatrix} 1 & 0 \end{bmatrix}, \quad \Psi(t,u,y) = \begin{bmatrix} \dfrac{y^2}{v_x(t)} & 0 \\ -\dfrac{b}{a}u & \dfrac{y}{v_x(t)} \end{bmatrix}, \quad \theta = \begin{bmatrix} c \\ d \end{bmatrix},$$

and the measured output $y = w_1$ is the wheel acceleration offset previously defined in (2.2).

Then, inspired by [129], we introduce the adaptive observer

$$\begin{aligned} \dot{\hat{w}} &= A(t,y)\hat{w} + Bu + \Psi(t,u,y)\hat{\theta} \\ &\quad + \left[K(t,y) + \Upsilon\Gamma\Upsilon^\top C^\top\right](y - C\hat{w}) && \text{(3.4a)} \\ \dot{\hat{\theta}} &= \Gamma\Upsilon^\top C^\top (y - C\hat{w}), && \text{(3.4b)} \\ \dot{\Upsilon} &= [A(t,y) - K(t,y)C]\,\Upsilon + \Psi(t,u,y) && \text{(3.4c)} \end{aligned}$$

where $\Gamma = \Gamma^\top > 0$. This observer is also reminiscent of that in [73, Def. 5.3.2] where A is considered to be constant. A benefit of this observer is that the dynamics of the estimation errors $\tilde{w} := \hat{w} - w$ and $\tilde{\theta} := \hat{\theta} - \theta$ corresponds to

$$\begin{aligned} \dot{\tilde{w}} &= [A(t,y) - K(t,y)C]\,\tilde{w} + \Psi(t,u,y)\tilde{\theta} \\ &\quad - \Upsilon\Gamma\Upsilon^\top C^\top C\tilde{w} && \text{(3.5a)} \\ \dot{\tilde{\theta}} &= -\Gamma\Upsilon^\top C^\top C\tilde{w} && \text{(3.5b)} \end{aligned}$$

together with (3.4c). For (3.5), it is shown in [129] that the origin is (uniformly) asymptotically stable[1] if $K(t,y)$ is such that for the system

$$\dot{\tilde{w}} = \left[A(t,y) - K(t,y)C\right]\tilde{w} \tag{3.6}$$

the origin is also (uniformly) asymptotically stable and $\Psi(t,u,y)$ is persistently exciting (PE) along the trajectories, that is to say, if there exist $\mu_1 > 0$ and $T_1 > 0$ such that, for all $t \geq 0$,

$$\int_t^{t+T_1} \Psi(\varsigma, u(\varsigma), y(\varsigma))^\top \Psi(\varsigma, u(\varsigma), y(\varsigma))\, \mathrm{d}\varsigma \geq \mu_1 I \tag{3.7}$$

—cf. [70]. Thus, if $\hat{w} \to w$ and $\hat{\theta} \to \theta$, the estimate of the XBS, which is computed via the inverse change of coordinates

$$\begin{aligned} \hat{z}_1 &= \hat{w}_1 \\ \hat{z}_2 &= \hat{w}_2 - \frac{\hat{c}}{a}\hat{w}_1, \end{aligned}$$

tends to its true values, i.e. $\hat{z} \to z$.

In what follows, we show how to define the observer gain $K(t,y)$ and establish global asymptotic stability of the origin for the system (3.6).

[1] Strictly speaking, in [129] the functions A and K only depend on t; hence exponential stability is established. Such property, however, is out of reach for (3.5).

3.2 ANALYSIS UNDER KNOWN ROAD CONDITIONS

For clarity of exposition, let us assume momentarily that $\hat{\theta} = \theta$ and $\Gamma = 0$. In view of the structure of $A(t, y)$ in (3.3), we set

$$K(t, y) := \frac{y}{v_x(t)} K'(y), \tag{3.8}$$

which is defined on $\mathbb{R}_{\geq 0} \times \mathbb{R}$ since $v_x(t)$ is bounded and separated from zero. We obtain

$$\dot{\tilde{w}} = \frac{y}{v_x(t)} \left[A' - K'(y)C \right] \tilde{w}, \tag{3.9}$$

where K' is yet to be defined. The state variable of this system is $\tilde{w}$. Hence, for the purpose of analysis, we write (3.9) as a linear time-varying system by replacing y with the output trajectories $y(t)$, i.e.

$$\dot{\tilde{w}} = \frac{y(t)}{v_x(t)} \left[A' - K'(y(t))C \right] \tilde{w}. \tag{3.10}$$

Provided that $y(t)$ is defined for all $t \geq 0$, this system is well posed —cf. [54, p. 627], [70].

Let us assume momentarily that $y(t) \neq 0$. Multiplying both sides of (3.10) by $v_x(t)/|y(t)|$ we obtain

$$\frac{v_x(t)}{|y(t)|} \frac{\mathrm{d}\tilde{w}}{\mathrm{d}t} = \operatorname{sgn}(y(t)) \left[A' - K'(y(t))C \right] \tilde{w} \tag{3.11}$$

so it becomes natural to introduce the new time variable $\tau := \nu(t)$, where

$$\nu(t) := \int_0^t \frac{|y(\varsigma)|}{v_x(\varsigma)} \, \mathrm{d}\varsigma. \tag{3.12}$$

Although, at a first glance, it may appear erroneous to define a time variable that depends on the state, this approach is not without precedent in the literature. It is inspired from the concept of orbital equivalence, which was popularized during the sixties and seventies as a tool for analyzing the qualitative properties of differential equations [82, p. 19]. Since then, it has been used to design control laws [99], adaptive filters [44], and observers [32, 95]. It is important to stress that the proposed change of time variable is not needed to implement the observer (3.4), but is only an artifice used in order to analyze the error dynamics. Therefore, whether the time scale depends on a state trajectory that is measurable or not is not a problem, as long as it is well defined (a property that will be guaranteed by Assumption 1 —see Section 3.2.1 for a detailed analysis of this last point). Hence, using

$$\frac{\mathrm{d}\tau}{\mathrm{d}t} = \frac{|y(t)|}{v_x(t)}, \qquad \tau(0) = 0, \tag{3.13}$$

and $t = \nu^{-1}(\tau)$, we may rewrite (3.11) as

$$\frac{\mathrm{d}\tilde{w}}{\mathrm{d}\tau} = \mathcal{A}(\tau)\tilde{w} \tag{3.14}$$

where

$$\mathcal{A}(\tau) = \operatorname{sgn}(y(\nu^{-1}(\tau)))\left[A' - K'(y(\nu^{-1}(\tau))C\right]\tilde{w}.$$

Note that $\operatorname{sgn}(y(\nu^{-1}(\cdot))) =: \sigma(\cdot)$ takes values in $\{-1, 1\}$; hence, it may be regarded as a switching signal. In that light, it is also natural to define the control gain K' as

$$K'(y) = \begin{cases} \begin{bmatrix} k_1^+ \\ k_2^+ \end{bmatrix}, & \text{if } y > 0 \\ \\ \begin{bmatrix} k_1^- \\ k_2^- \end{bmatrix}, & \text{if } y < 0 \end{cases} \tag{3.15}$$

where $k_{1,2}^{\pm}$ are parameters to be defined so that (3.14) become an exponentially-stable *switched* system defined by

$$\frac{\mathrm{d}\tilde{w}}{\mathrm{d}\tau} = A_{\sigma(\tau)}\tilde{w}, \tag{3.16}$$

where

$$A_{\sigma(\tau)} = \begin{cases} A_+ = \begin{bmatrix} -k_1^+ & -a \\ -k_2^+ & 0 \end{bmatrix}, & \text{if } y(\tau) > 0 \\ \\ A_- = \begin{bmatrix} k_1^- & a \\ k_2^- & 0 \end{bmatrix}, & \text{if } y(\tau) < 0. \end{cases}$$

Stability of switched systems is a well-studied subject [68]; sufficient conditions for this system to be exponentially stable are that $\sigma(\tau)$ admits a dwell time and that the dynamics of the system for each value of σ is exponentially stable. Nevertheless, for standard theory on switched systems to apply to the system (3.16), several technical aspects must be taken into account. So far, we have implicitly assumed that the output trajectory $y(t) \neq 0$; this is needed for (3.11) to be well defined. Furthermore, we implicitly assumed that the time-scale defined in (3.12) is well-posed.

Indeed, for this transformation to be well defined, the time τ must never evolve backwards relative to the actual time t, it must not go to infinity in finite time t, and it must not have a finite limit. The first condition holds because $t \mapsto \nu$ is non-decreasing —see (3.13) and (2.3). The second condition is guaranteed by the fact that y is bounded and the vehicle's velocity satisfies (2.3) —see (3.12). To guarantee the third condition we rely on typical wheel acceleration profiles that correspond to the operation of commercial ABS —cf. Fig. 2.2; see also [94, pp. 82-89] and [74, § 30.1.3].

Assumption 1. *During an ABS braking maneuver the wheel acceleration offset y satisfies the following:*

(i) y is persistently exciting (PE), i.e. there exist $\mu_0 > 0$ and $T_0 > 0$ such that

$$\int_t^{t+T_0} y(\varsigma)^2 \, \mathrm{d}\varsigma \geq \mu_0, \qquad \forall\, t \geq 0; \tag{3.17}$$

(ii) y crosses zero only at isolated points, i.e. for all $t_k \geq 0$ such that $y(t_k) = 0$,

$$\frac{\mathrm{d}y}{\mathrm{d}t}(t_k) \neq 0 \tag{3.18}$$

and, moreover, any two such points are separated by an interval of length no smaller than $T_D > 0$, i.e. for all $t_k, t_l \geq 0$, such that $y(t_k) = 0$ and $y(t_l) = 0$ with $t_k \neq t_l$,

$$\left|t_k - t_l\right| \geq T_D. \tag{3.19}$$

The hypothesis that y is PE guarantees that $\tau(t)$ does not tend to a constant as $t \to \infty$. Thus, the time-scale transformation (3.12) is well posed. Finally, the conditions (3.18) and (3.19) guarantee that the switching signal $\rho(t) := \operatorname{sgn}(y(t))$ has a minimal dwell-time T_D. This, and the continuity of ν in (3.12), implies that $\sigma(\tau)$ also has a minimal dwell-time τ_D (see Section 3.2.2 for details).

We are now ready to present our first statement, for the case in which the parameters are known.

Proposition 1. *Consider the system* (3.6) *with $K(t, y)$ given by* (3.8), (3.15), *and*

$$k_1^+ > 0, \quad k_2^+ < 0, \quad k_1^- = -k_1^+ < 0, \quad k_2^- = k_2^+ < 0. \tag{3.20}$$

If v_x satisfies (2.3) *and Assumption 1 holds, for the system* (3.6), *the origin $\{\tilde{w} = 0\}$ is globally asymptotically stable.*

Proof. The proof is inspired by Hoàng et al. [41, 42]. The characteristic polynomials of A_+ and A_- are

$$\varrho^2 + k_1^+ \varrho - a k_2^+ \qquad \text{and} \qquad \varrho^2 - k_1^- \varrho - a k_2^-,$$

respectively. For a polynomial of order 2 to have roots with negative real part, it is necessary and sufficient that all its coefficients be positive. Thus, the conditions

$$k_1^+ > 0, \quad k_2^+ < 0, \quad k_1^- < 0, \quad k_2^- < 0$$

ensure that the matrices A_+ and A_- are Hurwitz and a direct computation shows that the pairs (A_+, C) and (A_-, C) are observable. It follows that there exist two symmetric positive-definite matrices P_+ and P_- such that

$$A_+^\top P_+ + P_+ A_+ = -C^\top C \qquad \text{and} \qquad A_-^\top P_- + P_- A_- = -C^\top C$$

hold [116, Prop. 5.4]. Furthermore, a direct computation shows that, by imposing

$$k_1^- = -k_1^+, \quad k_2^- = k_2^+,$$

the solutions of the previous Lyapunov equations satisfy $P_+ = P_- =: P$. Thus, P defines a nonstrict (because $C^\top C$ is positive semidefinite) common Lyapunov function for the switched system (3.16). Under these conditions, and since the switching signal $\sigma(\tau)$ has a minimal dwell time τ_D, it follows from [37, Th. 4] that the origin for the system (3.16) is globally exponentially stable, uniformly with respect to the switching signal. Consequently, in the original time-scale, the origin for the system (3.6) is globally asymptotically stable. □

3.2.1 TIME-SCALE TRANSFORMATION

In this section we prove that the time-scale transformation (3.12) is well defined. To that end, (3.13) is regarded as the result of two successive transformations. That is, a first transformation from the original time variable t to an intermediate (or auxiliary) time variable s, and a second transformation from s to the time variable τ, in which the analysis of the switched system (3.16) is carried out.

The first time-scale transformation is defined as

$$\frac{\mathrm{d}s}{\mathrm{d}t} = \frac{1}{v_x(t)}, \qquad s(0) = 0, \tag{3.21}$$

where s is the intermediate time variable. This transformation is well defined because v_x is positive, bounded, and separated from zero. That is, the time s never evolves backwards with respect to the actual time t and

$$s \to \infty \Leftrightarrow t \to \infty.$$

Now, let us define the second time-scale transformation

$$\frac{\mathrm{d}\tau}{\mathrm{d}s} = \big|y(t(s))\big|, \qquad \tau(0) = 0. \tag{3.22}$$

Remark 1. *In* (3.22) *we write* $y(t(s))$*, and not* $y(s(t))$*, because the analysis that follows is performed in the* s *time-scale, i.e. regarding* s *as the independent time variable.*

Integrating (3.22) yields

$$\tau(s) = \int_0^s \big|y(t(\varsigma))\big| \,\mathrm{d}\varsigma. \tag{3.23}$$

Because y is bounded, there exists $y_{\max} > 0$ such that $\big|y(t(s))\big| \leq y_{\max}$ for all $s \geq 0$. This implies

$$\int_0^s \big|y(t(\varsigma))\big| \,\mathrm{d}\varsigma \leq y_{\max} s. \tag{3.24}$$

From (3.24) and (3.23), we have $\tau(s) \leq y_{\max} s$. Hence, τ does not go to infinity in finite s.

To prove that $\tau(s) \to \infty$ as $s \to \infty$, we invoke the substitution theorem for integrals [5, §. 5.7]:

$$\int_\alpha^\beta f\big(g(x)\big) g'(x) \,\mathrm{d}x = \int_{g(\alpha)}^{g(\beta)} f(x) \,\mathrm{d}x \tag{3.25}$$

and we define $g(\alpha) =: \check{a}$ and $g(\beta) =: \check{b}$. Note that if g^{-1} exists, then $\alpha = g^{-1}(\check{a})$, $\beta = g^{-1}(\check{b})$ and (3.25) becomes

$$\int_{g^{-1}(\check{a})}^{g^{-1}(\check{b})} f\big(g(x)\big)g'(x)\,\mathrm{d}x = \int_{\check{a}}^{\check{b}} f(x)\,\mathrm{d}x. \tag{3.26}$$

Because the transformation (3.21) is well defined, we apply this statement with

$$t = g(s), \qquad s = g^{-1}(t),$$

and we use (3.26) to relate the PE condition (3.17) in the t and s time-scales. That is, taking $\check{a} = t$, $\check{b} = t + T_0$ and $f(t) = y(t)^2$, from (3.17) and (3.26) we obtain

$$\int_t^{t+T_0} y(\varsigma)^2\,\mathrm{d}\varsigma = \int_{s(t)}^{s(t+T_0)} y(t(\varsigma))^2 v_x(t(\varsigma))\,\mathrm{d}\varsigma \geq \mu_0 \tag{3.27}$$

for all $s(t) \geq 0$. Now, because s is a strictly increasing function of t and satisfies (3.21) and (2.3), it follows that

$$\frac{T_0}{v_{x\max}} \leq s(t + T_0) - s(t) \leq \frac{T_0}{v_{x\min}}. \tag{3.28}$$

Also, recall that if a signal is PE over an interval of length T_0, then it is PE for any interval of length $T_0' \geq T_0$ [81, § 6.3]. Let $T_0' := T_0/v_{x\min}$. It follows, from (3.27) and (3.28), that

$$\int_{s(t)}^{s(t)+T_0'} y(t(\varsigma))^2 v_x(t(\varsigma))\,\mathrm{d}\varsigma \geq \mu_0, \tag{3.29}$$

and, from (2.3) and (3.29), that

$$\int_{s(t)}^{s(t)+T_0'} y(t(\varsigma))^2\,\mathrm{d}\varsigma \geq \frac{\mu_0}{v_{x\max}}. \tag{3.30}$$

Moreover, because y is bounded, we have

$$\left|\frac{y(t(s))}{y_{\max}}\right| \leq 1$$

for all $s \geq 0$. Thus,

$$\left|\frac{y(t(s))}{y_{\max}}\right| \geq \left(\frac{y(t(s))}{y_{\max}}\right)^2. \tag{3.31}$$

Multiplying both sides of (3.31) by $y_{\max}^2$ and integrating from $s(t)$ to $s(t) + T_0'$ it follows, from (3.30), that

$$\int_{s(t)}^{s(t)+T_0'} \big|y(t(\varsigma))\big|\,\mathrm{d}\varsigma \geq \frac{\mu_0}{v_{x\max}y_{\max}}. \tag{3.32}$$

Evaluating the limit of $\tau(s)$, given by (3.23), as $s \to \infty$ is tantamount to evaluating that of $\int_0^{nT_0'} \left|y(t(\varsigma))\right| \mathrm{d}\varsigma$ as $n \to \infty$. Thus, defining $\mu_0' := \mu_0 / v_{x\max} y_{\max}$, from (3.32) we have

$$\int_0^{nT_0'} \left|y(t(\varsigma))\right| \mathrm{d}\varsigma \geq n\mu_0',$$

which in turn implies that

$$\lim_{s\to\infty} \tau(s) = \lim_{n\to\infty} \int_0^{nT_0'} \left|y(t(\varsigma))\right| \mathrm{d}\varsigma = \infty.$$

We conclude that the transformation (3.22) is well defined, and so is (3.13), which is equivalent to applying (3.21) followed by (3.22). Moreover, the condition (3.18) ensures that the function h, such that $\tau = h(s)$, is globally invertible, i.e. $s = h^{-1}(\tau)$. Thus, we can define $\tau = h \circ g^{-1}(t) =: \nu(t)$ and $t = g \circ h^{-1}(\tau) = \nu^{-1}(\tau)$, where ν and ν^{-1} are also continuous functions.

3.2.2 DWELL-TIME

In this section we prove that the existence of a dwell-time for the switching signal $\rho(t)$ in the original time-scale, implies the existence of a dwell-time for $\sigma(\tau)$ in the τ time-scale.

By definition, continuity of ν^{-1} implies that for any sequence $\{\tau_n\}_{n\in\mathbb{N}}$ that converges to a point m, the corresponding sequence $\{\nu^{-1}(\tau_n)\}_{n\in\mathbb{N}}$ converges to $\nu^{-1}(m)$. We will proceed by contradiction. Assume that the switching signal $\rho(t)$ admits a dwell-time, but $\sigma(\tau)$ does not. Take $\{\tau_n\}$ as the sequence of time instants in the τ time-scale in which a switch in $\sigma(\tau)$ occurs. Because $\sigma(\tau)$ does not admit a dwell time, the sequence $\{\tau_n\}$ converges to some point m. Then, by continuity of ν^{-1}, the sequence $\{t_n\} = \{\nu^{-1}(\tau_n)\}$ of time instants in the original time-scale in which a switch in $\rho(t)$ takes place, converges to $\nu^{-1}(m)$. This implies that $\rho(t)$ does not admit a dwell-time. The contradiction is therefore established, thus proving that the existence of a dwell-time for $\rho(t)$ implies the existence of a dwell-time for $\sigma(\tau)$.

3.3 ANALYSIS UNDER UNKNOWN ROAD CONDITIONS

Proposition 2. *Consider the system* (3.2) *and the observer given by* (3.4), (3.8), (3.15), *and* (3.20). *Assume that v_x satisfies* (2.3), *Assumption 1 holds, and $t \mapsto \Psi(t, u(t), y(t))$ is PE. Then, the origin $(\tilde{w}, \tilde{\theta}) = (0, 0)$ of* (3.5) *is globally asymptotically stable.*

Proof. The proof is inspired by Zhang [129]. Define the linear combination of the estimation errors

$$\eta := \tilde{w} - \mathrm{Y}\tilde{\theta}.$$

Differentiating η, using (3.5a), (3.5b) and (3.4c), we get

$$\dot{\eta} = \big[A(t,y) - K(t,y)C\big]\eta \tag{3.33}$$

and, from (3.5b) and the definition of η, we have

$$\dot{\tilde{\theta}} = -\Gamma \mathrm{Y}^\top C^\top C\big[\mathrm{Y}\tilde{\theta} + \eta\big]. \tag{3.34}$$

Note that the system formed by (3.33) and (3.34) has a cascade structure. This is relevant because, for cascaded systems, sufficient conditions for the origin to be globally asymptotically stable (GAS) are well established —see, e.g. [71] and references therein. It is enough that the origin for (3.33) be GAS, that the origin for (3.34) with $\eta = 0$ be GAS, and that the solutions of (3.34)–(3.33) be uniformly globally bounded [86].

Now, note that the dynamics of η given by (3.33) has exactly the same form as that of the system (3.6). Thus, it follows from Proposition 1 that the origin of (3.33) is GAS. Moreover, take $\eta = 0$ in (3.34) and consider the unforced system

$$\dot{\tilde{\theta}} = -\Gamma \mathrm{Y}^\top C^\top C\mathrm{Y}\tilde{\theta}. \tag{3.35}$$

As $\Psi(\cdot, u(\cdot), y(\cdot))$ is bounded and PE, $\mathrm{Y}(\cdot, u(\cdot), y(\cdot))$ defined by (3.4c) is also bounded and PE [87]. Hence, the origin of (3.35) is globally exponentially stable and (3.34) is input-to-state stable with respect to the input η. Furthermore, the interconnection term $-\Gamma \mathrm{Y}^\top C^\top C$ is bounded. Therefore, it follows by a cascade argument that the origin $(\tilde{\theta}, \eta) = (0, 0)$ of the system (3.34)–(3.33) is GAS. Finally, to see that the same property holds for the origin $(\tilde{w}, \tilde{\theta}) = (0, 0)$ of (3.5), we observe that $\tilde{w} = \eta + \mathrm{Y}\tilde{\theta}$. □

3.4 SIMULATION RESULTS: SINGLE-WHEEL SYSTEM

The performance of the proposed switched adaptive observer has been tested via numerical simulations considering the (nonsimplified) quarter-car model described in Section 2.1. A braking scenario of a vehicle traveling with an initial speed of 25 m/s and a constant deceleration of 1.96 m/s^2 is illustrated in Figs. 3.1 to 3.9. Changes in road conditions occur at times $t = 3$ and $t = 6$: during the first part of the simulation the wheel runs on dry asphalt, then on wet asphalt, and finally on dry concrete. For the purpose of generating meaningful signals, the system is driven via a five-phase hybrid ABS control algorithm (see [89, 31] for a full description) that modulates the brake pressure based on measurements of the wheel acceleration offset. Persistency of excitation of $\Psi(\cdot, u(\cdot), y(\cdot))$ under such scenario is verified in Fig. 3.1, which shows the eigenvalues of the left-hand side of (3.7) for $T_1 = 1$ —recall that (3.7) holds if and only if

$$\varrho_{\min}\left\{\int_t^{t+T_1} \Psi(\varsigma, u(\varsigma), y(\varsigma))^\top \Psi(\varsigma, u(\varsigma), y(\varsigma))\,\mathrm{d}\varsigma\right\} \geq \mu_1 > 0$$

for all t, where $\varrho_{\min}\{\cdot\}$ denotes the minimal eigenvalue of the argument. The observer was tested under ideal conditions, i.e. without measurement noise or other external disturbances, as well as under a more realistic scenario considering a velocity-dependent perturbation in the system's measured output

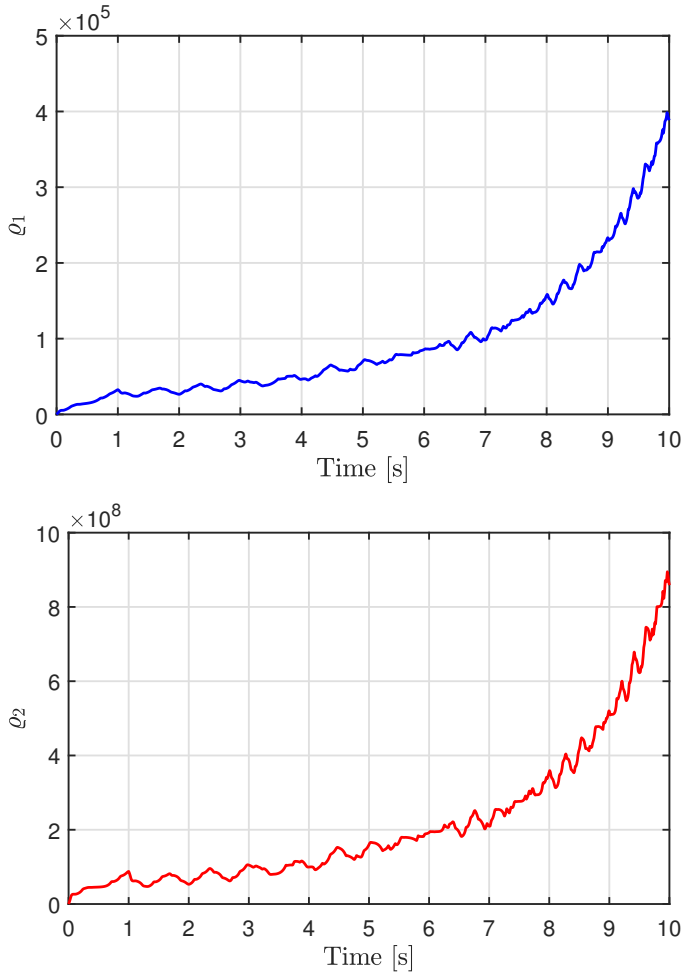

Figure 3.1: Eigenvalues of $\int_t^{t+T_1} \Psi(\varsigma, u(\varsigma), y(\varsigma))^\top \Psi(\varsigma, u(\varsigma), y(\varsigma))\, \mathrm{d}\varsigma$.

(Fig. 3.6). That is, the measurement of the wheel acceleration offset is perturbed by periodic (in one mechanical revolution) oscillations caused by imperfections in the wheel-speed sensors used in automotive applications (see Section 5.3).

The estimation results obtained under the ideal scenario are illustrated in Figs. 3.3 to 3.5. A quick convergence to zero of both the state and parameter estimation errors $\tilde{w}$, $\tilde{\theta}$ can be observed (Fig. 3.3), even after the abrupt transitions between different types of roads. Consequently, the estimated XBS also converges to its true value. In Figs. 3.4 and 3.5, we show a comparison between the XBS estimated via the adaptive observer presented in this paper and the one estimated via the augmented-state observer proposed in [41]. The adaptive observer exhibits better robustness properties to changes in road conditions than the augmented-state observer, and a better performance both during transient and steady-state conditions.

Figs. 3.7 to 3.9 illustrate the results obtained under the perturbed scenario. As it could be expected, the estimation errors $\tilde{w}, \tilde{\theta}$ are perturbed due to the error in the system's measured output, but they approach zero as the perturbation vanishes (because the perturbation is velocity-dependent, its amplitude

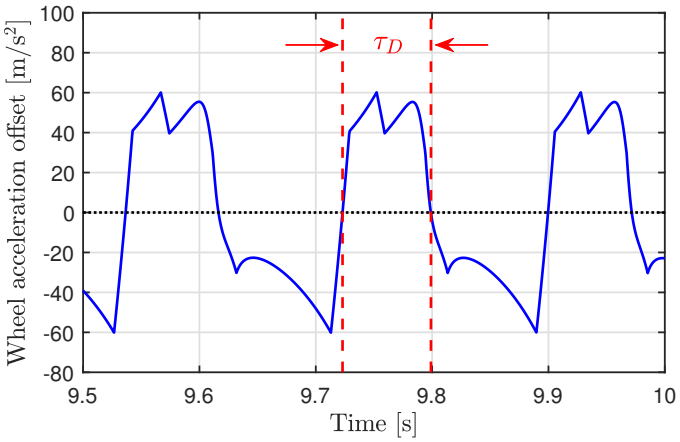

Figure 3.2: Wheel acceleration offset: illustration of the dwell-time condition.

decreases as the vehicle velocity is reduced). Therefore, with the adaptive observer the estimated XBS closely approaches its true value. Such is not the case for the augmented-state observer, which displays greater sensitivity to the error in the system's measured output, and whose estimation error does not converge to zero even as the perturbation vanishes. The results thus validate the effectiveness of the proposed approach.

3.5 Experimental results: single-wheel system

The performance of the proposed observer has been tested on experimental data acquired from the tyre-in-the-loop test rig of the Delft University of Technology during the evaluation of ABS strategies [31]. The test rig (Fig. 3.10) consists of a tyre rolling on top of a 2.5 m diameter steel drum (see [85, Fig. 12.7]). The tyre is mounted on a rim attached to a rotating axle that is, in turn, supported by a fixed frame through mechanical bearings. To emulate the displacement of the vehicle with respect to the road, the drum rotates about its axis driven by an electric motor. The braking of the wheel is performed via a hydraulic disk brake mounted on one side of the axle. The forces acting on the tyre are measured via piezoelectric force transducers, while the wheel and the drum speeds are measured by encoders.

Fig. 3.11 shows the wheel slip of an experiment [31] conducted at a drum speed of approximately 65 km/h. The five-phase hybrid ABS control algorithm of [89] is active between $t = 3.85$ s and $t = 7.27$ s; thus the switched adaptive observer is tested during that interval. To validate the estimation results, the data of Fig. 3.12 was fitted to the friction model (2.5) in order to identify the coefficients c_i. This allows to compute the XBS offline by evaluating the derivative of the fitted curve over the wheel slip. Then, the states and parameters of the system (3.2) can be computed offline from the wheel-acceleration-offset measurements and the parameters of the fitted friction curve.

The estimation results are illustrated in Fig. 3.13. The estimates of the states w_1 and w_2 converge to their real values within 0.5 s, even though the estimates

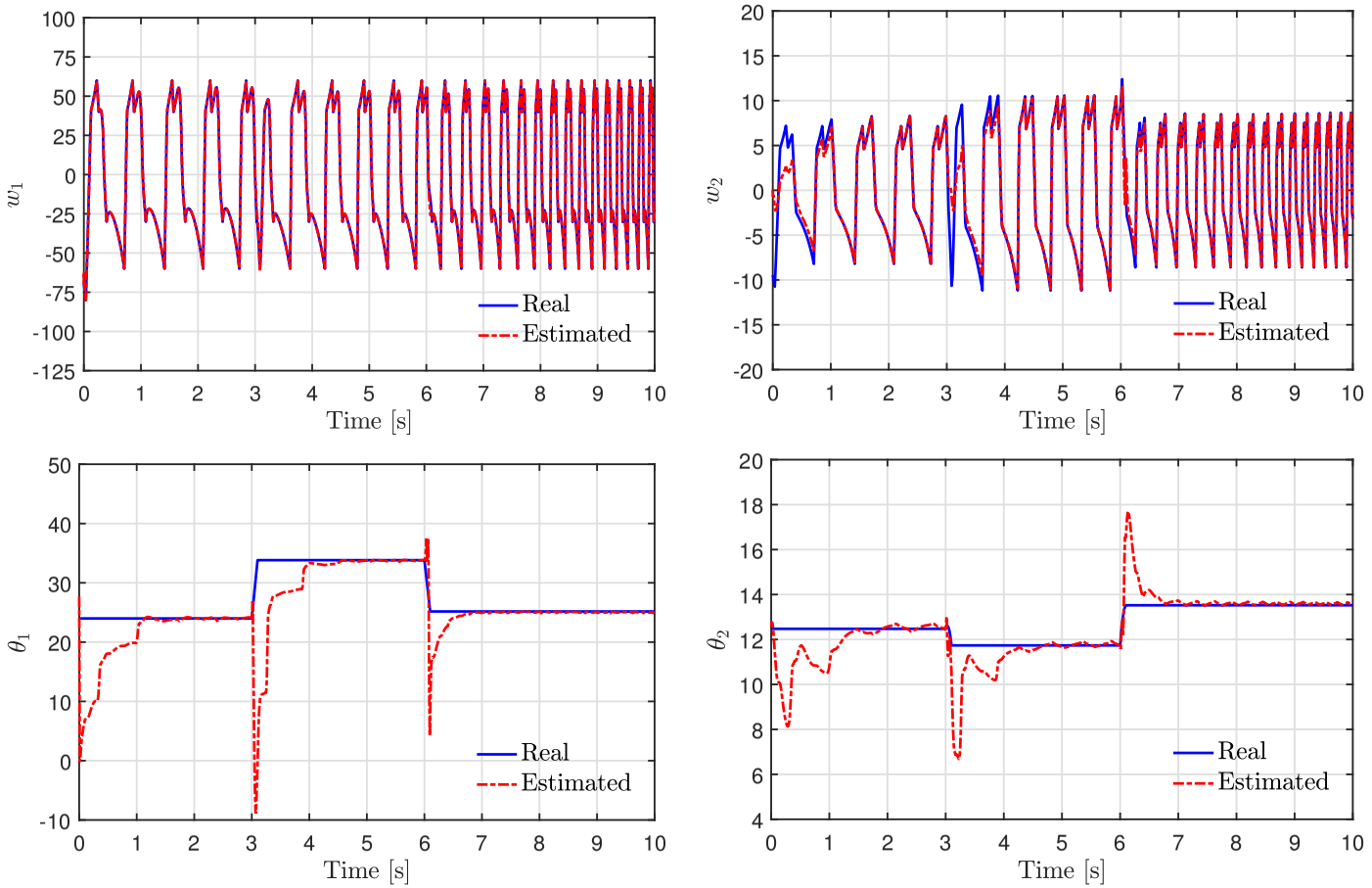

Figure 3.3: Ideal scenario: real vs estimated states and parameters.

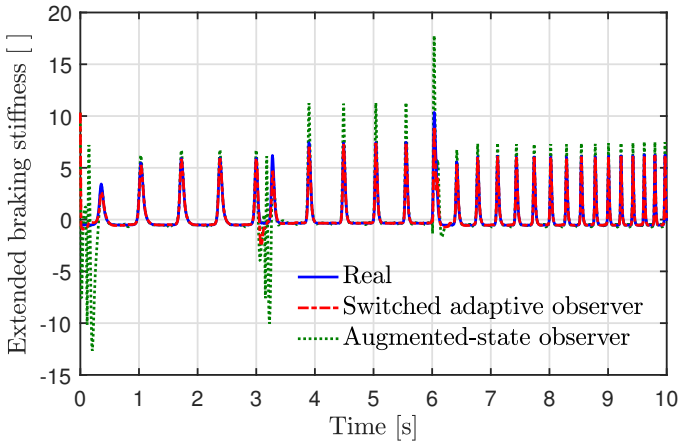

Figure 3.4: Ideal scenario: real vs estimated XBS.

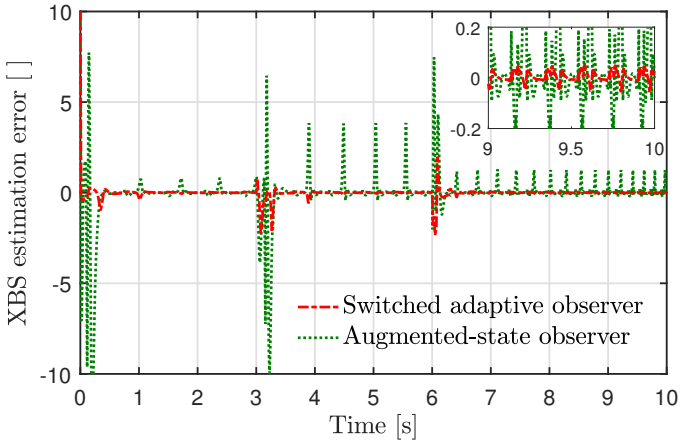

Figure 3.5: Ideal scenario: XBS estimation error.

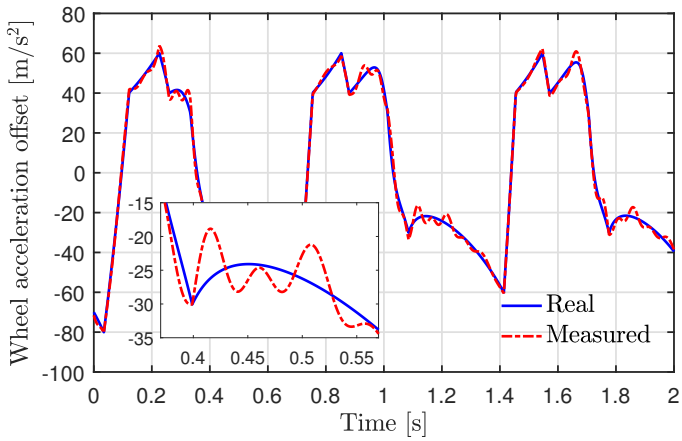

Figure 3.6: Wheel acceleration offset: real signal vs perturbed measurement.

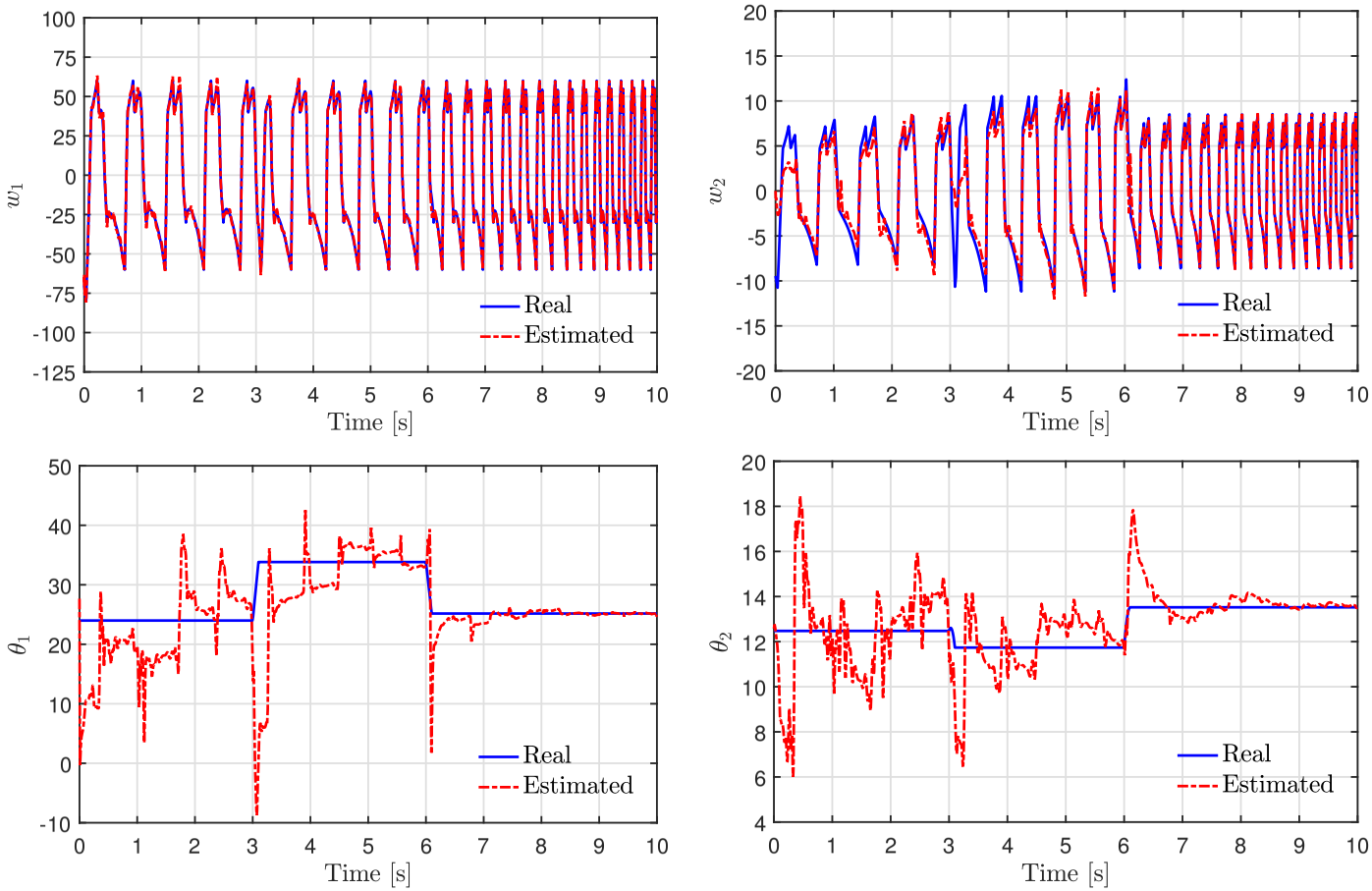

Figure 3.7: Perturbed scenario: real vs estimated states and parameters.

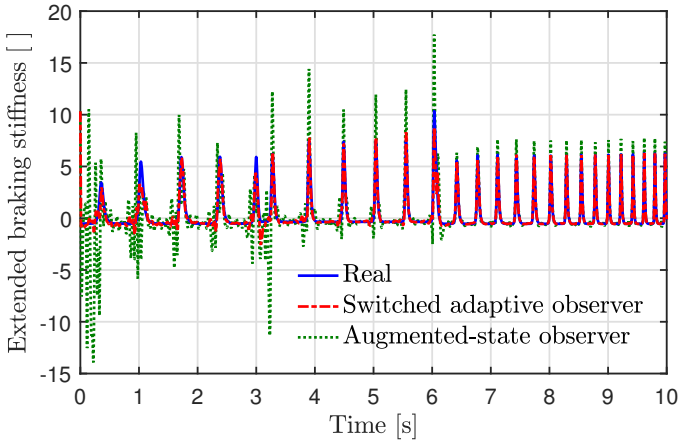

Figure 3.8: Perturbed scenario: real vs estimated XBS.

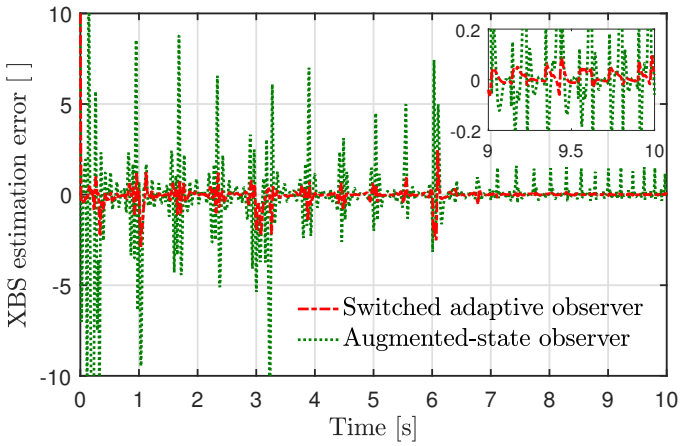

Figure 3.9: Perturbed scenario: XBS estimation error.

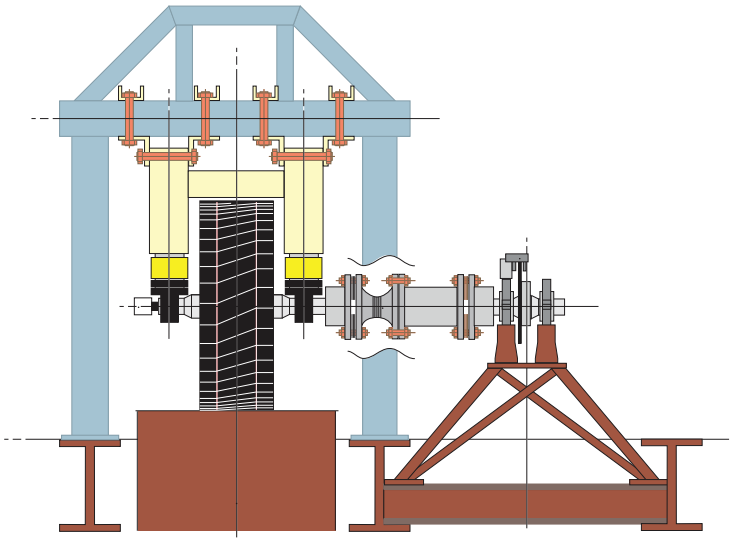

Figure 3.10: Front-view illustration of the tyre-in-the-loop test rig. Source of illustration: [31].

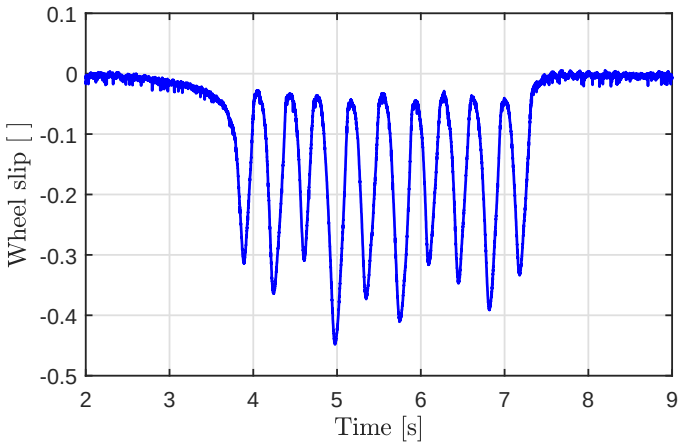

Figure 3.11: Wheel slip measured during an experiment at 65 km/h. A five-phase hybrid ABS algorithm is active between $t = 3.85$ s and $t = 7.27$ s.

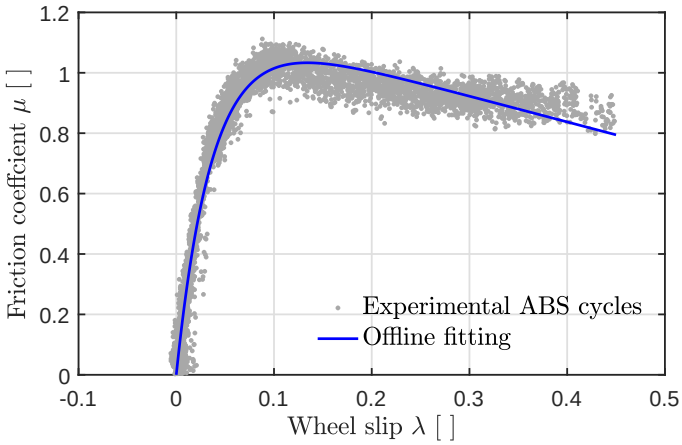

Figure 3.12: Measurement and offline fitting of the friction characteristics of the tyre-in-the-loop test rig. The parameters associated to the tyre mounted on the rim are $J = 1.2$ kg·m^2, $R = 0.3$ m, $F_z = 2850$ N·m, and $\gamma_b = 17.5$ N·m/bar. The fitted values of Burckhardt's friction model are $c_1 = 1.1794$, $c_2 = 27$, and $c_3 = 0.8552$. For the half of the curve with negative λ, the parameters c_1 and c_2 are also negative.

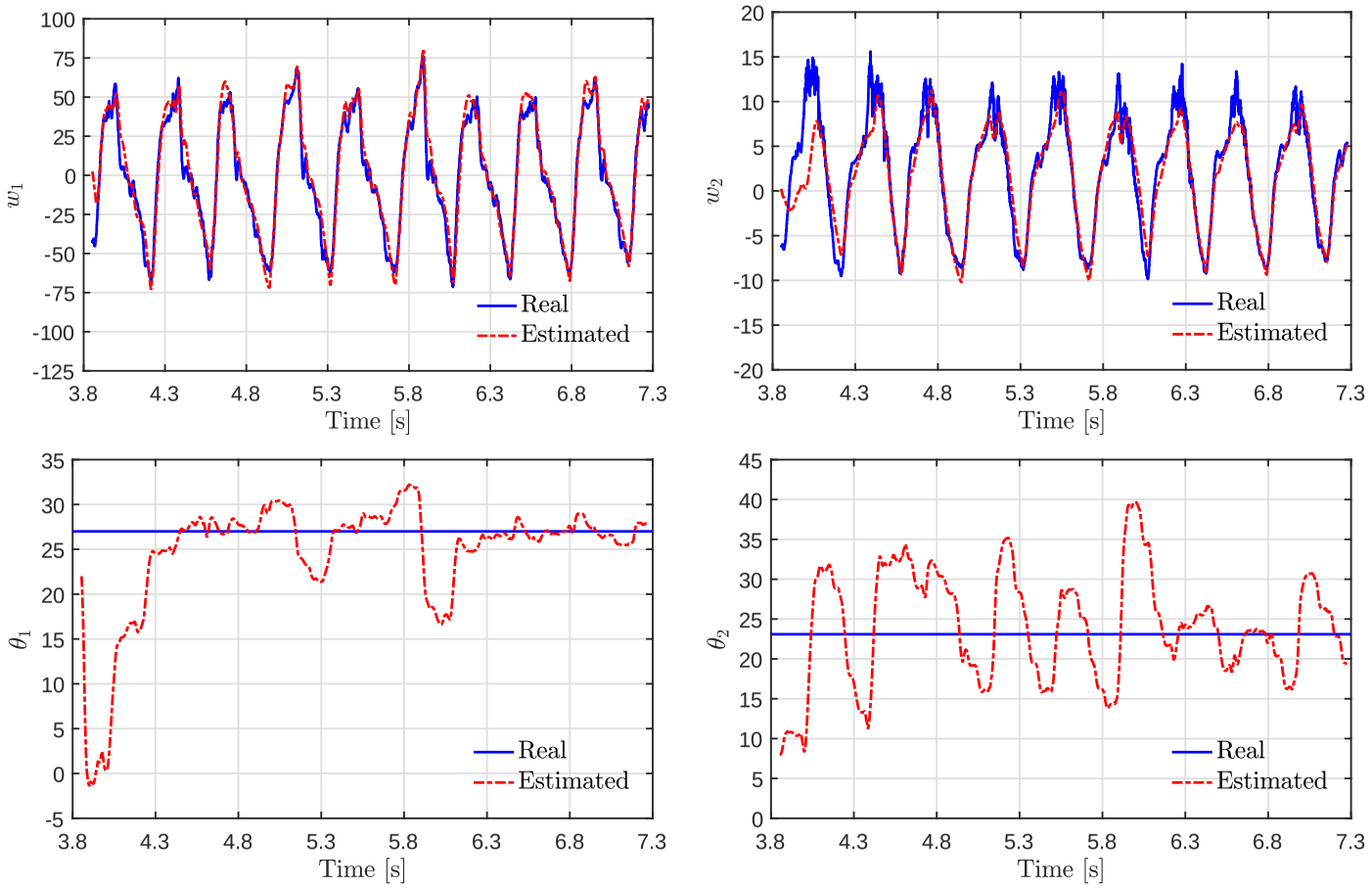

Figure 3.13: Real vs estimated states and parameters of the system (3.2).

of the parameters θ_1 and θ_2 do not converge to a constant value. It should be noted, however, that the estimated parameters do approach their real values and remain close to them during the rest of the experiment. As a result, a good estimation of the XBS is obtained, as illustrated in Fig. 3.14. The results obtained via the augmented-state observer proposed in [41] are shown as well. The switched adaptive observer clearly exhibits an overall better performance.

3.6 Simulation results: two-axle vehicle model

In this section we present some simulation results using a two-axle vehicle model [30]. The objective is to test the performance of the observer under changes in the road conditions (a perturbation that cannot be implemented in the test rig) and in the presence of vehicle dynamics that were not considered during the design stage. These include the suspension dynamics, as well as load transfer phenomenon and tyre relaxation length. Moreover, because the vehicle speed is not directly measured in commercial vehicles due to the lack of cost-effective and reliable sensors [96], the simulations consider that the vehicle speed is estimated from the measurements of the angular velocities of the wheels and the longitudinal acceleration of the vehicle.

Figs. 3.15, 3.16, and 3.17 illustrate a hard-braking scenario of a vehicle traveling at an initial speed of 180 km/h. The vehicle starts braking at $t = 0.25$ s. The braking on each wheel is individually controlled by a six-phase ABS control algorithm that is activated at $t = 0.75$ s in the front axle, and at $t = 0.50$ s in the rear axle. Changes in the road conditions occur at times 2.5 s and 5 s: during the first part of the simulation the vehicle runs on dry asphalt, then on snow, and then on wet asphalt. The vehicle speed at the end of the simulation is 15 km/h.

As with the experimental tests, the XBS estimation is performed during the interval in which the ABS is active. To evaluate the observer under realistic conditions, the vehicle speed is not considered to be directly measured. Instead, it is estimated using the Kalman-filter approach of [19], which takes as inputs the measurements of the linear velocity of the front wheel (computed as $R\omega$) and the longitudinal acceleration $a_x(t)$. The latter is affected by an additive dynamic bias with a turn-on component of 0.5 m/s^2, which is common in modern accelerometers [97]. The estimate of $v_x(t)$ used in the implementation of the observer is shown in Fig. 3.15. Because of the harsh braking conditions, the estimate displays an average error of 18% relative to its true value.

Moreover, in order to take into account the load transfer phenomenon in the implementation of (3.4), the parameter a that depends on the vertical load on each wheel is computed online using the measurements of the vehicle longitudinal acceleration. That is, the vertical loads F_{z_f} and F_{z_r} in the front and rear

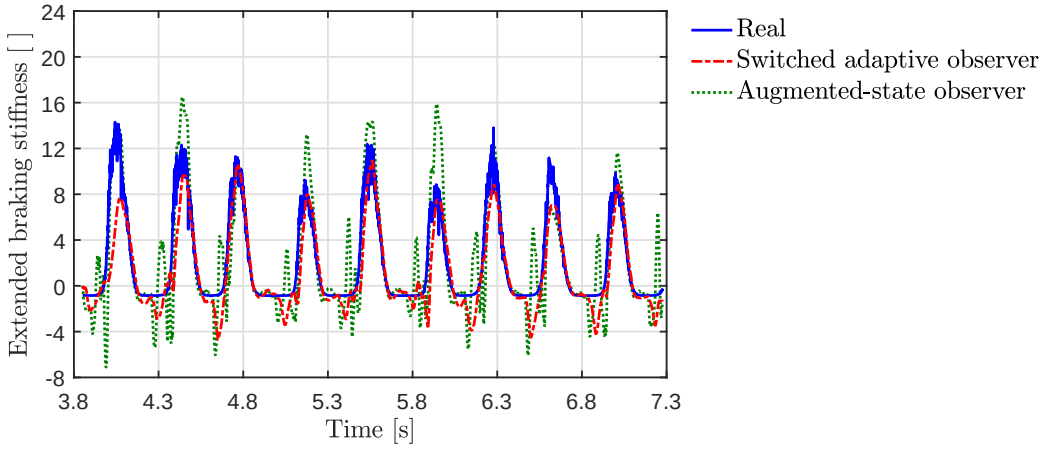

(a)

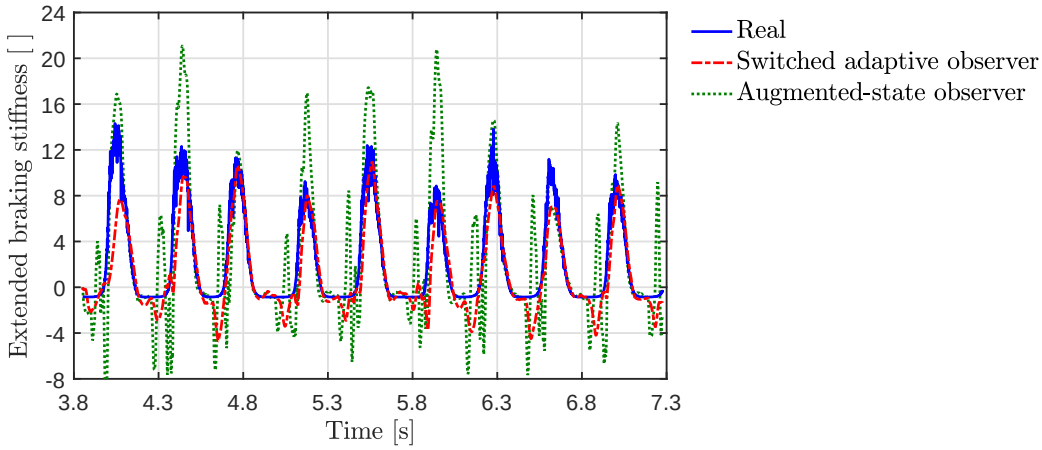

(b)

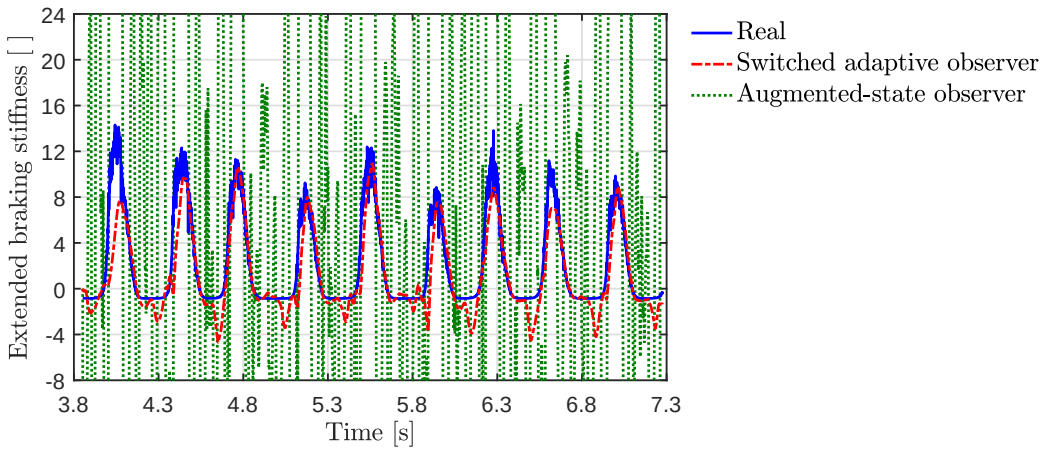

(c)

Figure 3.14: Real vs estimated XBS. The switched adaptive observer exhibits an overall better performance than the augmented-state observer of [41], especially when the latter is designed using conservative bounds on the road parameters. The augmented-state observer is implemented considering the parameters of: (a) the tyre-in-the-loop test rig, (b) dry and wet asphalt, and (c) all road conditions, from dry asphalt to ice.

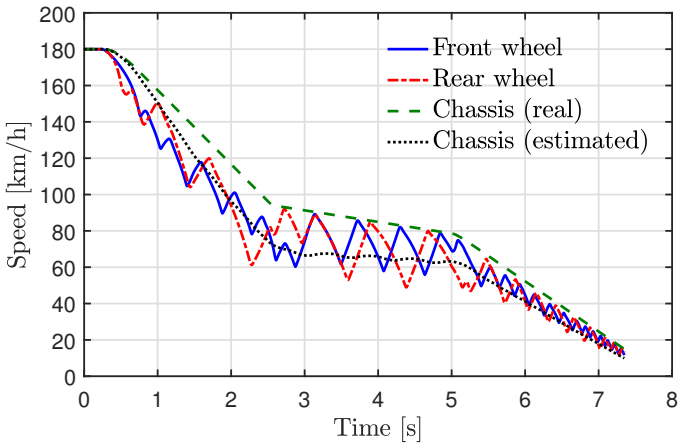

Figure 3.15: Longitudinal speed of the vehicle and linear speed of the tyres at the wheel-ground contact point during an ABS braking scenario.

wheels are computed as [101, § 2.4]

$$F_{z_f} = W_f - \Delta_{F_z} a_x(t), \tag{3.36a}$$
$$F_{z_r} = W_r + \Delta_{F_z} a_x(t), \tag{3.36b}$$

where W_f and W_r are the static vertical loads at the front and rear wheels, and Δ_{F_z} is the coefficient of load transfer due to the vehicle acceleration. These three parameters are constant and depend on (known) geometrical and mechanical characteristics of the vehicle. Thus, the above expressions can be computed with the measurements of $a_x(t)$. Fig. 3.17 shows the vertical load on each wheel during the considered braking scenario. The dotted lines correspond to the values of F_{z_f} and F_{z_r} computed using (3.36). Even though the measurements of $a_x(t)$ are subject to the accelerometer's bias, the computed values follow closely the real values of the vertical load in each wheel, thus they provide a reasonable approximation for the parameter a to be used in the observer.

The observer's robustness to the uncertainties described above is illustrated in Fig. 3.18. The graphic shows a comparison between the XBS estimated using the true signals $v_x(t)$ and $a_x(t)$ and that estimated using the vehicle's estimated speed (Fig. 3.15) and measured acceleration subject to sensor bias. Note in the latter case that even though the vehicle speed is underestimated by 18%, the observer still provides a reasonable approximation of the XBS. Notably, the zero-crossing of the estimate coincides with that of the real XBS. This is important because it means that the observer properly detects when the system transitions from one region of the tyre to the other.

The observer's overall performance, i.e. considering all the aforementioned uncertainties and perturbations, is illustrated in Fig. 3.19. During the initial transient, the estimate of the front tyre exhibits a better performance than that of the rear tyre. Because the abrupt changes in the road conditions (and thus in the parameters c and d of the model (3.2)) cause a sudden growth of the error $y - C\hat{w}$ between the measured and the expected output in (3.4), the estimates

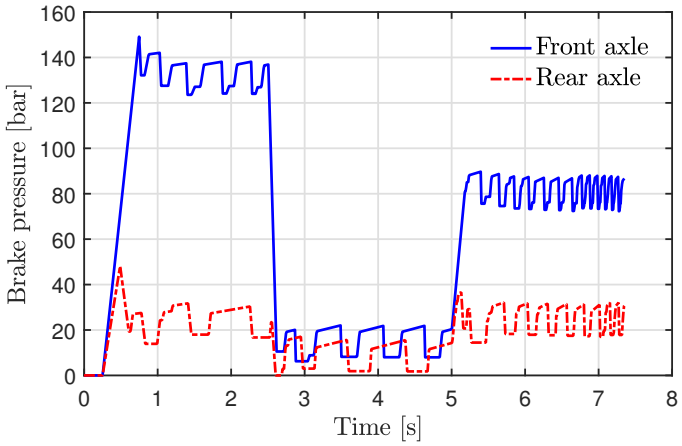

Figure 3.16: Brake pressure in the front and rear wheels during an ABS braking scenario. The pressure is drastically reduced between $t = 2.5$ s and $t = 5$ s when the vehicle runs on a low-friction surface (snow).

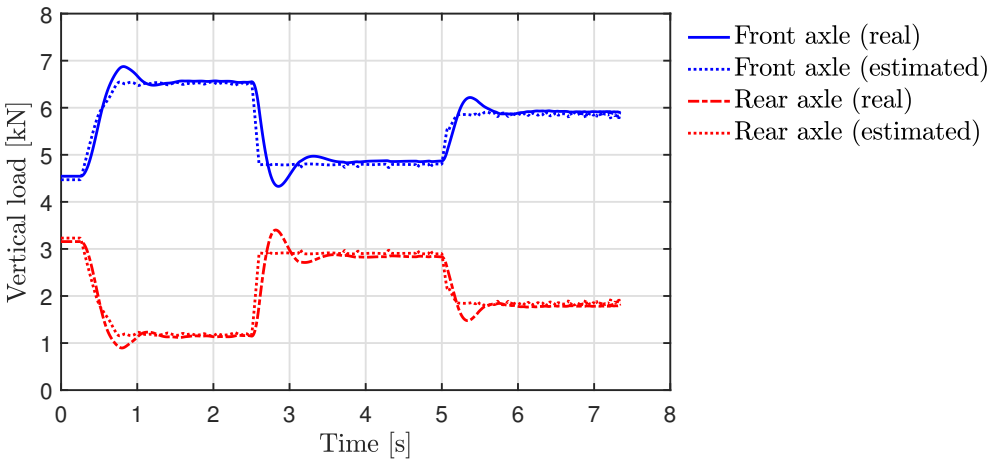

Figure 3.17: Vertical load in the front and rear axles during an ABS braking scenario. The dotted lines correspond to the values of F_{z_f} and F_{z_r} computed using (3.36) that are used in the implementation of the observer.

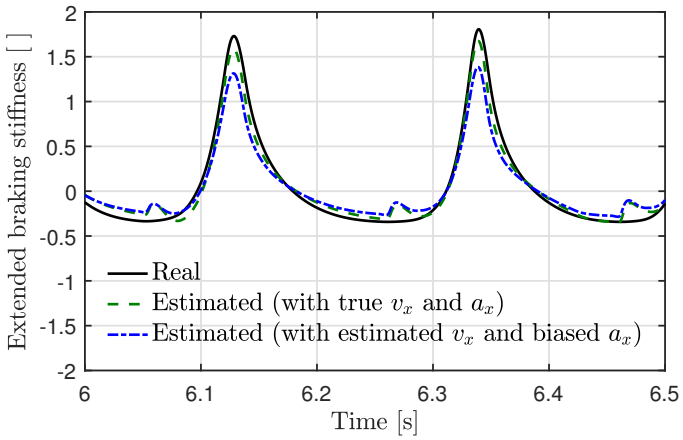

(a) Front axle

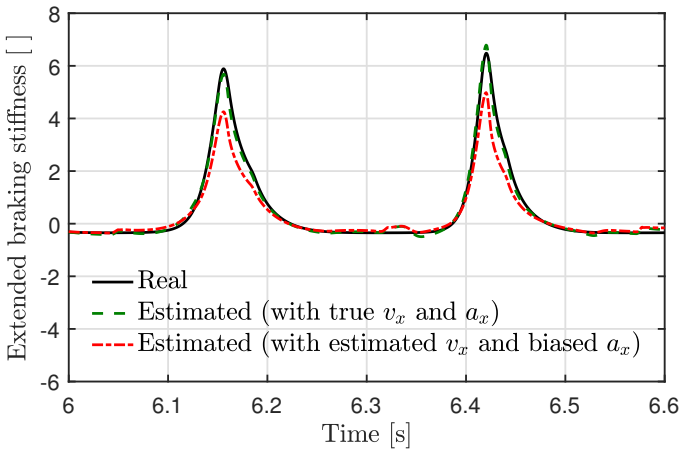

(b) Rear axle

Figure 3.18: Real vs estimated XBS: comparison of the results obtained using the true signals $v_x(t)$ and $a_x(t)$ against those obtained using the estimated vehicle speed and the acceleration perturbed by measurement bias.

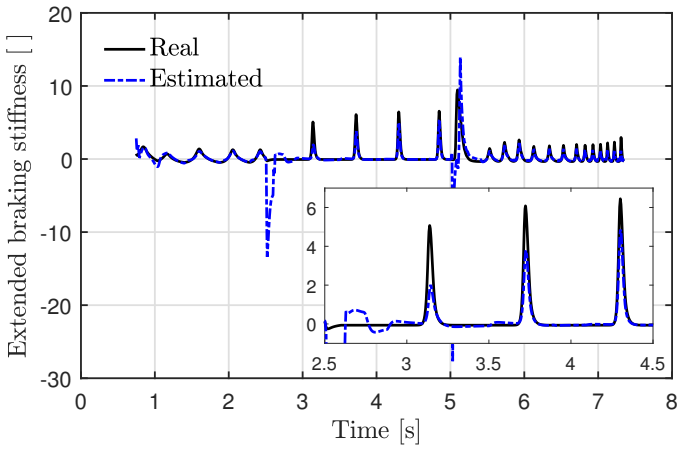

(a) Front axle

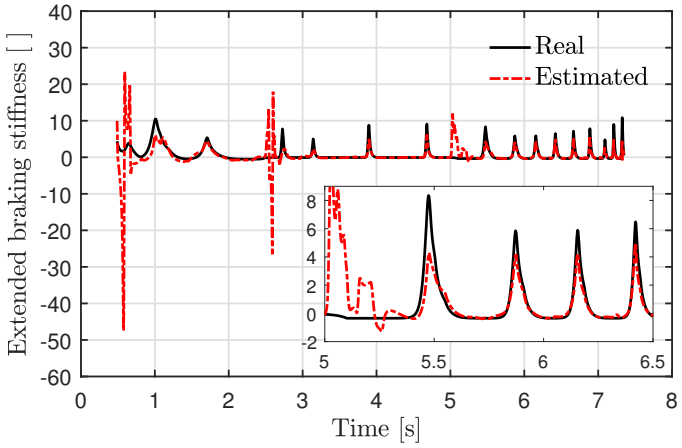

(b) Rear axle

Figure 3.19: Real vs estimated XBS of the front and rear wheels. The estimates are highly perturbed after the abrupt changes in road conditions at $t = 2.5$ s and $t = 5$ s, but they are able to re-approach their true values within 0.5 s after the perturbations.

are highly perturbed after the road transitions. However, they converge to their true values within 0.5 s past the perturbation.

3.7 Conclusion

In this chapter we presented a switched adaptive observer for the estimation of the tyre XBS. The design is based on a simplified dynamic model that retains a good degree of accuracy during an ABS-controlled braking scenario. The performance of the observer has been tested via numerical simulations and with experimental data from a tyre-in-the-loop test rig with satisfactory results. Moreover, the observer is able to recover a good estimate of the XBS even after large changes in road conditions and can be easily implemented in a real vehicle equipped with an ABS without the need of additional sensors.

The approach presented here has however an important limitation. Because of the conditions of Assumption 1 related to the PE and zero-crossing transversality of the measured output, the XBS observer might not be used, for instance, in conjunction with a controller that aims at regulating the trajectories of the system (3.1) at the origin. Yet, it is possible to exploit the XBS observer to improve the performance of ABS using hybrid control algorithms, in such a way that Assumption 1 be trivially satisfied. Our work in this direction is presented in Chapter 4.

4 ABS CONTROL BASED ON EXTENDED BRAKING STIFFNESS

In this chapter we address the control problem of the ABS. To that end, we first reformulate the (control) objective of the ABS as that of regulating the XBS to zero. For convenience, let us recall again the dynamic model

$$\dot{z}_1 = -\frac{a}{v_x(t)} z_1 z_2 - bu \tag{4.1a}$$

$$\dot{z}_2 = (cz_2 + d)\frac{1}{v_x(t)} z_1, \tag{4.1b}$$

where z_1 is the wheel acceleration offset and z_2 is the XBS.

4.1 CONTINUOUS CONTROL DESIGN

To simplify the control design, let us assume for the moment that both z_1 and z_2 are known. Under this assumption, we may design a control law that stabilizes system (4.1) at the origin. Note, however, that because the control input u does not appear explicitly in (4.1b), we must achieve the objective through z_1, that is, regarding the latter as a virtual control.

Hence, we first design a virtual reference z_1^* such that if $z_1 = z_1^*$, then $z_2 \to z_2^* = 0$. One such reference is

$$z_1^* = -k_r \frac{z_2}{cz_2 + d}, \qquad k_r > 0, \tag{4.2}$$

since, setting $z_1 = z_1^*$ in (4.1b) leads to $\dot{z}_2 = -k_r z_2 / v_x(t)$ which is exponentially stable (recall that $v_x(t)$ is separated from zero).

To perform the tracking of z_1^*, the control is designed as

$$u = \frac{1}{b}\left[-\frac{a}{v_x(t)} z_1 z_2 + \frac{k_p}{v_x(t)}(z_1 - z_1^*) - \dot{z}_1^*\right], \qquad k_p > 0, \tag{4.3}$$

where we employ (4.1b) in the evaluation of $\dot{z}_1^*$. Hence, the latter is implemented using z_1 and z_2 as

$$\dot{z}_1^* = -\frac{k_r}{v_x(t)} \frac{dz_1}{cz_2 + d}.$$

Note that, even though the right-hand side of (4.2) is not defined when $z_2 = -d/c$, this singularity lies outside the domain in which z_2 is physically possible. Indeed, z_2 satisfies $\mu'(0) \geq z_2 > -d/c$. Hence, z_1^* is well-posed.

Now, let $\tilde{z}_1 := z_1 - z_1^*$ and $\tilde{z}_2 = z_2 - z_2^*$. The substitution of (4.3) in (4.1a) yields the closed-loop dynamics

$$\begin{aligned}\dot{z}_1 &= \frac{k_p}{v_x(t)}\big(z_1^* - z_1\big) + \dot{z}_1^* \\ &= -\frac{k_p}{v_x(t)}\tilde{z}_1 + \dot{z}_1^*\end{aligned}$$

and, from (4.1b) and (4.2), we obtain

$$\begin{aligned}\dot{z}_2 &= \big(cz_2 + d\big)\frac{z_1^*}{v_x(t)} + \big(cz_2 + d\big)\frac{\tilde{z}_1}{v_x(t)} \\ &= -\frac{k_r}{v_x(t)}z_2 + \big(cz_2 + d\big)\frac{\tilde{z}_1}{v_x(t)}.\end{aligned}$$

Hence, the tracking error dynamics is

$$\dot{\tilde{z}}_1 = -\frac{k_p}{v_x(t)}\tilde{z}_1 \tag{4.4a}$$

$$\dot{\tilde{z}}_2 = -\frac{k_r}{v_x(t)}\tilde{z}_2 + \frac{c\tilde{z}_2 + d}{v_x(t)}\tilde{z}_1, \tag{4.4b}$$

which has a cascade structure. Let us recall that, for the origin of (4.4) to be GAS, it is enough that the origin for (4.4a) be GAS, that the origin for (4.4b) with $\tilde{z}_1 = 0$ be GAS, and that the solutions of (4.4) be uniformly globally bounded [86, 71].

Now, recalling that $v_x(t)$ is positive, bounded, and separated from zero, it follows that the origin of (4.4a) is GAS. The same holds for the origin of the unforced system

$$\dot{\tilde{z}}_2 = -\frac{k_r}{v_x(t)}\tilde{z}_2.$$

Moreover, note that because $z_2^* = 0$, the tracking error $\tilde{z}_2 = z_2$ is the XBS itself, which is bounded by nature. Thus, the interconnection term $\big(c\tilde{z}_2 + d\big)/v_x(t)$ is bounded and so are the solutions of (4.4). Therefore, it follows by a cascade argument that the origin of (4.4) is GAS.

The performance of this control law is illustrated in Fig. 4.1. Unless otherwise stated, in what follows we consider a simulation scenario of a vehicle braking on dry asphalt with an initial speed of 90 km/h. The graphics show the evolution of the system (solid line, blue) on the phase-plane for two different initial conditions (the trajectories labeled 'observer' will be discussed later on). Not surprisingly, the control law given by (4.2) and (4.3) is able to smoothly steer the system's trajectories towards the origin. We recall, however, that we have momentarily assumed that z_1 and z_2 are known, but in a real-time implementation z_2 cannot be directly measured. Hence, in order to implement the control law, an estimate $\hat{z}_2$ must be used instead.

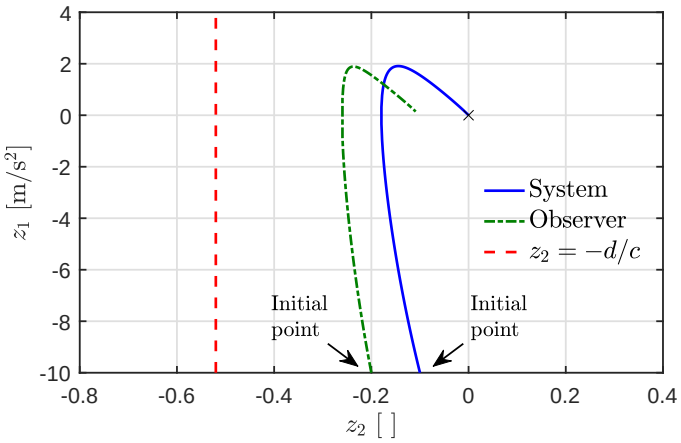

(a)

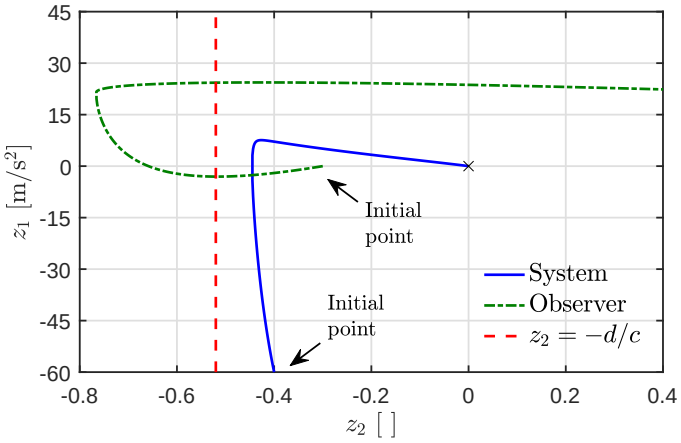

(b)

Figure 4.1: Continuous state-feedback control: the system converges to the origin. The estimated states, however, do not converge to their true values because $z_1 \to 0$ (hence, it is not persistently exciting). Moreover, in (b) the estimate $\hat{z}_2$ crosses the set $\{cz_2 + d = 0\}$ during the transient stage.

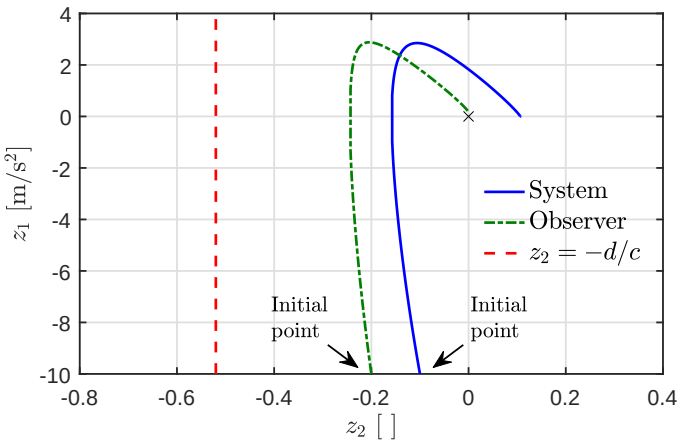

(a)

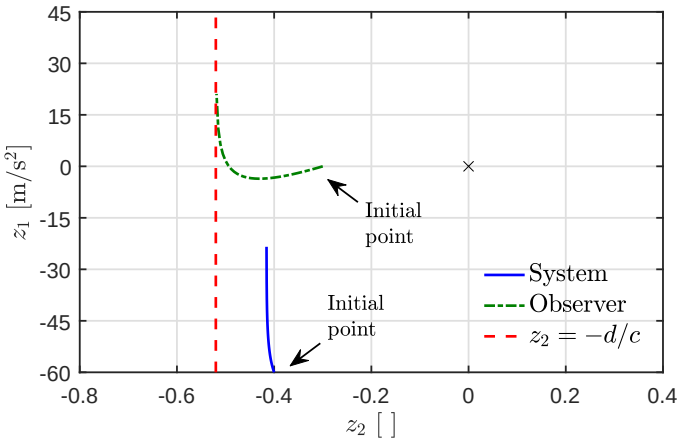

(b)

Figure 4.2: Continuous output-feedback control using the XBS observer: z_2 does not converge to its optimal value. (a) The estimated states do not converge to their true values because $z_1 \to 0$ (hence, it is not persistently exciting). (b) Even though the true trajectories of the system remain within the physically-possible region, as $\hat{z}_2$ approaches $-d/c$, the denominator of the right-hand side of (4.2) approaches zero and z_1^* grows unbounded. The simulation is stopped when a division by zero is detected.

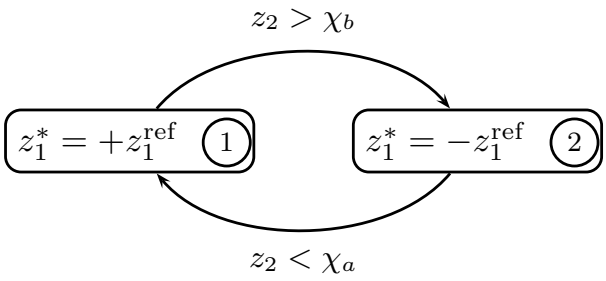

Figure 4.3: Two-phase regulation logic for z_1^*. The switching of the reference is performed based on the value of z_2.

Fig. 4.2 illustrates the performance of the controller when (4.2) and (4.3) are implemented using $\hat{z}_2$ instead of z_2. In both cases the control fails to drive the system towards the origin. This is caused by two problems: (*a*) the control law does not guarantee that z_1 is PE because $z_1 \to 0$, and (*b*) the observer does not guarantee that, for all t, $\hat{z}_2$ remains within the domain in which the control is well defined.

Consider again Fig. 4.1. The graphic shows the evolution of the observer (dash-dotted line, green) when the latter is implemented in parallel from the system-controller closed loop (in other words, the control is independent from the observer). In these cases, the trajectories $z_1(t)$ do not satisfy the PE condition (3.17) so the estimated states do not converge to their true values. For the initial conditions of Fig. 4.1(a), when the control is implemented in closed loop with the observer [Fig. 4.2(a)], this causes the system to converge to a point different than the origin. For the initial conditions of Fig. 4.1(b), during the transient stage $\hat{z}_2$ crosses into a region in which such a value of z_2 is not physically possible. Consequently, when the control is implemented in closed loop with the observer [Fig. 4.2(b)], the reference z_1^* grows unboundedly as $\hat{z}_2$ approaches $-d/c$. When $\hat{z}_2$ crosses the set $\{cz_2 + d = 0\}$ (dashed line, red), z_1^*, and therefore u, are no longer defined. To circumvent these problems, in the following section, we redefine the virtual reference z_1^* such that the PE condition (3.17) is satisfied.

4.2 HYBRID CONTROL DESIGN

To generate a function z_1^* such that z_1 is PE, we propose the two-phase regulation logic defined in Fig. 4.3, wherein z_1^{ref}, χ_a, and χ_b are (tunable) design parameters. The system's associated phase-portrait is illustrated in Fig. 4.4. The rationale behind this algorithm is as follows:

- We assume that the initial condition of the system is such that $z_1 < 0$ and $z_2 < 0$. That is, we assume that the wheel has entered the unstable region of the tyre; if it goes too far into this region, the wheel will lock down.

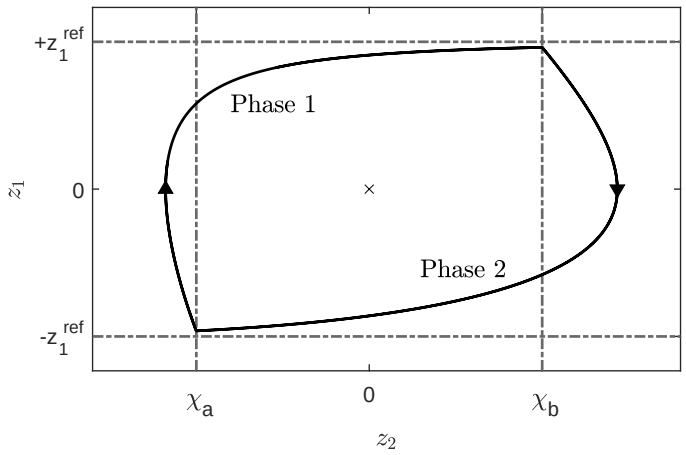

Figure 4.4: Limit cycle associated to the regulation logic of Fig. 4.3. The aim of the algorithm is to keep the system oscillating around the origin.

- During phase 1 the reference z_1^* is set to some positive value z_1^{ref}. The aim of this phase is to change the sign of the wheel acceleration offset and thus cause the wheel to return to the stable region of the tyre. Once z_1 becomes positive, z_2 starts to increase.
- As soon as z_2 crosses the threshold $\chi_b > 0$, phase 2 is triggered and the reference z_1^* is set to $-z_1^{\text{ref}}$. The aim of this phase is to prevent the wheel from going too far into the stable region, as this would result in a loss of friction force and thus in an increase of the braking distance. After the change of sign of z_1, the wheel goes back into the unstable region of the tyre and z_2 starts to decrease.
- As soon as z_2 crosses the threshold $\chi_a \leq 0$, phase 1 is triggered again and the cycle starts over.

The structure of this algorithm is similar to that of [18], in which the wheel acceleration is controlled to a positive or a negative reference during each phase using a proportional controller and the triggering of the phases is performed based on the measurement of the tyre longitudinal force. Nevertheless, unlike this approach, we do not assume that an additional sensor is available.

4.3 Analysis with known XBS

In this section we analyze the evolution of the trajectories $z_1(t)$ and $z_2(t)$ generated by the control algorithm of Fig. 4.3 and we establish sufficient conditions on k_p which guarantee asymptotic stability of the limit cycle of Fig. 4.4, provided that the XBS is known.

To simplify the analysis, we make use of the time-scale transformation (3.21) that was introduced in Section 3.2.1, that is

$$\frac{\mathrm{d}s}{\mathrm{d}t} = \frac{1}{v_x(t)}, \qquad s(0) = 0,$$

where s is the new time variable. As we have remarked already, because $v_x(t)$ is positive, bounded, and separated from zero, this transformation is well defined. Thus, without loss of generality, in what follows we consider the dynamics of the closed-loop system with respect to the s time-scale, i.e.

$$\frac{\mathrm{d}z_1}{\mathrm{d}s} = -k_p\big(z_1 - z_1^*\big) \tag{4.5a}$$

$$\frac{\mathrm{d}z_2}{\mathrm{d}s} = \big(cz_2 + d\big)z_1. \tag{4.5b}$$

Furthermore, we introduce the change of coordinates

$$\zeta_1 := \frac{z_1}{|z_1^*|}, \qquad \zeta_2 := \frac{z_2}{d\,|z_1^*|},$$

which allows us to study the evolution of the system separately for each phase of the limit cycle. To that end, in Sections 4.3.1 and 4.3.2, we make use of the concept of first integrals, which we then use, in Section 4.3.3, to construct a Poincaré map for the limit cycle.

4.3.1 PHASE 1

From (4.5), during phase 1 the dynamics of ζ_1 and ζ_2 is described by

$$\frac{\mathrm{d}\zeta_1}{\mathrm{d}s} = \alpha\,(1 - \zeta_1) \tag{4.6a}$$

$$\frac{\mathrm{d}\zeta_2}{\mathrm{d}s} = \zeta_1\,(1 + \beta\zeta_2), \tag{4.6b}$$

where we have defined $\alpha := k_p$ and $\beta := c\,|z_1^*|$.

A first integral (or integral of motion) of (4.6) is a function $\phi_1 : \mathbb{R}^2 \to \mathbb{R}$ that remains constant along any solution of (4.6), that is,

$$\frac{\mathrm{d}}{\mathrm{d}s}\phi_1(\zeta_1(s), \zeta_2(s)) = 0.$$

One such function is

$$\phi_1(\zeta_1, \zeta_2) = -\zeta_1 - \ln(1 - \zeta_1) - \frac{\alpha}{\beta}\ln\big(1 + \beta\zeta_2\big).$$

Hence, for any two points $(\zeta_1^\circ, \zeta_2^\circ)$ and (ζ_1', ζ_2') belonging to a solution of (4.6), we have

$$-\zeta_1' - \ln(1 - \zeta_1') - \frac{\alpha}{\beta}\ln\big(1 + \beta\zeta_2'\big) = -\zeta_1^\circ - \ln(1 - \zeta_1^\circ) - \frac{\alpha}{\beta}\ln\big(1 + \beta\zeta_2^\circ\big).$$

A direct computation yields

$$\big(1 - \zeta_1'\big) - \ln\big(1 - \zeta_1'\big) + \delta_1 = 0 \tag{4.7}$$

with

$$\delta_1 = \zeta_1^\circ + \ln\big(1 - \zeta_1^\circ\big) + \frac{\alpha}{\beta}\ln\left(\frac{1 + \beta\zeta_2^\circ}{1 + \beta\zeta_2'}\right) - 1. \tag{4.8}$$

4.3.2 PHASE 2

From (4.5), the dynamics of ζ_1 and ζ_2 is described during phase 2 by

$$\frac{\mathrm{d}\zeta_1}{\mathrm{d}s} = \alpha\,(-1-\zeta_1) \tag{4.9a}$$

$$\frac{\mathrm{d}\zeta_2}{\mathrm{d}s} = \zeta_1\,(1+\beta\zeta_2). \tag{4.9b}$$

A first integral of (4.9) is

$$\phi_2(\zeta_1,\zeta_2) = \zeta_1 - \ln(1+\zeta_1) + \frac{\alpha}{\beta}\ln\left(1+\beta\zeta_2\right).$$

Hence, for any two points (ζ_1', ζ_2') and (ζ_1'', ζ_2'') belonging to a solution of (4.9), we have

$$\zeta_1'' - \ln(1+\zeta_1'') + \frac{\alpha}{\beta}\ln\left(1+\beta\zeta_2''\right) = \zeta_1' - \ln(1+\zeta_1') + \frac{\alpha}{\beta}\ln\left(1+\beta\zeta_2'\right).$$

A direct computation yields

$$\left(1+\zeta_1''\right) - \ln\left(1+\zeta_1''\right) + \delta_2 = 0 \tag{4.10}$$

with

$$\delta_2 = -\zeta_1' + \ln\left(1+\zeta_1'\right) + \frac{\alpha}{\beta}\ln\left(\frac{1+\beta\zeta_2''}{1+\beta\zeta_2'}\right) - 1. \tag{4.11}$$

In the following section we use (4.7)–(4.8) and (4.10)–(4.11) to analyze the evolution of the system in the Phase-1-Phase-2 cycle.

4.3.3 LIMIT CYCLE

A basic mathematical tool to study planar limit cycles is the Poincaré map. The idea is to sample the solution of the system once per period according to an event-based or time-based rule, and then evaluate the stability properties of the sampled system. Thus, the Poincaré map transforms the analysis of periodic orbits of a system into the analysis of fixed points of a map (see Appendix A). In the case of hybrid systems, a standard approach to construct a Poincaré map is to select the transition between phases as the equivalent of a transverse section [79]. Thus, here we choose the transition at which phase 1 is triggered.

Consider the evolution of the system during one full cycle. Let $(\zeta_1^\circ, \zeta_2^\circ)$ in (4.7)–(4.8) and (ζ_1'', ζ_2'') in (4.10)–(4.11) be the starting and ending points of the corresponding trajectory of the system, and let (ζ_1', ζ_2') be the point at which the transition from phase 1 to phase 2 takes place. Thus,

$$\zeta_2^\circ = \zeta_2'' = \frac{\chi_a}{d\,|z_1^*|} =: \zeta_a$$

and

$$\zeta_2' = \frac{\chi_b}{d\,|z_1^*|} =: \zeta_b$$

are known. Our aim is to find a mapping P that maps a given (known) initial point ζ_1° to its corresponding return point ζ_1''.

The solutions of (4.7) and (4.10) are

$$1 - \zeta_1' = -W_0(-\exp(\delta_1)), \tag{4.12a}$$
$$1 + \zeta_1'' = -W_0(-\exp(\delta_2)), \tag{4.12b}$$

where $\exp(\cdot)$ denotes the exponential function and $W_0(\cdot)$ denotes the principal branch of the Lambert W function (see Appendix B). Thus, the Poincaré map is defined by

$$\zeta_1'' = P(\zeta_1^\circ) = \varphi_4 \circ \varphi_3 \circ \varphi_2 \circ \varphi_1(\zeta_1^\circ),$$

where $\circ$ denotes the composition of the functions

$$\varphi_1(\zeta_1^\circ) = \delta_1 = \zeta_1^\circ + \ln\left(1 - \zeta_1^\circ\right) - 1 + \alpha\kappa \tag{4.13a}$$
$$\varphi_2(\delta_1) = \zeta_1' = 1 + W_0(-\exp(\delta_1)) \tag{4.13b}$$
$$\varphi_3(\zeta_1') = \delta_2 = -\zeta_1' + \ln(1 + \zeta_1') - 1 + \alpha\kappa \tag{4.13c}$$
$$\varphi_4(\delta_2) = \zeta_1'' = -1 - W_0(-\exp(\delta_2)) \tag{4.13d}$$

and

$$\kappa = \frac{1}{\beta} \ln\left(\frac{1 + \beta\zeta_a}{1 + \beta\zeta_b}\right). \tag{4.14}$$

For further analysis, suppose that ζ_1° is a fixed point of the Poincaré map. Our aim now is to determine sufficient conditions on α such that ζ_1° is an attractive fixed point. To that end, consider the derivative of P at ζ_1°, that is

$$P'(\zeta_1^\circ) = \varphi_4'(\delta_2)\, \varphi_3'(\zeta_1')\, \varphi_2'(\delta_1)\, \varphi_1'(\zeta_1^\circ).$$

Because $z_1 < 0$ when phase 1 is triggered, $\zeta_1^\circ \in (-\infty, 0)$. Similarly, because $z_1 > 0$ when phase 2 is triggered, $\zeta_1' \in (0, +\infty)$. Moreover, from (4.13a) and (4.13c) it follows that $\delta_i \leq -1 + \alpha\kappa$, for $i = \{1, 2\}$. Because $\zeta_a < \zeta_b$ and $\ln(\cdot)$ is strictly monotone increasing, κ given by (4.14) is strictly negative. Hence, δ_i can be bounded from above by some arbitrary $\delta^{\text{up}} < -1$ by setting $\alpha \geq (\delta^{\text{up}} + 1)/\kappa$.

The derivative of (4.13a) is

$$\varphi_1'(\zeta_1^\circ) = \frac{\zeta_1^\circ}{\zeta_1^\circ - 1}.$$

Evaluating the above expression for $\zeta_1^\circ \in (-\infty, 0)$ we see that $\varphi_1'(\zeta_1^\circ) \in (0, 1)$. Hence,

$$\left|\varphi_1'(\zeta_1^\circ)\right| < 1. \tag{4.15}$$

The derivative of (4.13b) is

$$\varphi_2'(\delta_1) = \frac{-\exp(\delta_1)}{-\exp(\delta_1) + \exp(W_0(-\exp(\delta_1)))}.$$

Evaluating the above expression we see that φ_2' is strictly monotone decreasing and satisfies

$$\lim_{\delta_1 \to -\infty} \varphi_2'(\delta_1) = 0$$

whereas

$$\lim_{\delta_1 \to -1^-} \varphi_2'(\delta_1) = -\infty.$$

On the other hand, recall that δ_1 is bounded from above by δ^{up} provided that α is sufficiently large. Next, define $\varphi_2'(\delta^{\mathrm{up}}) =: -m$ so that $\delta_1 \in (-\infty, \delta^{\mathrm{up}}) \Rightarrow \varphi_2'(\delta_1) \in (-m, 0)$. The solution to the previous equation is

$$\delta^{\mathrm{up}} = \ln\left(\frac{m}{m+1}\right) - \frac{m}{m+1}.$$

Let $m \in (0,1)$. If $\alpha > (\delta^{\mathrm{up}} + 1)/\kappa$, then

$$\left|\varphi_2'(\delta_1)\right| < 1. \tag{4.16}$$

The derivative of (4.13c) is

$$\varphi_3'(\zeta_1') = -\frac{\zeta_1'}{1+\zeta_1'};$$

evaluating the above expression for $\zeta_1' \in (0, +\infty)$ we obtain that $\varphi_3'(\zeta_1') \in (-1, 0)$. Hence,

$$\left|\varphi_3'(\zeta_1')\right| < 1. \tag{4.17}$$

The derivative of (4.13d) is

$$\varphi_4'(\delta_2) = \frac{\exp(\delta_2)}{-\exp(\delta_2) + \exp(W_0(-\exp(\delta_2)))};$$

evaluating the above expression we see that φ_4' is strictly monotone increasing and satisfies

$$\lim_{\delta_2 \to -\infty} \varphi_4'(\delta_2) = 0$$

whereas

$$\lim_{\delta_2 \to -1^-} \varphi_4'(\delta_2) = +\infty.$$

Also, recall that δ_2 is bounded from above by δ^{up} and note that $\varphi_2'(\delta^{\mathrm{up}}) = -\varphi_4'(\delta^{\mathrm{up}})$. It follows that

$$\left|\varphi_4'(\delta_2)\right| < 1. \tag{4.18}$$

Thus, in view of (4.15), (4.16), (4.17), and (4.18), it follows that

$$\left|P'(\zeta_1^\circ)\right| < 1$$

and the limit cycle that contains ζ_1° is asymptotically stable [39, § 10.3].

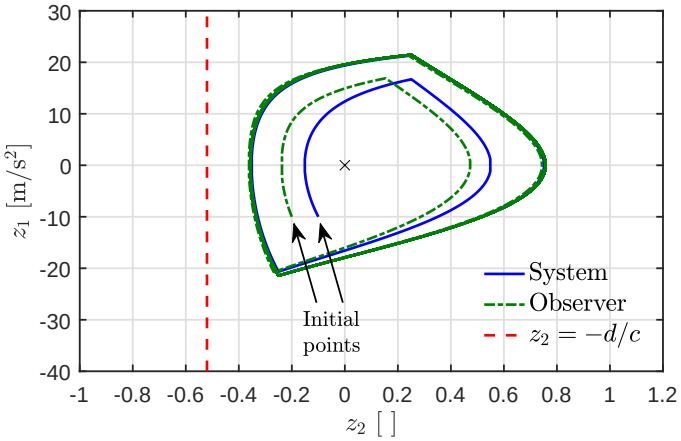

(a)

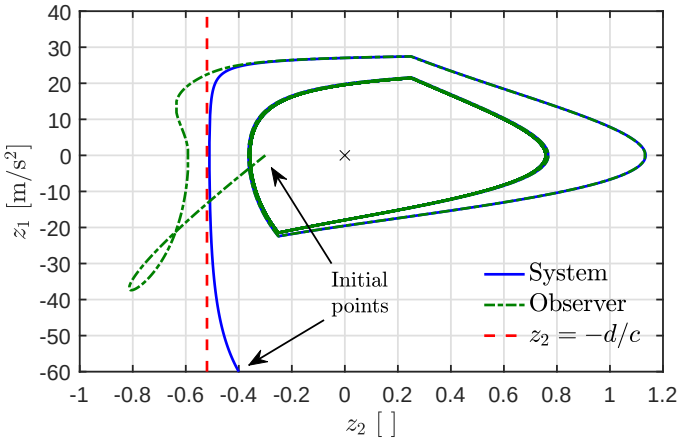

(b)

Figure 4.5: Hybrid state-feedback control: the system converges to a limit cycle around the origin.

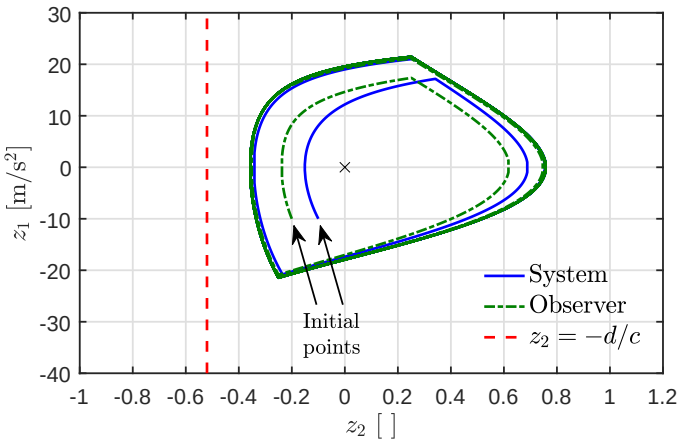

(a)

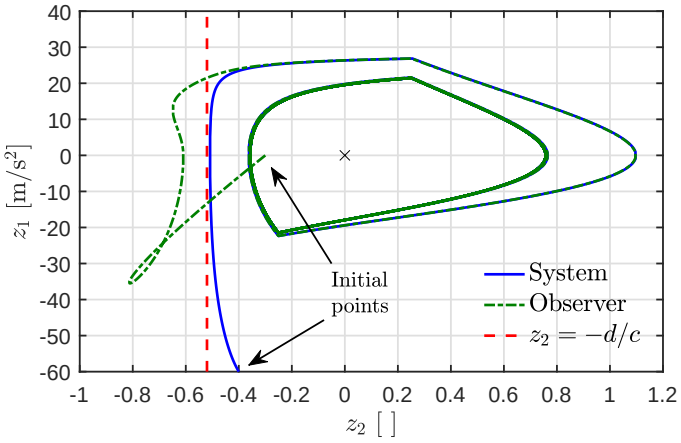

(b)

Figure 4.6: Hybrid output-feedback control using the XBS observer: the system converges to a limit cycle around the origin.

4.4 Simulation results

The performance of the hybrid control algorithm of Fig. 4.3 is illustrated in Fig. 4.5. The graphics show the phase-plane evolution of the system when the control law is implemented using state feedback. The initial conditions of the system and the observer as well as the design parameters are the same as those used to evaluate the continuous control. Because of the new definition of z_1^*, note that in the implementation of this algorithm we drop the last term of u given by (4.3) as $\dot{z}_1^* = 0$ almost everywhere. In both cases the control drives the system to a limit cycle around the origin. Moreover, because z_1 is PE, the observer (implemented in parallel from the system-controller closed loop) converges to the true trajectories of the system.

Fig. 4.6 illustrates the performance of the hybrid control law when it is implemented using $\hat{z}_2$ instead of z_2. Even though the system is perturbed during the transient stage because of the initial estimation error, the estimated states converge to the true trajectories of the system. Moreover, the hybrid con-

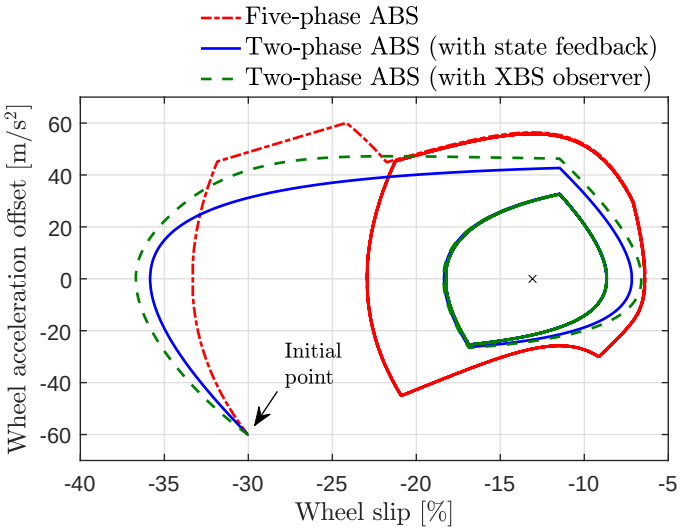

Figure 4.7: Comparison between the two-phase algorithm and the five-phase algorithm of [89]. The latter displays a larger variation of the wheel slip with respect to the optimal point.

trol shows robustness to $\hat{z}_2$ not staying within the physically-possible region. Hence, in all cases the control manages to drive the system towards a limit cycle around the origin, thus satisfying the control objective.

To ascertain the performance of the two-phase algorithm developed in this work and compare it against that of an algorithm that uses the same set of sensors, the five-phase algorithm of [89] based on wheel deceleration thresholds is taken as a reference. A qualitative comparison between these two algorithms is provided in Fig. 4.7. The graphic shows the phase-plane evolution of the system in the wheel slip domain for a vehicle braking on wet asphalt with an initial speed of 120 km/h. The results obtained with different initial speeds and road conditions are summarised in Table 4.1, which shows the braking distance l_{brake} computed as

$$l_{\text{brake}} = \frac{v_x(0)^2}{2g\bar{\mu}},$$

where g denotes the gravitational acceleration and $\bar{\mu}$ is the average friction coefficient obtained in each scenario. In all cases both algorithms manage to keep the system oscillating around the optimal braking point. With the two-phase algorithm, however, a smaller variation of the wheel slip with respect to its optimal value is obtained. In consequence, the average value of tyre-road friction coefficient is higher, and the braking distance is shorter than that of the five-phase algorithm. The reduction of the braking distance using the two-phase algorithm is especially noticeable at high speeds, in which a reduction of up to 1.5 m is obtained.

Even though, theoretically, the operating interval around zero could be made arbitrarily small, in any real-time implementation the choice of the different design parameters cannot be made arbitrarily. For the algorithm to work properly, the thresholds χ_b and χ_a must take into account the (typical) maximum

Road condition	Braking distance [m]		
	Five-phase ABS	Two-phase ABS	Difference
Travelling speed: 60 km/h			
Dry asphalt	12.31	12.18	−0.13
Wet asphalt	18.09	17.86	−0.23
Dry concrete	13.24	13.08	−0.16
Dry cobblestones	14.34	14.28	−0.06
Wet cobblestones	38.46	38.30	−0.16
Travelling speed: 120 km/h			
Dry asphalt	49.27	48.78	−0.49
Wet asphalt	72.38	71.58	−0.80
Dry concrete	52.97	52.40	−0.57
Dry cobblestones	57.34	57.11	−0.23
Wet cobblestones	153.88	153.41	−0.47
Travelling speed: 180 km/h			
Dry asphalt	110.87	109.90	−0.97
Wet asphalt	162.88	161.37	−1.51
Dry concrete	119.27	118.10	−1.17
Dry cobblestones	129.01	128.51	−0.50
Wet cobblestones	346.08	345.57	−0.51

Table 4.1: Braking distance: comparison between the two-phase and the five-phase algorithms.

and minimum values of XBS that can be attained in a certain type of road, as well as the possible error in the estimate $\hat{z}_2$. The reference z_1^{ref} should not be too small, as this would cause the algorithm to be very sensitive to the measurement noise in the wheel acceleration offset. Moreover, the gain k_p should be sufficiently large in order to guarantee asymptotic stability of the limit cycle.

4.5 CONCLUSION

In this chapter we presented a logic-based switching controller for the ABS. The switching thresholds are based on the value of the tyre XBS, which is estimated using the switched adaptive observer described in Chapter 3. The controller is designed so that the system's trajectories satisfy the conditions of Assumption 1, necessary for the estimation of the XBS. Sufficient conditions to guarantee the asymptotically stability of the limit cycle are established, provided that the wheel acceleration, the vehicle acceleration, and the XBS are known.

Part II

Wheel angular velocity and acceleration estimation

5 Preliminaries on velocity and acceleration measurement

In the previous chapters of this thesis, the wheel acceleration offset is considered as the system's measured output, thereby assuming that both the angular acceleration of the wheel and the longitudinal acceleration of the vehicle are measured. Although this assumption is reasonable in vehicles equipped with ABS, in practice these measurements are often perturbed by factors such as accelerometer bias (in the case of the vehicle longitudinal acceleration) and encoder imperfections (in the case of the wheel angular velocity and acceleration). In this chapter we address some problems related to the latter.

5.1 Incremental encoders

Real-time measurement of angular velocity and acceleration plays a crucial role in numerous control applications. For example, in the area of traction and brake control several vehicle-dynamics control systems rely on the measurement of the rotational speed of the wheels as the basic building block, making the wheel-speed sensor one of the most important sensors on a wheeled vehicle [34, 35].

The most commonly used technology to measure angular velocity and acceleration is based on incremental shaft encoders, i.e. transducers that convert the angular displacement of a shaft or axle into pulse-train signals. They consist, mainly, of two elements: a wheel with a built-in code-track that is attached to the rotating shaft, and a fixed pick-off sensor that detects the passing of the code-track and outputs a series of pulses as the shaft rotates. Thus, the velocity and acceleration are not directly measured, but reconstructed from the encoder pulses.

Among the available technologies to generate the output pulses, one can find encoders based on proximity sensors, conductive tracks, optical reflections, and magnetic field variations (see [24, § 6.2]). The principle of signal interpretation is identical for the four types of encoders just mentioned. In automotive applications, however, magnetic encoders are generally preferred because of

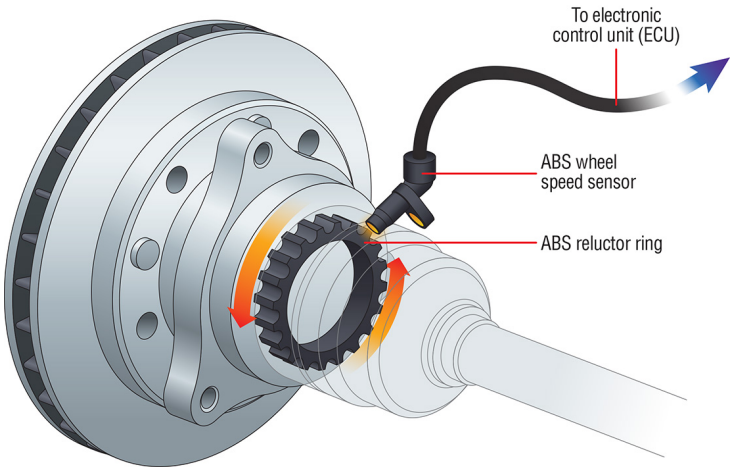

(a) Toothed wheel

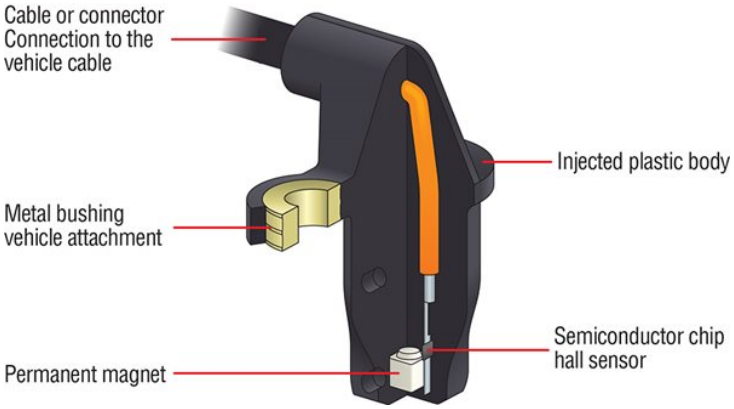

(b) Hall sensor

Figure 5.1: Structure of the magnetic incremental encoders used in ABS. Source of illustrations: [4].

their low cost, robustness, and reliability under harsh environmental conditions [117].

The structure of the encoders used in ABS is illustrated in Fig. 5.1. A steel toothed wheel (also called a pulse wheel or a reluctor ring) is attached to the hub, and a hall sensor is fixed on the vehicle chassis. A permanent magnet that is mounted next to the hall sensor generates a constant magnetic field. As the pulse wheel turns, the continuously alternating sequence of teeth and gaps induces corresponding fluctuations in the magnetic field. The fluctuations are detected by the hall sensor and converted into a square-wave signal in which each edge corresponds to the edge of one tooth.

Several algorithms have been proposed to estimate velocity or acceleration from encoder measurements (see [7] and [98] for comprehensive reviews on the state-of-the-art), which can be classified either as *model-based* or as *signal-based* approaches. The former are well suited for applications for which simple and fairly accurate models exist, such as electrical motors. In automotive applications, however, the wheel dynamics is affected by the highly nonlinear and un-

certain tyre-road friction coefficient, hence the latter are usually preferred [101, appx. B].

In the next section we present the outline of a signal-based approach known as the time-stamping algorithm (TSA), which is used throughout this work to reconstruct angular velocity and acceleration from the output pulses of an incremental encoder.

5.2 TIME-STAMPING ALGORITHM

The TSA [75, 76] is closely related to the Savitzky-Golay filter [104] (see also [105, 106]) and the least squares fit observer [11]. It consists in capturing, via a high-resolution clock, the time instants in which the edges of the encoder pulses are detected, and using the information of the last n edges to approximate the evolution of the angular position with a polynomial of order m. Each edge detection is called an encoder event.

Let t_i and θ_i denote the time instant and position corresponding to the ith encoder event, and let k be the index of the most recent event. The position θ at the current time t is modelled as

$$\theta(t) = p_m\, t^m + p_{m-1}\, t^{m-1} + \ldots + p_0, \tag{5.1}$$

where the coefficients $p_0, \ldots, p_m$ are unknown. A regression problem is formulated for the last n events as

$$Ax = b \tag{5.2}$$

where $A \in \mathbb{R}^{n\times(m+1)}$, $x \in \mathbb{R}^{m+1}$, and $b \in \mathbb{R}^n$ are given by

$$\begin{aligned} A &= \begin{bmatrix} t_{k-n+1}^m & t_{k-n+1}^{m-1} & \cdots & t_{k-n+1} & 1 \\ \vdots & \vdots & \vdots & \vdots & \vdots \\ t_k^m & t_k^{m-1} & \cdots & t_k & 1 \end{bmatrix}, \\ x &= \begin{bmatrix} p_m & p_{m-1} & \cdots & p_1 & p_0 \end{bmatrix}^\top, \\ b &= \begin{bmatrix} \theta_{k-n+1} & \cdots & \theta_k \end{bmatrix}^\top. \end{aligned}$$

Given $n > m \geq 2$, (5.2) is solved for x, in the least-squares sense, as

$$x = (A^\top A)^{-1} A^\top b. \tag{5.3}$$

Estimates of the angular velocity ω and acceleration α are then obtained via analytic differentiation of (5.1) with respect to time, as

$$\omega(t) = \sum_{i=1}^{m} i\, p_i\, t^{i-1} \tag{5.4}$$

and

$$\alpha(t) = \sum_{i=2}^{m} (i-1)\, i\, p_i\, t^{i-2}. \tag{5.5}$$

Remark 2. *For implementation purposes, in order to prevent numerical problems during the execution of the TSA, the time instants of the last n events are scaled to* $[0, 1]$ *in every sampling time of the controller. This scaling improves the numerical properties of A and hence the accuracy of* (5.3)*. Further discussion on this topic is given in Appendix C.*

In what follows, the order of the polynomial is set to $m = 2$. Under this choice, the algorithm presented here is equivalent to the one described in [31, appx. 1], which has been shown to yield a good performance in automotive applications.

5.3 Encoder imperfections and their effects

An ideal incremental encoder is characterized by identical and equidistant teeth (or, in optical encoders, slits) distributed over the encoder's code-track and, in the case of quadrature encoders, by two symmetrical output channels 90 degrees out of phase. That is, an ideal encoder is characterized by equally-spaced edge transitions of the output pulses. In real devices, however, well-known manufacturing and assembly imperfections introduce variations in the location of the edge transitions from their expected values.

Generated by these imperfections, the most significant error sources in the encoder output signals are [76]:

1) cycle error, i.e. stochastic variations of the edge transitions due to non-identical and unequally-distributed teeth, as well as limitations and irregularities of the encoder's signal generation and sensing hardware;
2) pulse-width error, generated when the duty cycle of the output pulses is not exactly symmetrical;
3) phase error, generated when the phase between the two channels is not exactly 90 degrees; and
4) eccentricity or tilt of the encoder's code-track due to concentricity and assembly tolerances. The primary contributions to this error source are shaft, assembly, and track eccentricities, as well as radial play (see [24, § 6.7.1]).

These error sources have been thoroughly analyzed in [51, 52, 53], where it is shown that they can be classified as differential and integral nonlinearities, and hence be modelled as two independent additive perturbations. The first three error sources correspond to differential nonlinearities, also termed 'transition noise'. When viewed over the circumference of the encoder's code-track, they appear as random high-frequency variations of the edge transition locations from their ideal values. The fourth error source corresponds to an integral nonlinearity. When viewed over the circumference of the encoder's code-track, it introduces a systematic low-frequency variation with a period of one mechanical revolution. The effects of these nonlinearities are further discussed in the following sections.

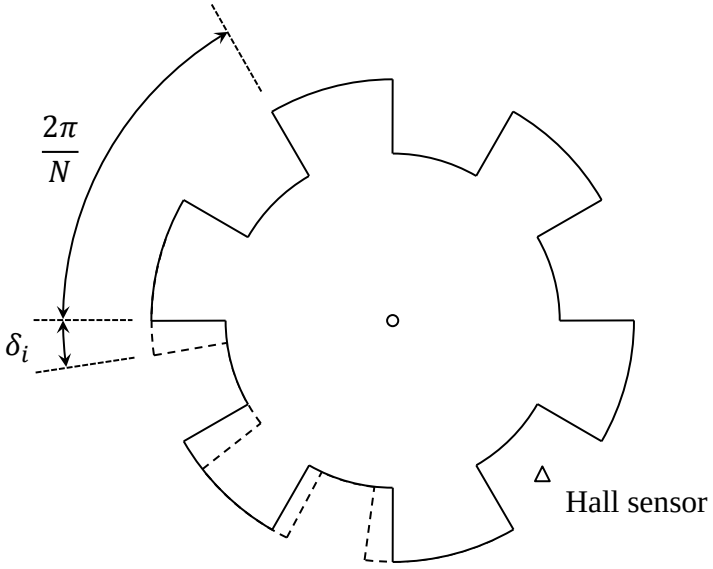

(a) Nonideal teeth

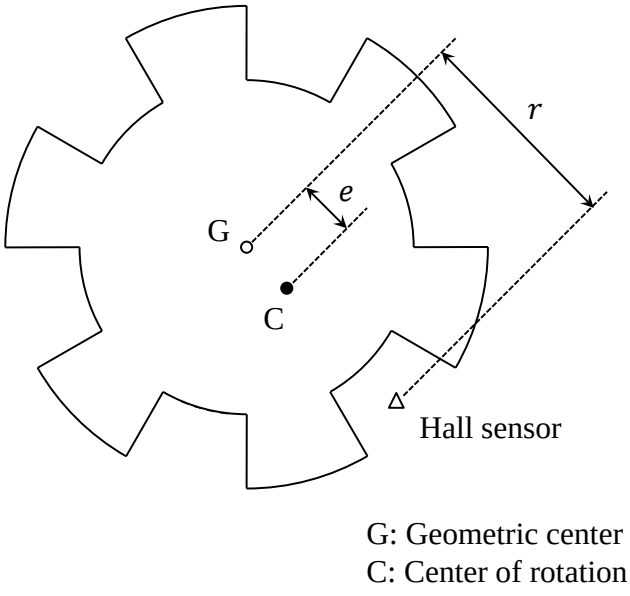

(b) Eccentricity

Figure 5.2: Illustration of encoder imperfections.

5.3.1 Effects of differential nonlinearities

Let θ_i^{nom} denote the ideal edge transition location of the ith tooth over the encoder's code-track given by

$$\theta_i^{\text{nom}} = (i-1)\tfrac{2\pi}{N}, \quad i = 1, \ldots, N$$

where N is the number of pulses per revolution of the encoder. It has been established in [52] that the influence of differential nonlinearities can be accurately modelled by an additive noise process uniformly distributed over $[-\epsilon, +\epsilon]$, where ϵ represents the maximum deviation of the location at which an edge transition may occur. The corresponding actual transition locations, i.e. the positions at which a change in the quantized position code occurs, are given by

$$\theta_i^{\text{act}} = \theta_i^{\text{nom}} + \delta_i \tag{5.6}$$

where $\delta_i \in [-\epsilon, +\epsilon]$ is the transition location error of the ith tooth with respect to its nominal value —see Fig. 5.2(a).

5.3.2 Effects of integral nonlinearities

Consider an encoder with code-track radius r which, for most practical purposes, can be taken as the disc radius. The eccentricity e of an encoder is defined as the distance between the geometric center G of the code-track and its center of rotation C —see Fig. 5.2(b).

From the law of sines, the difference between the true angle of rotation θ_r and the corresponding measurement θ_m is

$$\theta_m - \theta_r = \arcsin\left\{\frac{e}{r}\sin\left(\theta_r + \varphi\right)\right\}, \tag{5.7}$$

where φ denotes an offset angle relative to the (arbitrarily) selected reference. If $e/r \ll 1$, a condition which is reasonable to assume in practical scenarios, then the small-angle approximation $\arcsin\{\frac{e}{r}\} \approx \frac{e}{r}$ holds. Hence, from (5.7) the measured position may be modelled as

$$\theta_m \approx \theta_r + \frac{e}{r}\sin\left(\theta_r + \varphi\right). \tag{5.8}$$

5.3.3 Effects of differential and integral nonlinearities

The effects of differential and integral nonlinearities on position measurement are illustrated in Fig. 5.3, which shows the error in edge-transition locations as a function of angular position for a 60-pulses-per-revolution (ppr) and a 1024-ppr encoder. These graphics were obtained using the experimental setup described in Section 6.3. The shaft of the encoders was rotated at a (theoretically) constant velocity and the time instants at which each edge transition was detected were stored and compared against the ideal time instants at which the edge

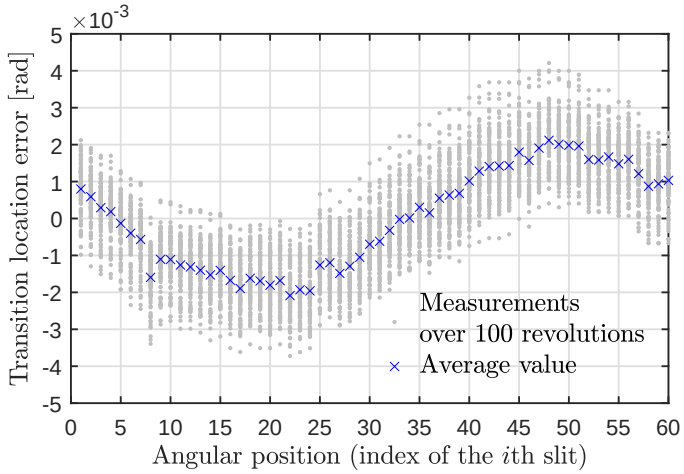

(a) 60-ppr encoder

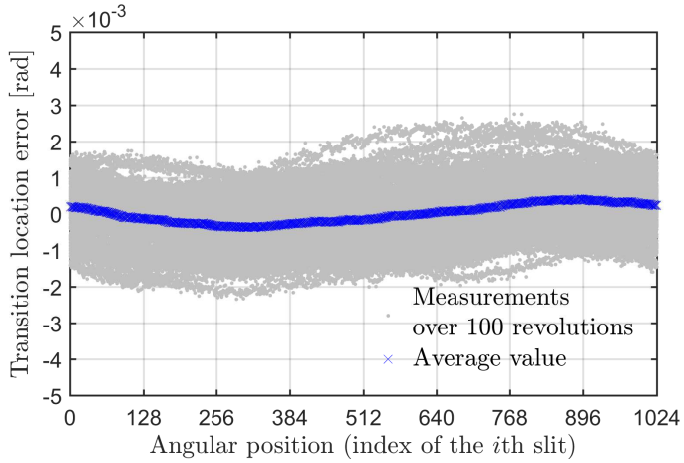

(b) 1024-ppr encoder

Figure 5.3: Error in edge transition location as a function of angular position for a low-resolution and a high-resolution encoder.

transitions would have occurred if the encoders were perfect. The transition-location error was then computed via a least-squares fitting of the time-instant error and the theoretical value of the shaft velocity. For the ith encoder slit, each dot represents the error measured at one of a total of 100 revolutions, and the cross represents the average value of the error corresponding to that slit. Both a systematic low-frequency variation and a stochastic high-frequency variation of the transition locations can be observed, thus fitting the postulation of the two distinct and independent error sources described by (5.6) and (5.8).

The effects of the encoder imperfections on velocity and acceleration measurement are illustrated in Fig. 5.4. The graphic shows the measurements obtained via the TSA for an experiment with a constant reference of 1020 rpm using different numbers of events. Note that, because the execution of the TSA is feasible only after the first n events have been captured, the measured signals are not available at the beginning of the experiment. A clear periodicity can be observed in all cases. It can be noted as well that the amount of high-frequency

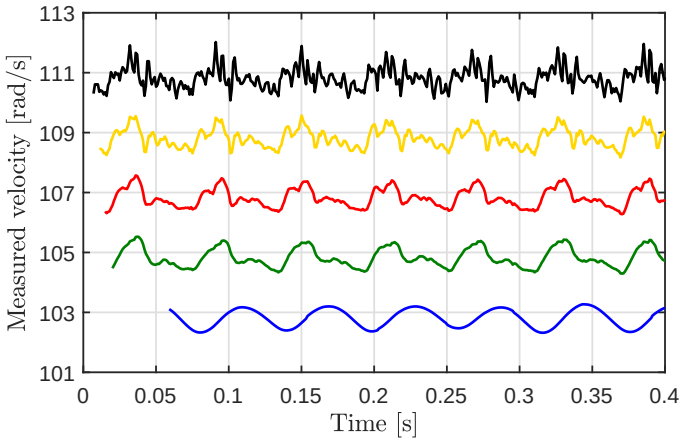

(a) Velocity: 6 events (black, offset $= 4$ rad/s), 10 events (yellow, offset $= 2$ rad/s), 15 events (red), 20 events (green, offset $= -2$ rad/s), 60 events (blue, offset $= -4$ rad/s).

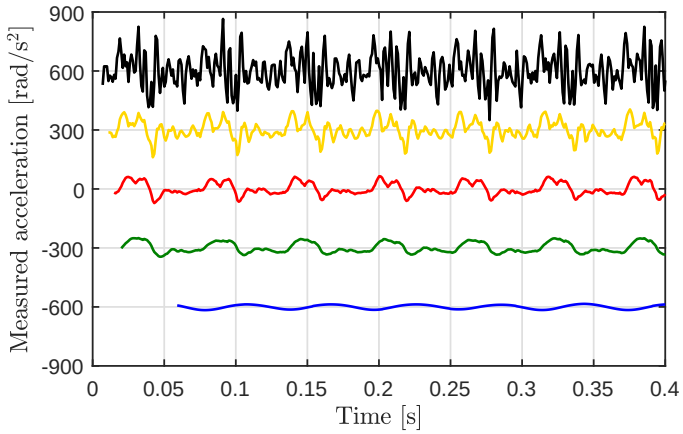

(b) Acceleration: 6 events (black, offset $= 600$ rad/s^2), 10 events (yellow, offset $= 300$ rad/s^2), 15 events (red), 20 events (green, offset $= -300$ rad/s^2), 60 events (blue, offset $= -600$ rad/s^2).

Figure 5.4: Velocity and acceleration measured via the TSA for a 1020 rpm (≈ 107 rad/s) constant-velocity reference using a 60-ppr encoder and different numbers of events (an offset is added to each signal for the sake of clarity).

variations that appear in the measured signals is directly related to the number n of encoder events used in the estimation. Not surprisingly, because we are using a second-order parabola to approximate the position history, the more angle/time points are used in the polynomial fit, the less the measured velocity and acceleration signals are prone to be affected by high-frequency transition location errors —see [105, Fig. 4]. This filtering effect introduces however an important phase lag when n is too large, which hampers the ability of the TSA to capture small variations in the real signals and to accurately reflect large sudden variations.

Our objective in this thesis is to obtain better estimates of the angular velocity and acceleration of the wheel, that is, to remove the periodic perturbations introduced by the encoder imperfections without introducing a phase lag. To

put our contribution in perspective, in Section 5.4 we give a short account of the state of the art. Our main results are presented in Chapter 6.

5.4 Literature review on the compensation of encoder imperfections

In an academic context, the inexact encoder readings induced by sensor imperfections can be compensated using error look-up tables (see, e.g. [112, 76]). However, these are suited solely for a particular encoder and their construction requires the availability of a high-resolution reference sensor. In an industrial context, error estimation and compensation approaches have been proposed, but they work only when the speed is constant (see, e.g. [35]) or does not vary significantly within one revolution (see, e.g. [93]).

The available literature (cited in Sections 5.1, 5.2, and 5.3) shows that, on the one hand, the problem of rotational velocity and acceleration estimation from ideal incremental encoder measurements is well-addressed and, on the other hand, the most significant error sources in the encoder output signals caused by sensor imperfections are well-known. However, to the best of our knowledge, only a small number of works have addressed the issue of the effects of encoder imperfections on the velocity and acceleration estimation using real-time filters.

The presence of periodic disturbances with a period of one mechanical revolution was noticed in [21] in the context of experimental identification of engine-to-slip dynamics in a sport motorbike. An offline zero-phase adaptive notch-filter-based scheme was used to remove the first harmonic component of the velocity of the wheels. The causes of the disturbances were later identified in [88] and the adaptive notch-filter was applied in real time. Similarly, the phenomenon was noticed in wheel acceleration measurements in [31], in the context of experimental validation of a five-phase ABS algorithm. A dynamic notch filter was proposed in [40] to eliminate the periodic disturbances on the wheel acceleration and the effect of this filter on the delay margin of the system's feedback loop was analysed.

More recently, a method to remove the wheel-speed disturbances caused by sensor imperfections was proposed in [93] to estimate the pedaling cadence in an electric bicycle. Under the assumption that the true speed is well approximated by the mean revolution speed (which does not hold, e.g. during sudden braking scenarios), a constrained batch least squares formulation was used to recursively estimate and compensate for the geometric errors of the toothed wheel of the encoder.

In this work, we are interested in the estimation of the wheel angular velocity and acceleration for automotive applications such as the ABS. It should be noted, however, that the domain of application of our contribution is by no means restricted to the automotive field. In the next chapter we introduce three models that capture the effects of sensor imperfections on the measured position, velocity, and acceleration signals. By combining these models with the

features of the TSA, we propose a method to identify and remove the periodical disturbances introduced by sensor imperfections. Rather than filtering out only the first harmonic component of the disturbances as in the previous references, the aim of our approach is to identify a given number of harmonic components and to use that information to recover reliable estimates of the velocity and acceleration of the shaft.

6 VELOCITY AND ACCELERATION ESTIMATION

In this chapter we present an algorithm to estimate the wheel angular velocity and acceleration and remove the periodical perturbations caused by the encoder imperfections. To that end, we first develop three measurement models that capture the effects of the imperfections on the signals measured via the TSA.

6.1 MEASUREMENT MODELS

The arguments given in Section 5.3 and the experimental data that is shown in Fig. 5.3, naturally lead us to model the effects of sensor imperfections using a 2π-periodic function, that we denote $\theta_r \mapsto f_r$, added to the real position θ_r. Hence the measured position θ_m corresponds to

$$\theta_m = \theta_r + f_r(\theta_r). \tag{6.1}$$

If the function f_r is approximated using a finite number M_r of Fourier coefficients, we have

$$\theta_m = \theta_r + \sum_{k=1}^{M_r} \left[a_k^r \sin(k\theta_r) + b_k^r \cos(k\theta_r) \right].$$

In what follows, we assume that both $a_k^r \ll 1$ and $b_k^r \ll 1$. Indeed, even for high-quality sensors, the error ϵ due to transition noise is often between 0.002 and 0.05 encoder cycles [50], whereas the eccentricity e of the code-track is often between 0.05 and 0.25 mm [61]. Hence, this condition is always satisfied if the encoder is of reasonable quality and if the sensor has been correctly mounted on its shaft.

The fact that θ_r is unknown limits the applicability of the previous model. Nevertheless, when the perturbation f_r is sufficiently small, the function φ_r that maps θ_r to θ_m through (6.1) is invertible. Denoting this inverse by φ_m, we have

$$\theta_m = \theta_r + f_r \circ \varphi_m(\theta_m),$$

where $\circ$ denotes the function composition operator. Defining $f_m = f_r \circ \varphi_m$, we obtain

$$\theta_m = \theta_r + f_m(\theta_m).$$

The function f_m is also 2π-periodic. Note, however, that the Fourier coefficients of a finite approximation of f_m, given by

$$\theta_m = \theta_r + \sum_{k=1}^{M} \left[a_k \sin(k\theta_m) + b_k \cos(k\theta_m) \right], \tag{6.2}$$

are in general different from those of f_r, even when $M = M_r$. Actually, in general $M \neq M_r$ and it might be necessary to take $M > M_r$ to obtain a good approximation.

The new approximation (6.2) is the starting point for our estimation algorithm. The differentiation with respect to time of the expression above leads to the velocity and acceleration measurement models

$$\omega_m = \omega_r + \omega_m \sum_{k=1}^{M} \left[k a'_k \cos(k\theta_m) - k b'_k \sin(k\theta_m) \right] \tag{6.3}$$

and

$$\begin{aligned} \alpha_m = \alpha_r &+ \alpha_m \sum_{k=1}^{M} \left[k a''_k \cos(k\theta_m) - k b''_k \sin(k\theta_m) \right] \\ &- \omega_m^2 \sum_{k=1}^{M} \left[k^2 a''_k \sin(k\theta_m) + k^2 b''_k \cos(k\theta_m) \right], \end{aligned} \tag{6.4}$$

in which the Fourier coefficients a'_k, b'_k, a''_k and b''_k are unknown. Hence, our goal is to estimate the Fourier coefficients in order to recover reliable estimates of ω_r and α_r.

Remark 3. *The notation $(\cdot)'$ and $(\cdot)''$ is used here in order to emphasize that the Fourier coefficients are different in* (6.2), (6.3), *and* (6.4) *because ω_m (resp. α_m) does not correspond to the derivative of θ_m (resp. ω_m), but it is obtained by using the TSA. This fact is illustrated in Fig. 6.1, where we show the values of a_k and b_k obtained via an offline least-squares fitting of the models* (6.2), (6.3), *and* (6.4) *with the data of the 1020-rpm experiment (Fig. 5.4) using 15 events. It can be observed that the fitted values of a_k and b_k vary when the fitting is performed using the different models, especially for the low-order harmonics.*

In the experiments associated to Figs. 5.3, 5.4, and 6.1 below, an evaluation of the quality of these models as a function of the number of harmonics M seems to indicate that the fit between data and the model improves until $M = \lceil N/n \rceil + 1$, where N is the number of pulses per revolution of the encoder, n is the number of events used in the fit, and $\lceil \cdot \rceil$ denotes the smallest integer greater than or equal to the argument. Based on (6.3) and (6.4), an algorithm to reduce the periodic noise present in the measured signals can be designed as discussed in the following section.

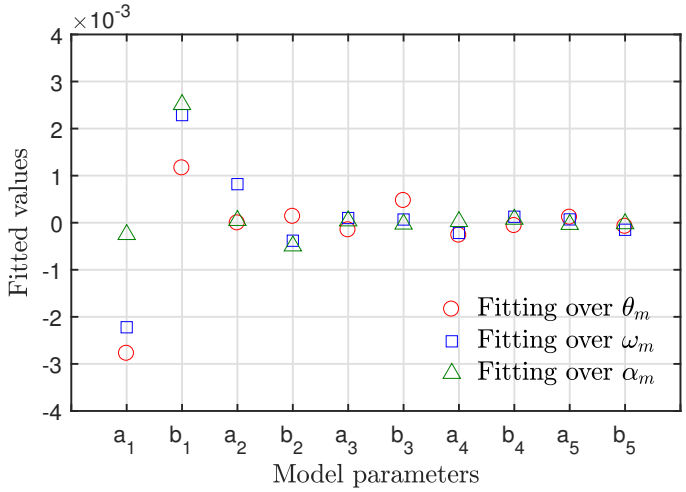

Figure 6.1: Off-line least-squares fitting of the Fourier coefficients a_k and b_k for the measurement models (6.2), (6.3), and (6.4), using $n = 15$ and $M = 5$.

6.2 Estimation algorithm

Let us rewrite (6.3) and (6.4) as

$$\omega_m = \omega_r + \omega_m \phi(\theta_m)^\top D \vartheta' \tag{6.5}$$

and

$$\alpha_m = \alpha_r + \left[\alpha_m \phi(\theta_m)^\top D - \omega_m^2 \psi(\theta_m)^\top D^2\right] \vartheta'', \tag{6.6}$$

where $D \in \mathbb{R}^{2M \times 2M}$, $\phi, \psi \in \mathbb{R}^{2M}$ are defined as

$$D = \operatorname{diag}[1, 1, 2, 2, \ldots],$$

$$\phi(\theta_m) = \begin{bmatrix} \cos(\theta_m) & -\sin(\theta_m) & \cos(2\theta_m) & -\sin(2\theta_m) & \cdots \end{bmatrix}^\top,$$

$$\psi(\theta_m) = \begin{bmatrix} \sin(\theta_m) & \cos(\theta_m) & \sin(2\theta_m) & \cos(2\theta_m) & \cdots \end{bmatrix}^\top,$$

and $\vartheta', \vartheta'' \in \mathbb{R}^{2M}$ contain the corresponding coefficients a_k', b_k', a_k'' and b_k''.

According to these models, provided that the frequencies of vehicle velocity and acceleration variations are much lower than those of the wheel harmonics, the measured velocity ω_m and the measured acceleration α_m can be seen as the sum of a low-frequency term —ω_r in (6.5) and α_r in (6.6)— and a high-frequency (with respect to the first one) term $\Phi(\theta_m, \omega_m, \alpha_m)^\top \vartheta$, where $\Phi \in \mathbb{R}^{2M}$ depends on the known signals θ_m, ω_m, and α_m, and is linear in the unknown parameters $\vartheta \in \mathbb{R}^{2M}$. More precisely, we use

$$\Phi = \begin{cases} D\phi(\theta_m)\omega_m & \text{for the model (6.5)} \\ D\phi(\theta_m)\alpha_m - D^2\psi(\theta_m)\omega_m^2 & \text{for the model (6.6),} \end{cases}$$

and

$$\vartheta = \begin{cases} \vartheta' & \text{for the model (6.5)} \\ \vartheta'' & \text{for the model (6.6).} \end{cases}$$

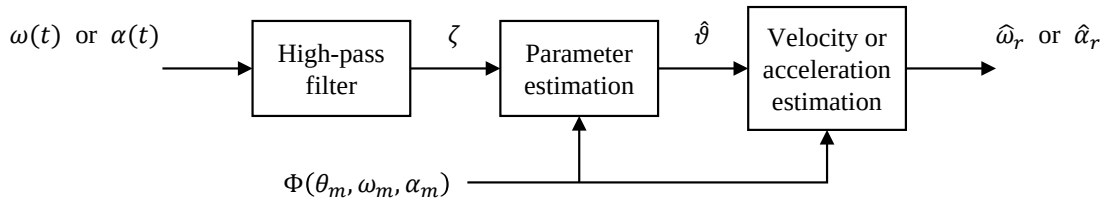

Figure 6.2: Three-stage velocity and acceleration estimation scheme. The input signals $\omega(t)$ and $\alpha(t)$ are those obtained from the TSA —see (5.4) and (5.5).

In order to estimate the real velocity (resp. acceleration), we perform the three-stage algorithm illustrated in Fig. 6.2. In the first stage, in order to separate $\Phi(\theta_m, \omega_m, \alpha_m)^\top \vartheta$ from the other terms in (6.5) (resp. (6.6)), the measured signal is filtered using a first-order high-pass filter with a cutoff frequency that is considerably below that of the wheel revolution (for example 1 Hz).

In the second stage, assuming that the filters are ideal and they completely eliminate the low-frequency term of the measured signals, the Fourier coefficients of the periodic perturbation in (6.5) (resp. (6.6)) are estimated using the parametric model

$$\zeta = \Phi(\theta_m, \omega_m, \alpha_m)^\top \vartheta \tag{6.7}$$

via the normalized recursive least-squares algorithm with forgetting factor [45, Ch. 4]:

$$\dot{\widehat{\vartheta}} = -\Gamma \Phi \varepsilon, \qquad \widehat{\vartheta}(0) = \widehat{\vartheta}_0 \tag{6.8a}$$

$$\dot{\Gamma} = \beta\Gamma - \frac{\Gamma\Phi\Phi^\top\Gamma}{1 + \kappa\Phi^\top\Phi}, \qquad \Gamma(0) = \Gamma_0 = \Gamma_0^\top > 0 \tag{6.8b}$$

$$\varepsilon = \frac{\Phi^\top\widehat{\vartheta} - \zeta}{1 + \kappa\Phi^\top\Phi}, \tag{6.8c}$$

where $\widehat{\vartheta} \in \mathbb{R}^{2M}$, $\Gamma \in \mathbb{R}^{2M\times 2M}$, $\varepsilon \in \mathbb{R}$, and κ and β are positive constants.

Note that due to the form of the parametric model (6.7) any other standard algorithm may be used. Note as well that, due to the form of $\phi(\theta_m)$, $\psi(\theta_m)$, and D, the real-time implementation of the RLS algorithm can be greatly simplified, especially for large values of M. That is, the term $\Phi^\top\Phi$ in (6.8b) and (6.8c) simplifies to

$$\Phi^\top\Phi = \begin{cases} \varsigma_2\omega_m^2 & \text{for velocity estimation} \\ \varsigma_2\alpha_m^2 + \varsigma_4\omega_m^4 & \text{for acceleration estimation} \end{cases}$$

where $\varsigma_2 = \sum_{k=1}^{M} k^2$ and $\varsigma_4 = \sum_{k=1}^{M} k^4$. Also, note that the regressor Φ contains M frequencies, that is, it is sufficiently rich to estimate the $2M$ unknown parameters [45, Ch. 5].

Finally, using the estimated parameters $\widehat{\vartheta}$, we construct our velocity estimate as

$$\widehat{\omega}_r = \omega_m - \omega_m\phi(\theta_m)^\top D\widehat{\vartheta}'$$

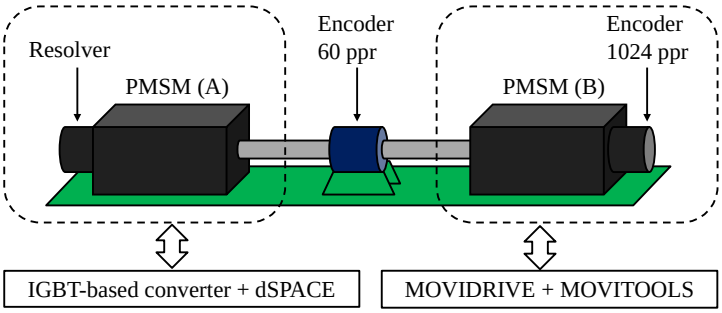

Figure 6.3: Experimental setup. The low-resolution 60-ppr encoder and the high-resolution 1024-ppr encoder are those characterized in Fig. 5.3.

and our acceleration estimate as

$$\widehat{\alpha}_r = \alpha_m - \left[\alpha_m \phi(\theta_m)^\top D - \omega_m^2 \psi(\theta_m)^\top D^2\right] \widehat{\vartheta''}.$$

6.3 Experimental validation

The performance of the estimation algorithm has been evaluated using a test rig from the SATIE-TEMA laboratory of IFSTTAR. The experimental setup is illustrated in Fig. 6.3. It consists of two identical three-phase synchronous motors coupled via a torque transducer. The motor A has a built-in 2-pole resolver; it is driven by an IGBT[1]-based converter and a dSPACE DS1006 processor board. The motor B has a built-in 1024-ppr encoder; it is driven by a MOVIDRIVE inverter and the MOVITOOLS MotionStudio software from SEW-EURODRIVE. For the tests presented in this paper, the motor B was used as an active torque generator and the motor A as a passive load. The estimation algorithm was implemented using an available 60-ppr encoder mounted between the motors that has a resolution close to 48 ppr, which is frequent in automotive applications (see, e.g. [94, pp. 90-93] and [103]). The 1024-ppr encoder was used as a high-resolution reference sensor. For simplicity, the TSA was implemented considering only the rising edge of one output channel. The use of quadrature mode is nevertheless straightforward.

The performance of the estimation algorithm is illustrated in Fig. 6.4 for a time-varying velocity reference, and in Fig. 6.5 for a constant reference. The parameters and initial conditions of the estimation algorithm were set as $\kappa = 1$, $\beta = 0.1$, $\widehat{\vartheta}_0 = 0$, and Γ_0 as a matrix of the form $\Gamma_0 = \mathrm{diag}[\gamma_1, \gamma_1, \gamma_2, \gamma_2, \ldots]$ with $\gamma_1 > \gamma_2 > \ldots > \gamma_M > 0$. In all cases a comparison with respect to the results obtained using a notch filter, as proposed in [88] and [40], is shown. The damping ratio of the filter, $\xi \in (0, 1)$, was chosen as $\xi = 0.5$ in order to have a good compromise between the selectiveness of the filter and its response time. The signals labeled as 'measured' correspond to those obtained directly from the TSA.

[1]Insulated-gate bipolar transistor

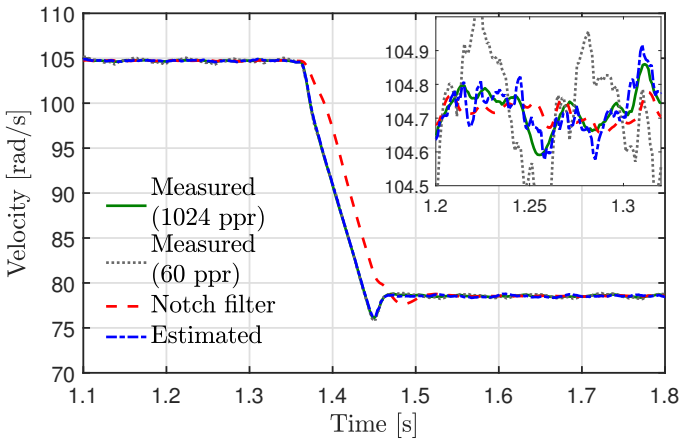

(a) Velocity

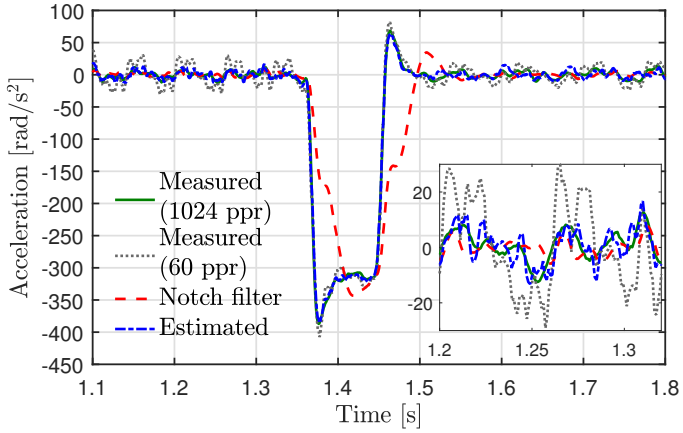

(b) Acceleration

Figure 6.4: Measured vs filtered and estimated signals for a time-varying velocity reference using $n = 15$ and $M = 5$.

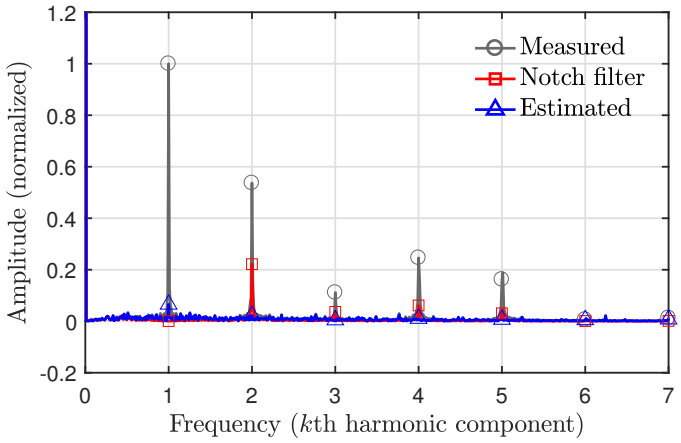

(a) Velocity

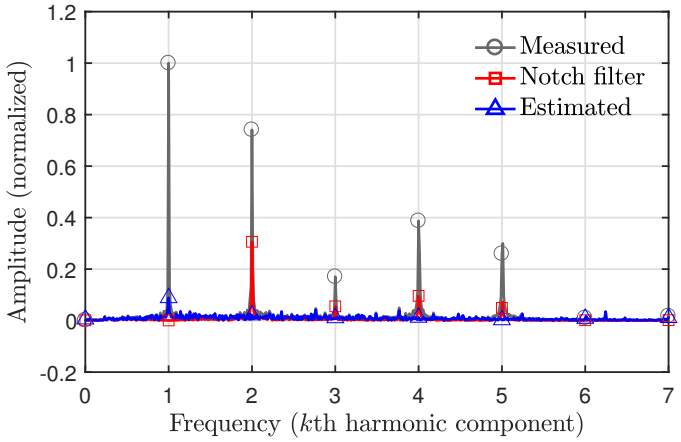

(b) Acceleration

Figure 6.5: Fourier transform of the measured, filtered, and estimated signals for a constant velocity reference using $n = 15$ and $M = 5$. The depicted amplitude is normalized to the magnitude of the first harmonic of the measured signals.

Signal	Root-mean-square error	
	Velocity [rad/s]	Acceleration [rad/s^2]
Time-varying reference		
Measured (60ppr)	0.1430	12.8528
Notch filter	5.2597	33.5899
Estimated	0.0783	5.9237
Constant reference		
Measured (60ppr)	0.3007	30.0886
Notch filter	3.0730	7.9528
Estimated	0.0716	7.9405

Table 6.1: Root-mean-square error of the measured, filtered, and estimated signals relative to the 1024-ppr encoder.

The depicted results show that, once the estimated parameters have converged to appropriate values, the estimated signals contain significantly smaller oscillations than the measurements. This can be more easily noticed during the intervals in which the velocity or the acceleration are constant. During these intervals, the level of attenuation of the periodic perturbations of the estimation algorithm is similar to that of the notch filter. The usefulness of the estimation algorithm over a notch filter is, however, more evident during the intervals in which the velocity or the acceleration are changing. Even though both the notch filter and the estimation algorithm show a good performance in terms of reducing the amplitude of the oscillations, the filter clearly introduces a significant delay, whereas the estimation scheme follows the reference with no noticeable delay. The root-mean-square error (computed with respect to measurements of the 1024-ppr encoder) is given in Table 6.1. In all cases, the proposed scheme performs better than both the TSA and the notch filter: it makes it possible to obtain better estimates of the velocity and of the acceleration without using a large number of events nor introducing a long delay. To further illustrate these advantages, in the next section we use the estimation algorithm in a concrete case-study of control systems technology, namely, the antilock braking system (ABS).

6.4 Simulation results: application to ABS control

A five-phase hybrid ABS control algorithm, based on the one presented in [89], is described in Fig. 6.6. The objective of the algorithm is to keep the wheel slip x_1 (recall the quarter-car model of Section 2.3) in a small neighbourhood around its unknown optimal value x_1^*, in order to minimize the braking distance while maintaining a good steerability of the vehicle. According to the active phase,

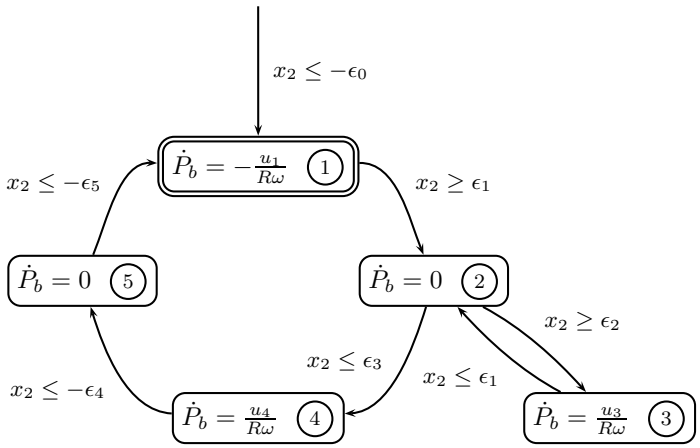

Figure 6.6: Five-phase hybrid ABS control algorithm based on that of [89].

the brake pressure is either kept constant (phases 2 and 5), or rapidly increased (phases 3 and 4) or decreased (phase 1). The changes in brake pressure are determined as a function of the wheel angular velocity ω and some parameters $u_i > 0$ that depend on the maximum pressure variations allowed by the brake actuator. The switch from one phase to another is triggered when the wheel acceleration offset x_2 crosses some predefined thresholds $\epsilon_i > 0$. Since x_2 depends on the value of the wheel acceleration α, any perturbation in the measurement of α can cause the trigger to occur at inappropriate moments.

The performance of the control algorithm is illustrated in Figs. 6.7, 6.8, and 6.9, where the phase-plane behavior of the wheel dynamics during a braking maneuver of a vehicle running on dry concrete with an initial speed of 130 km/h are shown. The TSA was implemented using $m = 2$, $n = 12$ and $M = 6$, considering an encoder with parameters $N = 60$ and $M_r = 1$. The ideal limit cycle, obtained when the real values of ω and α are used in the control algorithm, is shown in all cases using green circles. The deceleration thresholds $\epsilon_0 = 50$, $\epsilon_1 = 30$, $\epsilon_2 = 40$, $\epsilon_3 = 20$, $\epsilon_4 = 20$, and $\epsilon_5 = 30$ m/s^2, are represented by the horizontal gray lines. The optimal point $(x_1^*, 0)$ is indicated with a cross. Any variation in x_1 decreases the average braking force, while variations in x_2 demand a stronger effort from the brake actuator. Therefore, the amplitude of the cycle is a measure of the braking performance: the smaller the cycle, the shorter the vehicle's braking distance.

Fig. 6.7 shows the behavior obtained when the measurements affected by encoder imperfections are used. Due to the perturbations in the measured signals, the algorithm fails to cycle and remains blocked in an arbitrary phase (in this particular simulation, the wheel is trapped at the point $(-7, 0)$). To cope with this, one may increase the values of ϵ_i (as suggested in [31]) so that only the most significant variations in x_2 are detected, but this implies increasing the amplitude of the limit cycle as well. When a notch filter (see [88] and [40]) is used to remove the perturbations in the measured signals (Fig. 6.8), the control

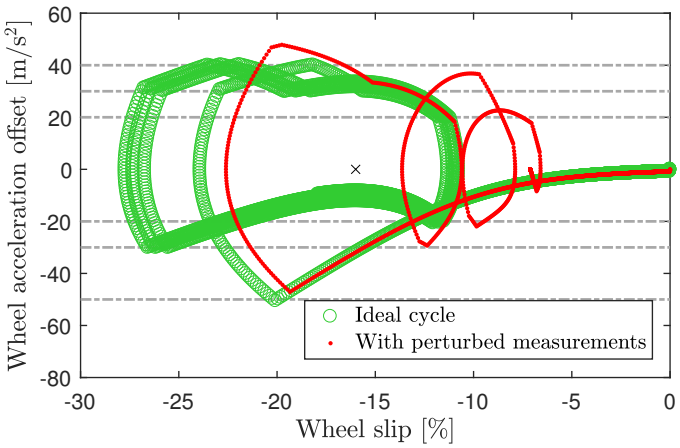

Figure 6.7: Ideal cycle vs behavior obtained with the measurements affected by encoder imperfections.

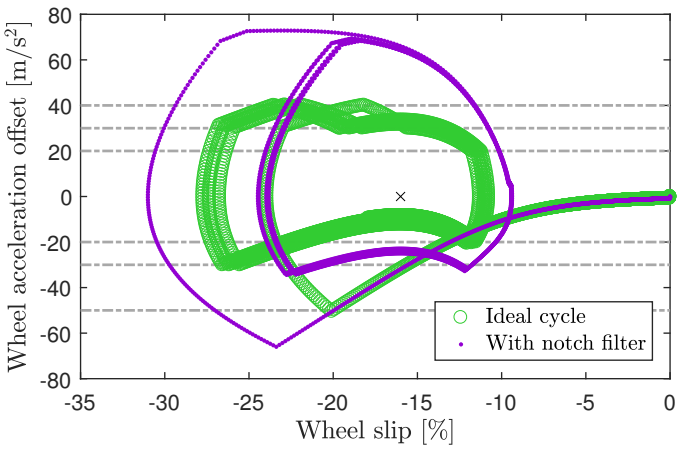

Figure 6.8: Ideal cycle vs behavior obtained using a notch filter.

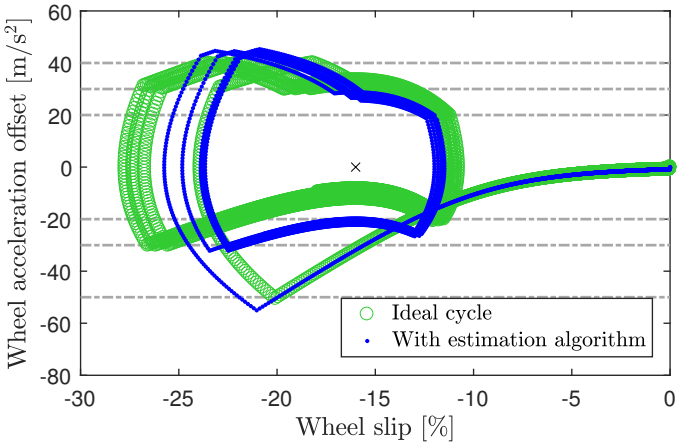

Figure 6.9: Ideal cycle vs behavior obtained using the estimation algorithm.

algorithm is able to cycle around the desired point, but the performance is far from optimal. The delay introduced by the notch filter causes the algorithm to switch from one phase to another at inappropriate moments and the acceleration to go far outside the predefined thresholds. Finally, when the estimation algorithm is used to compensate for the encoder imperfections (Fig. 6.9), the control algorithm is able to cycle around the desired point. Although the estimation is not perfect and the acceleration violates the predefined thresholds, the excursion is smaller (around 35 m/s^2) than with the notch filter. Thus, the use of the estimation algorithm renders the performance of the control algorithm much closer to optimal.

6.5 Conclusion

In this chapter we presented a three-stage algorithm to estimate angular velocity and acceleration from incremental encoder measurements and reduce the effects of the encoder imperfections. The performance of the algorithm has been evaluated in open-loop via experimental tests with satisfactory results, and in closed-loop via numerical simulations. Although the estimation algorithm is presented in this work in the context of the ABS, the domain of application of our contribution is by no means restricted to the automotive field.

7 Conclusions and recommendations

This thesis has addressed the problem of the estimation of the XBS, its use in the design of a control algorithm for the ABS, and the estimation of the angular velocity and acceleration of the wheel, both of which are essential signals for the operation of the ABS. Some concluding remarks and recommendations for future research on each of these topics are given below.

In Chapter 3, a switched adaptive observer for the estimation of the XBS is presented. The observer is designed based on a quarter-car model which considers a vehicle braking on a straight line, and tested via numerical simulations and using experimental data under such scenario. Although the simulations are performed considering phenomena such as dynamic load transfer and tyre relaxation length with satisfactory results, further tests should be conducted considering a more realistic setting that includes, for example, the lateral dynamics of the tyre-road friction forces. Furthermore, the observer is designed considering the system's parameters $(R^2/J)F_z$ and $(R/J)\gamma_b$ to be known and constant. While variations of the vertical load F_z and its estimation from the measurements of the vehicle acceleration are considered in the simulations presented in this thesis, variations and uncertainties in the other parameters are not. Nevertheless, it is expected (by the author) that the estimation of the XBS will not be significantly affected when these elements are taken into account, since several approaches for the estimation of the effective rolling radius R and the brake efficiency γ_b are available in the literature —see, e.g. [14, 28, 72] for the former and [64, 43, 77, 36] for the latter.

In Chapter 4, two XBS-based control algorithms for the ABS are presented: a continuous one that does not achieve the control objective of the ABS when implemented in closed loop with the XBS observer, and a hybrid one that does. Although our primary objective was to develop an XBS regulation controller, this challenging task could not be accomplished because of the conditions on the system's measured output required for the convergence of the observer. While it is well known that that the separation principle does not hold in general for nonlinear systems, concrete examples of this fact do not seem to be so frequent in the literature. Hence, the "negative" results obtained with the continuous algorithm are included in the thesis, as we believe that they represent an interesting (albeit purely illustrative) contribution to this topic.

In order for the system's trajectories to satisfy the (PE, zero-crossing transversality, and dwell-time) conditions required for the convergence of the observer, the second algorithm is designed following the paradigm of logic-based switching controllers. Our aim at this stage is to design an algorithm that, unlike previous approaches, does not require additional torque/force sensors. The resulting two-phase hybrid algorithm is simple, easy to implement, and has shown to be able to produce shorter braking distances when compared to a deceleration-based algorithm. We emphasize, however, that our work in this topic is part of an ongoing project. Hence, although we believe that the control of ABS based on the estimation of the XBS is a promising approach, the results presented in Chapter 4 should be seen as merely a first step towards that goal.

Among the following steps are included the stability analysis of the closed-loop system (that is, including the dynamics of the observer), as well as the evaluation of the controller in the presence of unmodelled dynamics and changes in the road conditions. Moreover, future work should study whether the two-phase hybrid algorithm meets the requirements for practical implementation, especially regarding its robustness to actuator delay, and modify it accordingly if necessary as was done in [31]. Another interesting topic to be studied concerns the performance of the controller when the tyre-road friction curve does not have a well-defined maximum, which is typically the case when braking on ice or gravel. Previous hybrid algorithms [89, 18] have reported to present difficulties in that situation. However, because the switching thresholds of the two-phase hybrid algorithm depend directly on the slope of the friction curve (the XBS), it is expected that our algorithm will be able to deal more easily with that situation.

In Chapter 6, a three-stage algorithm to estimate the angular velocity and acceleration of the wheel and remove the periodical perturbations caused by encoder imperfections is presented. The key point of our approach is to take into account the effects of the time-stamping algorithm by considering a model for the acceleration perturbation that differs from the derivative of the velocity perturbation. The algorithm does not require the availability of error look-up tables, and it has a good performance in terms of reducing the effects of the imperfections without introducing a long delay. The experimental tests show that the algorithm is quite effective in applications which employ low-resolution encoders, such as the ABS. However, the usefulness of the algorithm in other areas, and especially in those which employ high-resolution encoders, still needs to be explored. It is expected that the algorithm will be useful, for example, for minimizing torque ripple in electrical motors [29]. Finally, it is to be noted that the utility of the algorithm in a closed-loop control scenario is illustrated only via numerical simulations. Unfortunately, no (closed-loop) experimental tests could be performed within the time span of this thesis. Such tests are expected to take place in oncoming projects.

APPENDICES

A POINCARÉ MAP

In this appendix we present a brief introduction to the Poincaré map adapted from [110, § 8.7]. For a complete discussion on this topic, the reader is referred to [91, § 3.4] and [100, § 7.3], as well as [124, Ch. 4] for the case of Poincaré maps for hybrid systems.

Consider a system $\dot{x} = f(x)$ with $x \in \mathbb{R}^n$, $x(0) = x_0$ and f smooth. Let S be a transverse section, that is, a surface of dimension $n-1$ transverse to the associated flow (all trajectories starting on S flow through it, not parallel to it). A Poincaré map is a mapping $P : S \to S$ obtained by following trajectories of x from one intersection with S to the next. If $x_k \in S$ denotes the kth intersection, then the Poincaré map is defined by

$$x_{k+1} = P(x_k).$$

Suppose x° is a fixed point of P, that is, $P(x^\circ) = x^\circ$. Then, a trajectory starting at x° returns to x° after some time T and is therefore a closed orbit γ for the original system —see Fig. A.1. Moreover, by studying the behaviour of P near x°, one can determine the stability of γ. In particular, if

$$\left|P'(x^\circ)\right| < 1,$$

then γ is asymptotically stable [39, § 10.3] —see also [26, Ch. 5].

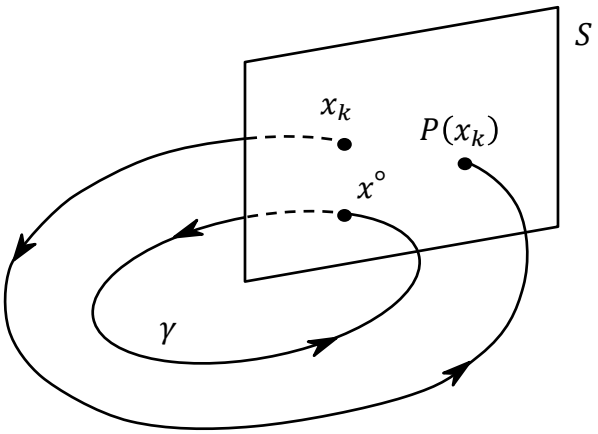

Figure A.1: Geometric interpretation of a Poincaré map $P : S \to S$.

B LAMBERT W FUNCTION

In this appendix we present a brief introduction to the Lambert W function adapted from [17] and we expand on the solution of (4.7) and (4.10).

Consider the equation

$$\xi \exp(\xi) = \Delta, \tag{B.1}$$

with $\xi, \Delta \in \mathbb{C}$. The solution to (B.1) is given by

$$\xi = W(\Delta), \tag{B.2}$$

where W, known as the Lambert W function (see [16]), is defined to be the multi-valued inverse of the function

$$f(\xi) = \xi \exp(\xi).$$

Because f is not injective, (B.1) has a countably infinite number of solutions, which are denoted by $W_k(\Delta)$ for $k \in \mathbb{Z}$. That is, each integer k specifies a branch of the Lambert W function. By convention, only the branches $k = 0$ (called the principal branch) and $k = -1$ are those that are real-valued for any Δ.

Moreover, if $\Delta \in \mathbb{R}$, then

- for $\Delta \in [-1/e, 0]$, (B.1) has two real solutions $W_0(\Delta)$ and $W_{-1}(\Delta)$.
- for $\Delta \in [0, \infty)$, (B.1) has one real solution $W_0(\Delta)$.
- for $\Delta \in (-\infty, -1/e)$, (B.1) no real solution.

—see Fig. B.1.

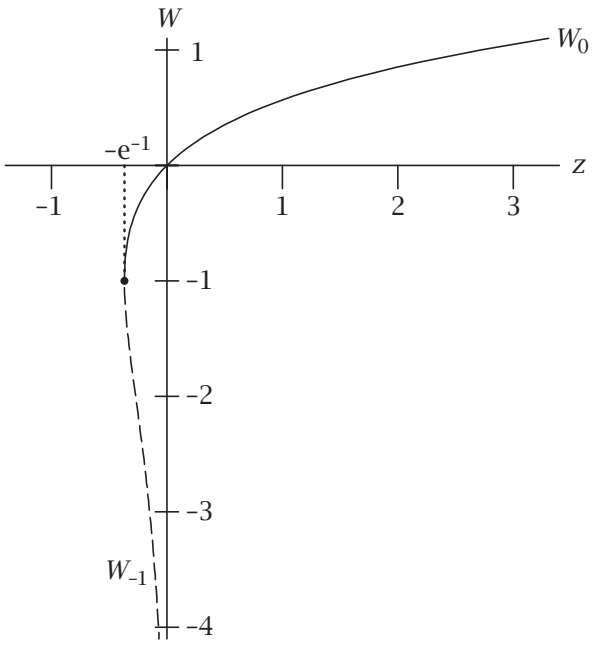

Figure B.1: Real branches of the Lambert W function. The solid line is the principal branch W_0; the dashed line is W_{-1}, which is the only other branch that takes real values. Source of illustration: [38, p. 152].

SOLUTION OF EQUATIONS OF THE FORM $ax + b\ln(x) + c = 0$

Now, consider the equation

$$ax + b\ln(x) + c = 0, \tag{B.3}$$

where $a, b, c \in \mathbb{R}$ and $a, b \neq 0$. Rewriting (B.3) yields

$$\begin{aligned} & ax + b\left[\ln\left(\frac{a}{b}x\right) - \ln\left(\frac{a}{b}\right)\right] + c = 0 \\ \Rightarrow \qquad & \ln\left(\frac{a}{b}x\right) + \frac{a}{b}x = \ln\left(\frac{a}{b}\right) - \frac{c}{b} \\ \Rightarrow \qquad & \left(\frac{a}{b}x\right)\exp\left(\frac{a}{b}x\right) = \frac{a}{b}\exp\left(-\frac{c}{b}\right). \end{aligned}$$

Note that this expression is of the form (B.1). Hence, taking $\xi = (a/b)x$ and $\Delta = (a/b)\exp(-c/b)$ in (B.2) yields

$$\begin{aligned} & \frac{a}{b}x = W\left(\frac{a}{b}\exp\left(-\frac{c}{b}\right)\right) \\ \Rightarrow \qquad & x = \frac{b}{a}W\left(\frac{a}{b}\exp\left(-\frac{c}{b}\right)\right). \end{aligned} \tag{B.4}$$

Finally, note that (4.7), given by

$$\left(1 - \zeta_1'\right) - \ln\left(1 - \zeta_1'\right) + \delta_1 = 0,$$

is of the form (B.3) with $x = 1 - \zeta_1'$, $a = 1$, $b = -1$, and $c = \delta_1$. Thus, from (B.4), it follows that

$$1 - \zeta_1' = -W(-\exp(\delta_1)).$$

Moreover, note that (4.10), given by

$$\left(1 + \zeta_1''\right) - \ln\left(1 + \zeta_1''\right) + \delta_2 = 0,$$

is also of the form (B.3) with $x = 1 + \zeta_1''$, $a = 1$, $b = -1$, and $c = \delta_2$. Thus, from (B.4), it follows that

$$1 + \zeta_1'' = -W(-\exp(\delta_2)).$$

In this work only the solutions given by the branch W_0 are used.

C SCALING OF ENCODER EVENTS IN THE TIME-STAMPING ALGORITHM

During the execution of the TSA, numerical problems in the polynomial fit and/or conditioning problems in the matrix A may arise because the time instants and the time span of the stored encoder events can be very small (even in the order of the sampling period of the high-resolution clock). To prevent such problems, the time instants of the events are reset to zero and normalized in every sampling time of the controller.

Let t_{reg} denote the register (or array) that contains the time instant information of the last n events. If the absolute value of the elements in the register is big, numerical problems may arise because of the higher-order terms in A. Moreover, if the difference between the elements in the register is very small, then A can become ill-conditioned. To prevent these issues, the elements in t_{reg} are referenced with respect to the oldest event in the register, i.e. shifted by $-t_{k-n+1}$, and scaled with respect to the time span $\Delta = t_k - t_{k-n+1}$ between the first and the last elements in the register.

For example, consider a second order fit with five events, i.e. $m = 2$ and $n = 5$, and let

$$t_{\text{reg}} = \begin{bmatrix} 22 & 23 & 24 & 25 & 26 \end{bmatrix} \times 10^{-5}.$$

The oldest event in the register is $t_{k-n+1} = 22 \times 10^{-5}$ and the time span is $\Delta = 4 \times 10^{-5}$. Hence, the elements in t_{reg} are shifted and scaled as

$$t'_{\text{reg}} = \frac{1}{\Delta}(t_{\text{reg}} - t_{k-n+1}) = \begin{bmatrix} 0 & 0.25 & 0.5 & 0.75 & 1 \end{bmatrix}.$$

The condition number of the matrix A' built with the shifted-and-scaled time instants in t'_{reg} is $\text{cond}(A') = 16.66$, whereas the condition number of the matrix A built with the true time instants is $\text{cond}(A) = 5.97 \times 10^9$. The time scaling improves the numerical properties of the matrix rendering it well-conditioned, and thus improves the accuracy of the least squares solution to the regression problem.

After replacing A with A' in (5.3) and solving for x to estimate the polynomial coefficients $p_0, \ldots, p_m$, the time scaling is accounted for in the polynomial extrapolation by redefining (5.1), (5.4), and (5.5). Thus the position, velocity, and acceleration at time t are estimated as

$$\theta(t) = \sum_{i=0}^{m} p_i \left(\frac{1}{\Delta}(t - t_{k-n+1}) \right)^i$$

$$\omega(t) = \sum_{i=1}^{m} i\, p_i \left(\frac{1}{\Delta}(t - t_{k-n+1}) \right)^{i-1} \frac{1}{\Delta}$$

and

$$\alpha(t) = \sum_{i=2}^{m} (i-1)\, i\, p_i \left(\frac{1}{\Delta}(t - t_{k-n+1}) \right)^{i-2} \frac{1}{\Delta^2}.$$

REFERENCES

[1] AHN, C., PENG, H., AND TSENG, H. E. Robust estimation of road frictional coefficient. *IEEE Transactions on Control Systems Technology*, 21(1):1–13, 2013.

[2] ALVAREZ, L., AND YI, J. Adaptive emergency braking control in automated highway systems. In *Proceedings of the 38th IEEE Conference on Decision and Control* (1999), vol. 4, pp. 3740–3745.

[3] ALVAREZ, L., YI, J., HOROWITZ, R., AND OLMOS, L. Dynamic friction model-based tire-road friction estimation and emergency braking control. *Journal of Dynamic Systems, Measurement, and Control*, 127(1):22–32, 2005.

[4] APEC BRAKING. ABS sensors. Retrieved from https://www.apecbraking.co.uk/Resources/TechniciansGuides/ABS-Sensors.aspx, n.d. Accessed: March 05, 2019.

[5] APOSTOL, T. M. *Calculus*, second ed., vol. I One-variable calculus, with an introduction to linear algebra. John Wiley & Sons, 1967.

[6] BÄHR, J., AND ERKER, P. *Bosch: History of a Global Enterprise*. C.H. Beck, Munich, Germany, 2015.

[7] BASCETTA, L., MAGNANI, G., AND ROCCO, P. Velocity estimation: Assessing the performance of non-model-based techniques. *IEEE Transactions on Control Systems Technology*, 17(2):424–433, 2009.

[8] BESANÇON, G. A viewpoint on observability and observer design for nonlinear systems. In *New Directions in Nonlinear Observer Design*, H. Nijmeijer and T. Fossen, Eds., vol. 244 of *Lecture Notes in Control and Information Sciences*. Springer London, 1999, pp. 3–22.

[9] BLIMAN, P. A., AND SORINE, M. Easy-to-use realistic dry friction models for automatic control. In *Proceedings of the 3rd European Control Conference* (1995), pp. 3788–3794.

[10] BLUNDELL, M., AND HARTY, D. *Multibody Systems Approach to Vehicle Dynamics*, second ed. Butterworth-Heinemann, 2015.

[11] BROWN, R. H., AND SCHNEIDER, S. C. Velocity observations from discrete position encoders. In *Proc. SPIE 0858 Signal Acquisition and Processing* (1987), pp. 1111–1118.

[12] BURCKHARDT, M. *Fahrwerktechnik: Radschlupf-Regelsysteme*. Vogel-Verlag, Würzburg, Germany, 1993.

[13] CANUDAS DE WIT, C., TSIOTRAS, P., VELENIS, E., BASSET, M., AND GISSINGER, G. Dynamic friction models for road/tire longitudinal interaction. *Vehicle System Dynamics*, 39(3):189–226, 2003.

[14] CARLSON, C. R., AND GERDES, J. C. Consistent nonlinear estimation of longitudinal tire stiffness and effective radius. *IEEE Transactions on Control Systems Technology*, 13(6):1010–1020, 2005.

[15] CHOI, S. B. Antilock brake system with a continuous wheel slip control to maximize the braking performance and the ride quality. *IEEE Transactions on Control Systems Technology*, 16(5):996–1003, 2008.

[16] CORLESS, R. M., GONNET, G. H., HARE, D. E. G., JEFFREY, D. J., AND KNUTH, D. E. On the Lambert W function. *Advances in Computational Mathematics*, 5(1):329–359, 1996.

[17] CORLESS, R. M., AND JEFFREY, D. J. The Lambert W function. In *The Princeton Companion to Applied Mathematics*, N. J. Higham, Ed. Princeton University Press, 2015, pp. 151–155.

[18] CORNO, M., GERARD, M., VERHAEGEN, M., AND HOLWEG, E. Hybrid ABS control using force measurement. *IEEE Transactions on Control Systems Technology*, 20(5):1223–1235, 2012.

[19] CORNO, M., PANZANI, G., AND SAVARESI, S. M. Traction-control-oriented state estimation for motorcycles. *IEEE Transactions on Control Systems Technology*, 21(6):2400–2407, 2013.

[20] CORNO, M., ROSELLI, F., ONESTO, L., MOLINARO, F., GRAVES, E., DOUBEK, A., AND SAVARESI, S. M. Experimental validation of an antilock braking system for snowmobiles with lateral stability considerations. *IEEE Transactions on Control Systems Technology*, 1–8, 2018.

[21] CORNO, M., AND SAVARESI, S. M. Experimental identification of engine-to-slip dynamics for traction control applications in a sport motorbike. *European Journal of Control*, 16(1):88–108, 2010.

[22] DAHL, P. R. Solid friction damping of mechanical vibrations. *AIAA Journal*, 14(12):1675–1682, 1976.

[23] DAIMLER AG. Mercedes-Benz and the invention of the anti-lock braking system: ABS, ready for production in 1978. Retrieved from https://media.daimler.com/marsMediaSite/ko/en/9913502, 2008. Accessed: April 01, 2019.

[24] DE SILVA, C. W. *Sensors and actuators: Engineering system instrumentation*, second ed. CRC Press, 2015.

[25] DEUR, J., ASGARI, J., AND HROVAT, D. A 3D brush-type dynamic tire friction model. *Vehicle System Dynamics*, 42(3):133–173, 2004.

[26] DEVANEY, R. L. *A First Course In Chaotic Dynamical Systems: Theory And Experiment*. Westview Press, 1992.

[27] DRAKUNOV, S., ÖZGÜNER, Ü., DIX, P., AND ASHRAFI, B. ABS control using optimum search via sliding modes. *IEEE Transactions on Control Systems Technology*, 3(1):79–85, 1995.

[28] EL TANNOURY, C., MOUSSAOUI, S., PLESTAN, F., ROMANI, N., AND PITA-GIL, G. Synthesis and application of nonlinear observers for the estimation of tire effective radius and rolling resistance of an automotive vehicle. *IEEE Transactions on Control Systems Technology*, 21(6):2408–2416, 2013.

[29] ESPÍNDOLA-LÓPEZ, E., GÓMEZ-ESPINOSA, A., CARRILLO-SERRANO, R. V., AND JÁUREGUI-CORREA, J. C. Fourier series learning control for torque ripple minimization in permanent magnet synchronous motors. *Applied Sciences*, 6(9), 2016.

[30] GENTA, G. *Motor vehicle dynamics: modeling and simulation*, vol. 43 of *Advances in Mathematics for Applied Sciences*. World Scientific, 2006.

[31] GERARD, M., PASILLAS-LÉPINE, W., DE VRIES, E., AND VERHAEGEN, M. Improvements to a five-phase ABS algorithm for experimental validation. *Vehicle System Dynamics*, 50(10):1585–1611, 2012.

[32] GUAY, M. Observer linearization by output-dependent time-scale transformations. *IEEE Transactions on Automatic Control*, 47(10):1730–1735, 2002.

[33] GUSTAFSSON, F. Slip-based tire-road friction estimation. *Automatica*, 33(6):1087–1099, 1997.

[34] GUSTAFSSON, F. Automotive safety systems. *IEEE Signal Processing Magazine*, 26(4):32–47, 2009.

[35] GUSTAFSSON, F. Rotational speed sensors: limitations, pre-processing and automotive applications. *IEEE Instrumentation & Measurement Magazine*, 13(2):16–23, 2010.

[36] HAN, K., CHOI, S. B., LEE, J., HYUN, D., AND LEE, J. Accurate brake torque estimation with adaptive uncertainty compensation using a brake force distribution characteristic. *IEEE Transactions on Vehicular Technology*, 66(12):10830–10840, 2017.

[37] HESPANHA, J. P. Uniform stability of switched linear systems: extensions of LaSalle's invariance principle. *IEEE Transactions on Automatic Control*, 49(4):470–482, 2004.

[38] HIGHAM, N. J., Ed. *The Princeton Companion to Applied Mathematics*. Princeton University Press, 2015.

[39] HIRSCH, M. W., SMALE, S., AND DEVANEY, R. L. *Differential Equations, Dynamical Systems, and an Introduction to Chaos*, second ed. Academic Press, 2004.

[40] HOÀNG, T. B., PASILLAS-LÉPINE, W., AND DE BERNARDINIS, A. Reducing the impact of wheel-frequency oscillations in continuous and hybrid abs strategies. In *Proceedings of the 11th International Symposium on Advanced Vehicle Control (AVEC'12)* (2012).

[41] HOÀNG, T. B., PASILLAS-LÉPINE, W., DE BERNARDINIS, A., AND NETTO, M. Extended braking stiffness estimation based on a switched observer, with an application to wheel-acceleration control. *IEEE Transactions on Control Systems Technology*, 22(6):2384–2392, 2014.

[42] HOÀNG, T. B., PASILLAS-LÉPINE, W., AND RESPONDEK, W. A switching observer for systems with linearizable error dynamics via singular time-scaling. In *Proceedings of the 21st International Symposium on Mathematical Theory of Networks and Systems* (2014), pp. 1101–1108.

[43] HONG, D., HWANG, I., YOON, P., AND HUH, K. Development of a vehicle stability control system using brake-by-wire actuators. *Journal of Dynamic Systems, Measurement, and Control*, 130(1):011008, 2007.

[44] HSU, L., ORTEGA, R., AND DAMM, G. A globally convergent frequency estimator. *IEEE Transactions on Automatic Control*, 44(4):698–713, 1999.

[45] IOANNOU, P., AND SUN, J. *Robust Adaptive Control*. Dover Books on Electrical Engineering. Dover Publications, 2012.

[46] JIANG, F., AND GAO, Z. An application of nonlinear PID control to a class of truck ABS problems. In *Proceedings of the 40th IEEE Conference on Decision and Control* (2001), vol. 1, pp. 516–521.

[47] JOHANSEN, T. A., PETERSEN, I., KALKKUHL, J., AND LUDEMANN, J. Gain-scheduled wheel slip control in automotive brake systems. *IEEE Transactions on Control Systems Technology*, 11(6):799–811, 2003.

[48] JOHNSON, A. *Hitting the Brakes: Engineering Design and the Production of Knowledge*. Duke University Press, 2009.

[49] JOHNSON, A. The culture of ABS. *Mechanical Engineering*, 132(9):26–31, 2010.

[50] KAVANAGH, R. C. Improved digital tachometer with reduced sensitivity to sensor nonideality. *IEEE Transactions on Industrial Electronics*, 47(4):890–897, 2000.

[51] KAVANAGH, R. C. Shaft encoder characterization via theoretical model of differentiator with both differential and integral nonlinearities. *IEEE Transactions on Instrumentation and Measurement*, 49(4):795–801, 2000.

[52] KAVANAGH, R. C. Performance analysis and compensation of M/T-type digital tachometers. *IEEE Transactions on Instrumentation and Measurement*, 50(4):965–970, 2001.

[53] KAVANAGH, R. C. Shaft encoder characterisation through analysis of the mean-squared errors in nonideal quantised systems. *IEE Proceedings - Science, Measurement and Technology*, 149(2):99–104, 2002.

[54] KHALIL, H. K. *Nonlinear Systems*, second ed. Prentice Hall, 1996.

[55] KIENCKE, U. Realtime estimation of adhesion characteristic between tyres and road. *IFAC Proceedings Volumes*, 26(2, Part 3):15–18, 1993. 12th IFAC World Congress.

[56] KIENCKE, U., AND DAISS, S. Estimation of tyre friction for enhanced ABS systems. In *Proceedings of the International Symposium on Advanced Vehicle Control (AVEC'94)* (1994), pp. 515–520.

[57] KIENCKE, U., AND NIELSEN, L. *Automotive control systems: For engine, driveline, and vehicle*, second ed. Springer-Verlag Berlin Heidelberg, 2005.

[58] KNORR-BREMSE AG. Looking back on 110 years of expertise: Milestones of the Rail Vehicle Systems and Commercial Vehicle Systems divisions. Retrieved from https://www.knorr-bremse.com/en/company/history/, n.d. Accessed: April 03, 2019.

[59] KOENIGSEGG. Koenigsegg Agera RS achieves multiple production car world speed records. Retrieved from https://www.koenigsegg.com/koenigsegg-agera-rs-achieves-multiple-production-car-world-speed-records/, Nov. 2017. Accessed: March 25, 2019.

[60] KÖPPEN, T., KÜPPER, T., AND MAKARENKOV, O. Existence and stability of limit cycles in control of anti-lock braking systems with two boundaries via perturbation theory. *International Journal of Control*, 90(5):974–989, 2017.

[61] KREIT, D. Optical encoders – are they as accurate as you think? Zettlex UK Ltd (Technical white paper), 2014.

[62] KUO, C.-Y., AND YEH, E. C. A four-phase control scheme of an anti-skid brake system for all road conditions. *Proceedings of the Institution of Mechanical Engineers, Part D: Journal of Automobile Engineering*, 206(4):275–283, 1992.

[63] LAYNE, J. R., PASSINO, K. M., AND YURKOVICH, S. Fuzzy learning control for antiskid braking systems. *IEEE Transactions on Control Systems Technology*, 1(2):122–129, 1993.

[64] LEE, C., HEDRICK, K., AND YI, K. Real-time slip-based estimation of maximum tire-road friction coefficient. *IEEE/ASME Transactions on Mechatronics*, 9(2):454–458, 2004.

[65] LEIBER, H., AND CZINCZEL, A. Antiskid system for passenger cars with a digital electronic control unit, 1979. SAE Technical Paper 790458.

[66] LI, L., WANG, F.-Y., AND ZHOU, Q. Integrated longitudinal and lateral tire/road friction modeling and monitoring for vehicle motion control. *IEEE Transactions on Intelligent Transportation Systems*, 7(1):1–19, 2006.

[67] LI, X., ZHANG, Q., AND SU, H. An adaptive observer for joint estimation of states and parameters in both state and output equations. *International Journal of Adaptive Control and Signal Processing*, 25(9):831–842, 2011.

[68] LIBERZON, D. *Switching in Systems and Control*. Systems & Control: Foundations & Applications. Birkhäuser Basel, 2003.

[69] LIN, C.-M., AND HSU, C.-F. Self-learning fuzzy sliding-mode control for antilock braking systems. *IEEE Transactions on Control Systems Technology*, 11(2):273–278, 2003.

[70] LORÍA, A., AND PANTELEY, E. Uniform exponential stability of linear time-varying systems: revisited. *Systems & Control Letters*, 47(1):13–24, 2002.

[71] LORÍA, A., AND PANTELEY, E. Cascaded nonlinear time-varying systems: Analysis and design. In *Advanced Topics in Control Systems Theory: Lecture Notes from FAP 2004*, F. Lamnabhi-Lagarrigue, A. Loría, and E. Panteley, Eds., vol. 311 of *Lecture Notes in Control and Information Sciences*. Springer London, 2005, pp. 23–64.

[72] LUNDQUIST, C., KARLSSON, R., ÖZKAN, E., AND GUSTAFSSON, F. Tire radii estimation using a marginalized particle filter. *IEEE Transactions on Intelligent Transportation Systems*, 15(2):663–672, 2014.

[73] MARINO, R., AND TOMEI, P. *Nonlinear Control Design: Geometric, Adaptive, and Robust*. Prentice Hall, 1995.

[74] MASTINU, G., AND PLOECHL, M., Eds. *Road and off-road vehicle system dynamics handbook*. CRC Press, 2014.

[75] MERRY, R., VAN DE MOLENGRAFT, M., AND STEINBUCH, M. Velocity and acceleration estimation for optical incremental encoders. *Mechatronics*, 20(1):20–26, 2010. Special Issue on "Servo Control for Data Storage and Precision Systems", from 17th IFAC World Congress 2008.

[76] MERRY, R., VAN DE MOLENGRAFT, M., AND STEINBUCH, M. Optimal higher-order encoder time-stamping. *Mechatronics*, 23(5):481–490, 2013.

[77] MILLER, J. I., AND CEBON, D. A high performance pneumatic braking system for heavy vehicles. *Vehicle System Dynamics*, 48(S1):373–392, 2010.

[78] MOONEY, G. Safe landing. *ANSYS Advantage*, VII(1):10–13, 2013.

[79] MORRIS, B., AND GRIZZLE, J. W. Hybrid invariant manifolds in systems with impulse effects with application to periodic locomotion in bipedal robots. *IEEE Transactions on Automatic Control*, 54(8):1751–1764, 2009.

[80] MÜLLER, S., UCHANSKI, M., AND HEDRICK, K. Estimation of the maximum tire-road friction coefficient. *Journal of Dynamic Systems, Measurement, and Control*, 125(4):607–617, 2003.

[81] NARENDRA, K. S., AND ANNASWAMY, A. M. *Stable Adaptive Systems*. Dover Publications, 2005.

[82] NEMYTSKII, V. V., AND STEPANOV, V. V. *Qualitative Theory of Differential Equations*. Princeton University Press, 1960.

[83] ONO, E., ASANO, K., SUGAI, M., ITO, S., YAMAMOTO, M., SAWADA, M., AND YASUI, Y. Estimation of automotive tire force characteristics using wheel velocity. *Control Engineering Practice*, 11(12):1361–1370, 2003.

[84] OUWERKERK, H., AND GUNTUR, R. R. Skid prediction. *Vehicle System Dynamics*, 1(2):67–88, 1972.

[85] PACEJKA, H. B. *Tire and Vehicle Dynamics*, third ed. Butterworth-Heinemann, 2012.

[86] PANTELEY, E., AND LORÍA, A. Growth rate conditions for uniform asymptotic stability of cascaded time-varying systems. *Automatica*, 37(3):453–460, 2001.

[87] PANTELEY, E., LORÍA, A., AND TEEL, A. Relaxed persistency of excitation for uniform asymptotic stability. *IEEE Transactions on Automatic Control*, 46(12):1874–1886, 2001.

[88] PANZANI, G., CORNO, M., AND SAVARESI, S. M. On the periodic noise affecting wheel speed measurement. *IFAC Proceedings Volumes*, 45(16):1695–1700, 2012. 16th IFAC Symposium on System Identification.

[89] PASILLAS-LÉPINE, W. Hybrid modeling and limit cycle analysis for a class of five-phase anti-lock brake algorithms. *Vehicle System Dynamics*, 44(2):173–188, 2006.

[90] PASILLAS-LÉPINE, W., LORÍA, A., AND GERARD, M. Design and experimental validation of a nonlinear wheel slip control algorithm. *Automatica*, 48(8):1852–1859, 2012.

[91] PERKO, L. *Differential Equations and Dynamical Systems*, third ed., vol. 7 of *Texts in Applied Mathematics*. Springer-Verlag New York, 2001.

[92] RAJAMANI, R., PIYABONGKARN, N., LEW, J., YI, K., AND PHANOMCHOENG, G. Tire-road friction-coefficient estimation. *IEEE Control Systems*, 30(4):54–69, 2010.

[93] RALLO, G., FORMENTIN, S., CORNO, M., AND SAVARESI, S. M. Real-time pedaling rate estimation via wheel speed filtering. *IFAC-PapersOnLine*, 50(1):6010–6015, 2017. 20th IFAC World Congress.

[94] REIF, K., Ed. *Brakes, brake control and driver assistance systems: Function, regulation and components*. Bosch Professional Automotive Information. Springer Vieweg, Wiesbaden, Germany, 2014.

[95] RESPONDEK, W., POGROMSKY, A., AND NIJMEIJER, H. Time scaling for observer design with linearizable error dynamics. *Automatica*, 40(2):277–285, 2004.

[96] REZAEIAN, A., KHAJEPOUR, A., MELEK, W., CHEN, S.-K., AND MOSHCHUK, N. Simultaneous vehicle real-time longitudinal and lateral velocity estimation. *IEEE Transactions on Vehicular Technology*, 66(3):1950–1962, 2017.

[97] RODRIGO MARCO, V., KALKKUHL, J., AND RAISCH, J. EKF for simultaneous vehicle motion estimation and IMU bias calibration with observability-based adaptation. In *2018 American Control Conference (ACC)* (2018), pp. 6309–6316.

[98] RONSSE, R., DE ROSSI, S. M. M., VITIELLO, N., LENZI, T., CARROZZA, M. C., AND IJSPEERT, A. J. Real-time estimate of velocity and acceleration of quasi-periodic signals using adaptive oscillators. *IEEE Transactions on Robotics*, 29(3):783–791, 2013.

[99] SAMPEI, M., AND FURUTA, K. On time scaling for nonlinear systems: Application to linearization. *IEEE Transactions on Automatic Control*, 31(5):459–462, 1986.

[100] SASTRY, S. *Nonlinear Systems: Analysis, Stability, and Control*, vol. 10 of *Interdisciplinary Applied Mathematics*. Springer-Verlag New York, 1999.

[101] SAVARESI, S. M., AND TANELLI, M. *Active braking control systems design for vehicles*. Advances in Industrial Control. Springer-Verlag London, 2010.

[102] SAVARESI, S. M., TANELLI, M., AND CANTONI, C. Mixed slip-deceleration control in automotive braking systems. *Journal of Dynamic Systems, Measurement, and Control*, 129(1):20–31, 2007.

[103] SAVARESI, S. M., TANELLI, M., LANGTHALER, P., AND DEL RE, L. New regressors for the direct identification of tire deformation in road vehicles via "in-tire" accelerometers. *IEEE Transactions on Control Systems Technology*, 16(4):769–780, 2008.

[104] SAVITZKY, A., AND GOLAY, M. J. E. Smoothing and differentiation of data by simplified least squares procedures. *Analytical Chemistry*, 36(8):1627–1639, 1964.

[105] SCHAFER, R. W. On the frequency-domain properties of Savitzky-Golay filters. In *2011 Digital Signal Processing and Signal Processing Education Meeting (DSP/SPE)* (2011), pp. 54–59.

[106] SCHAFER, R. W. What *Is* a Savitzky-Golay filter? [lecture notes]. *IEEE Signal Processing Magazine*, 28(4):111–117, 2011.

[107] SIMON, B. Braking without locking the wheels. Bosch History Blog. Retrieved from https://blog.bosch.com/history/en/2018/09/14/braking-without-locking-the-wheels/, 2018. Accesed: April 03, 2019.

[108] SINGH, K. B., ARAT, M. A., AND TAHERI, S. An intelligent tire based tire-road friction estimation technique and adaptive wheel slip controller for antilock brake system. *Journal of Dynamic Systems, Measurement, and Control*, 135(3):031002, 2013.

[109] SOLYOM, S., RANTZER, A., AND LÜDEMANN, J. Synthesis of a model-based tire slip controller. *Vehicle System Dynamics*, 41(6):475–499, 2004.

[110] STROGATZ, S. H. *Nonlinear dynamics and chaos: with applications to physics, biology, chemistry, and engineering*. Perseus Books, 1994.

[111] SUGAI, M., YAMAGUCHI, H., MIYASHITA, M., UMENO, T., AND ASANO, K. New control technique for maximizing braking force on antilock braking system. *Vehicle System Dynamics*, 32(4-5):299–312, 1999.

[112] TAN, K. K., ZHOU, H. X., AND LEE, T. H. New interpolation method for quadrature encoder signals. *IEEE Transactions on Instrumentation and Measurement*, 51(5):1073–1079, 2002.

[113] TANELLI, M., ASTOLFI, A., AND SAVARESI, S. M. Robust nonlinear proportional-integral control for active braking control systems. In *Proceedings of the 45th IEEE Conference on Decision and Control* (2006), pp. 1745–1750.

[114] TANELLI, M., ASTOLFI, A., AND SAVARESI, S. M. Robust nonlinear output feedback control for brake by wire control systems. *Automatica*, 44(4):1078–1087, 2008.

[115] TANELLI, M., OSORIO, G., DI BERNARDO, M., SAVARESI, S. M., AND ASTOLFI, A. Existence, stability and robustness analysis of limit cycles in hybrid anti-lock braking systems. *International Journal of Control*, 82(4):659–678, 2009.

[116] TERRELL, W. J. *Stability and Stabilization: An Introduction*. Princeton University Press, 2009.

[117] TREUTLER, C. P. O. Magnetic sensors for automotive applications. *Sensors and Actuators A: Physical*, 91(1):2–6, 2001. Third European Conference on Magnetic Sensors & Actuators.

[118] UMENO, T. Estimation of tire-road friction by tire rotational vibration model. *R&D Review of Toyota CRDL*, 37(3):53–58, 2002.

[119] UMENO, T., ONO, E., ASANO, K., ITO, S., TANAKA, A., YASUI, Y., AND SAWADA, M. Estimation of tire-road friction using tire vibration model, 2002. SAE Technical Paper 2002-01-1183.

[120] UNSAL, C., AND KACHROO, P. Sliding mode measurement feedback control for antilock braking systems. *IEEE Transactions on Control Systems Technology*, 7(2):271–281, 1999.

[121] VILLAGRA, J., D'ANDRÉA NOVEL, B., FLIESS, M., AND MOUNIER, H. A diagnosis-based approach for tire–road forces and maximum friction estimation. *Control Engineering Practice*, 19(2):174–184, 2011.

[122] WELLSTEAD, P. E., AND PETTIT, N. B. O. L. Analysis and redesign of an antilock brake system controller. *IEE Proceedings - Control Theory and Applications*, 144(5):413–426, 1997.

[123] WESSEL, K. Bremskraftregler, insbesondere fuer kraftfahrzeuge (brake pressure regulator, particularly for motor vehicles), 1928. Patent no. DE492199C, Germany. Filed: 19/10/1928. Granted: 20/02/1930.

[124] WESTERVELT, E. R., GRIZZLE, J. W., CHEVALLEREAU, C., CHOI, J. H., AND MORRIS, B. *Feedback Control of Dynamic Bipedal Robot Locomotion*. Automation and Control Engineering. CRC Press, 2007.

[125] WORLD HEALTH ORGANIZATION. Save LIVES: a road safety technical package. Retrieved from https://www.who.int/violence_injury_prevention/publications/road_traffic/save-lives-package/en/, 2017.

[126] WORLD HEALTH ORGANIZATION. Global status report on road safety 2018. Retrieved from https://www.who.int/violence_injury_prevention/road_safety_status/2018/en/, 2018.

[127] YI, J., ALVAREZ, L., AND HOROWITZ, R. Adaptive emergency braking control with underestimation of friction coefficient. *IEEE Transactions on Control Systems Technology*, 10(3):381–392, 2002.

[128] ZHANG, J., SUN, W., AND JING, H. Nonlinear robust control of antilock braking systems assisted by active suspensions for automobile. *IEEE Transactions on Control Systems Technology*, 1–8, 2018.

[129] ZHANG, Q. Adaptive observer for multiple-input-multiple-output (MIMO) linear time-varying systems. *IEEE Transactions on Automatic Control*, 47(3):525–529, 2002.

[130] ZHANG, Q. An adaptive observer for sensor fault estimation in linear time varying systems. *IFAC Proceedings Volumes*, 38(1):137–142, 2005. 16th IFAC World Congress.

RÉSUMÉ ÉTENDU DE LA THÈSE

QUELQUES PROBLÈMES DE COMMANDE ET D'ESTIMATION LIÉS AUX SYSTÈMES D'ANTIBLOCAGE DES ROUES

Les accidents de la circulation routière constituent un problème important pour la santé publique et le développement, avec des coûts socioéconomiques significatifs. Selon l'Organisation Mondiale de la Santé, plus de 1,35 million de personnes meurent chaque année dans des accidents de la route, et plus de 50 millions subissent des traumatismes graves. Une cible ambitieuse de réduire ces chiffres de moitié d'ici 2020 a été établie dans le cadre du Programme de développement durable à l'horizon 2030. Les mesures clés à être mises en œuvre pour atteindre la cible incluent : d'établir et de faire respecter des limitations de vitesse et d'autres lois de circulation, de fournir de l'infrastructure sûre pour tous les usagers de la route et d'établir et de faire respecter des réglementations en matière de normes de sécurité des véhicules automobiles. Le déploiement universel des technologies permettant d'éviter un accident ou d'atténuer la gravité des blessures est encouragé, avec un accent sur des systèmes avancés de sécurité active dont l'efficacité est démontrée, tels que le système d'antiblocage des roues (ABS, de l'allemand « antiblockiersystem »).

Introduit par Bosch en 1978 sur les véhicules de série, l'ABS est le socle des systèmes de sécurité active d'aujourd'hui. Son principe d'opération est simple : lors d'une situation de freinage d'urgence, la force du freinage appliquée par le conducteur peut être supérieure à celle que le pneu peut gérer. En conséquence, la roue se bloque et le pneu n'arrive plus à transmettre les forces de traction latérale. Le véhicule devient instable et incontrôlable, puisqu'il ne réagit plus aux commandes de direction exercées par le conducteur au niveau du volant. Par contre, dans un véhicule équipé de l'ABS, des capteurs mesurent la vitesse de rotation des roues et transmettent cette information à l'unité de contrôle de l'ABS. Si cette dernière détecte qu'une ou plusieurs roues sont sur le point de se bloquer, l'ABS intervient pour moduler la pression de freinage sur chaque roue. De cette façon, l'ABS empêche les roues de se bloquer, assurant un freinage en sécurité et, par conséquent, le véhicule reste stable et contrôlable. Généralement, la distance d'arrêt diminue aussi.

Cette thèse aborde trois problèmes liés à l'ABS dans le cadre de la dynamique de la roue : l'estimation de la rigidité de freinage étendue (XBS) des pneus lors du freinage d'urgence, la commande de l'ABS basée sur l'estimation de l'XBS, et l'estimation de la vitesse et de l'accélération angulaires de la roue à partir des

mesures provenant d'un codeur avec des imperfections. L'objectif général de ce travail est de développer des outils visant à améliorer la performance des systèmes de freinage, en utilisant des techniques adaptées de l'automatique non linéaire.

Première partie : Estimation de l'XBS

L'XBS (de l'anglais « extended braking stiffness ») peut être définie comme la dérivée du coefficient de frottement pneu-chaussée par rapport au taux de glissement. Il s'agit d'une généralisation du concept « rigidité de freinage » introduit par Gustafsson, qui est définie comme la pente du coefficient de frottement dans le point de taux de glissement zéro. L'intérêt d'estimer l'XBS provient de son potentiel pour améliorer la conception des algorithmes ABS car, contrairement à la valeur optimale du taux de glissement (c'est-à-dire le taux de glissement pour lequel le coefficient de frottement atteint son maximum) qui est variable et généralement inconnue, la valeur optimale de l'XBS est toujours égale à zéro. L'estimation de cette variable peut servir, par exemple, pour contrôler l'accélération angulaire de la roue et, donc, rendre l'ABS plus robuste aux changements de conditions d'adhérence de la chaussée.

La première partie de la thèse est dédiée à la construction d'un observateur adaptatif pour l'XBS. Nous partons d'un modèle développé dans des travaux précédents dans lequel l'XBS apparaît comme variable d'état et qui est, à son tour, basé sur le modèle de frottement de Burckhardt. Dans ce modèle, on suppose que les paramètres liés aux conditions de la chaussée sont constants mais inconnus. La sortie du système est définie comme la différence entre l'accélération du véhicule et celle de la roue. La vitesse du véhicule est supposée être connue et considérée comme une variable externe du modèle.

Pour concevoir l'observateur on introduit d'abord un changement de coordonnées qui rend le système linéaire dans les paramètres inconnus, ce qui permet l'utilisation des techniques disponibles pour ce type de systèmes. Ensuite, inspiré par les travaux de Zhang [129] et Hoàng et al. [41], on introduit un observateur adaptatif commuté, c'est-à-dire un observateur adaptatif dont les gains d'estimation commutent entre deux valeurs possibles en fonction du signe de la sortie du système. Ce choix permet d'analyser les propriétés de stabilité de l'observateur dans une échelle de temps transformée, dont la dynamique de l'erreur d'observation peut être considérée comme un système commuté. On établit des conditions suffisantes sur les gains de l'observateur qui garantissent que, pour la dynamique de l'erreur d'observation, l'origine est asymptotiquement stable, à condition que le signal de commutation (c'est-à-dire le signe de la sortie du système) ait un temps de maintien minimal. En outre, on établit des conditions qui assurent que le changement d'échelle de temps (qui dépende de la vitesse du véhicule et de la sortie du système) est bien défini et, que s'il existe un temps de maintien minimal dans l'échelle de temps originale, il existera aussi un temps de maintien minimal dans l'échelle de temps transformée. Ces conditions sont synthétisées sous la forme d'hypothèses qui nous semblent raisonnables lors d'une situation de freinage ABS : la pre-

mière est que la vitesse du véhicule est positive, bornée, et séparée de zéro ; la deuxième est que la sortie du système est d'excitation permanente, croise zéro seulement dans des points isolés et chacun de ces points sont séparés par un temps minimal non nul.

Nous avons testé la performance de l'observateur proposé en utilisant des données expérimentales recueillies lors de l'évaluation des algorithmes ABS. Le banc d'essai consiste dans un tambour métallique de 2.5 mètres de diamètre qui tourne sur son axe pour émuler le déplacement du véhicule et un pneu qui roule au-dessus du tambour. Les résultats montrent que l'observateur adaptatif est plus robuste au bruit de mesure et donne une meilleure estimation de l'XBS que les approches précédentes. On a testé la performance de l'observateur en présence des changements de conditions de la chaussée (une perturbation qui ne peut pas être émulée sur le banc d'essai) à travers des simulations numériques. On utilise un modèle du véhicule à deux essieux qui inclue des phénomènes négligés lors de la conception de l'observateur, telles que la dynamique de la suspension, le transfert de charge, et la longueur de relaxation du pneu. De plus, on considère que la vitesse du véhicule est estimée à partir des mesures de la vitesse angulaire des roues et de l'accélération longitudinale du véhicule. Les résultats montrent que, même si la vitesse du véhicule est sous-estimée de 20%, l'observateur fournit encore une estimation raisonnable de l'XBS. Notamment, le passage par zéro de l'estimation coïncide avec celui de la véritable XBS, ce qui est important car cela signifie que l'observateur est capable de détecter correctement lorsque le système passe d'une région du pneu à l'autre.

Deuxième partie : Commande de l'ABS basée sur l'estimation de l'XBS

La deuxième partie de la thèse est dédiée à la conception d'une loi de commande ABS basée sur l'estimation de l'XBS. D'abord, on conçoit une loi de commande continue dont le but est de réguler le système vers l'origine. On montre également via des simulations numériques que, lorsque la sortie du système converge vers zéro, elle ne satisfait pas la condition d'excitation permanente et l'observateur ne converge pas vers les trajectoires réelles du système. On conçoit ensuite une loi de commande hybride dans laquelle la référence d'accélération de la roue est commutée en fonction de la valeur de l'XBS. Le but est de faire converger le système vers un cycle limite autour de zéro afin de faire en sorte que les trajectoires du système satisfassent la condition d'excitation permanente. L'algorithme a deux phases. On suppose que les conditions initiales sont telles que l'accélération de la roue et l'XBS sont négatifs, c'est-à-dire le système est entré dans la région instable du pneu ; s'il va trop loin dans cette région la roue sera bloquée. Pendant la première phase, la référence d'accélération de la roue est mise à une valeur positive ; le but est de faire la roue revenir dans la région stable du pneu. Une fois que l'accélération est positive, l'XBS commence à augmenter jusqu'à ce qu'il traverse un certain seuil qui déclenche l'activation de la phase 2. Pendant la deuxième phase, la référence d'accélération de la roue est mise à une valeur négative ; le but est d'éviter que la roue aille trop loin dans la région stable car cela impliquerait une perte de

force de frottement et donc une augmentation de la distance de freinage. Après le changement du signe de l'accélération, la roue revient dans la région instable du pneu. L'XBS commence à diminuer jusqu'à ce qu'il traverse un seuil qui déclenche de nouveau l'activation de la phase 1.

Pour étudier la stabilité du cycle limite obtenu, on utilise l'application du premier retour de Poincaré, qui transforme l'analyse des orbites périodiques d'un système dans l'analyse de points fixes d'une application. Dans cette première étape, on néglige la dynamique de l'observateur, c'est-à-dire on considère que l'XBS est connue. Pour construire l'application du premier retour on prend la transition où la phase 1 est déclenchée comme l'équivalent d'une section transverse. A partir de cette analyse on obtient des conditions suffisantes pour garantir la stabilité asymptotique du cycle limite.

Nous avons testé la performance de cette loi de commande via des simulations numériques. Les résultats confirment la stabilité asymptotique du cycle limite dans le cas où l'XBS est connue. De plus, dans le cas où l'on utilise l'observateur adaptatif pour estimer l'XBS, les trajectoires du système satisfont la condition d'excitation permanente, l'XBS est donc correctement estimé et le système en boucle fermée atteint une bonne performance lors du freinage. L'analyse de stabilité du cycle limite incluant la dynamique de l'observateur sera réalisée dans des travaux futurs.

Troisième partie : Estimation de la vitesse et de l'accélération angulaires

La technologie la plus courante pour mesurer la vitesse et l'accélération angulaires est basée sur des codeurs incrémentaux. Ceux-ci consistent principalement en une roue dentée (ou un disque à fentes) attachée à l'arbre rotatif et un capteur fixe qui détecte le passage des dents et produit comme sortie un signal carré dont le bord de chaque impulsion correspond au bord d'une dent. Un codeur idéal est caractérisé par des dents (ou fentes) identiques et distribuées de façon équidistante le long de la roue codée. Les codeurs réels ont pourtant des imperfections de fabrication telles que des dents non identiques ou non équidistantes et de l'excentricité de la roue codée par rapport à l'arbre de rotation. Ces imperfections introduisent des variations dans l'emplacement des bords des impulsions qui peuvent être modélisées comme deux perturbations additives indépendantes. Lorsqu'elles sont visualisées le long de la circonférence de la roue codée, les dents non idéales produisent des variations stochastiques à haute fréquence, tandis que l'excentricité de la roue codée produit une variation systématique à basse fréquence. D'ailleurs, comme l'erreur dû aux imperfections est périodique dans une tour mécanique, les mesures de vitesse et accélération contiennent des perturbations périodiques dont la fréquence coïncide avec celle de l'arbre de rotation. La révision de la littérature au sujet de l'enlèvement de ces perturbations montre que, bien que les imperfections des codeurs sont bien connues, juste un petit nombre d'approches qui utilisent des filtres en temps réel ont été proposés, toutes dans le cadre de la commande des véhicules. Ces travaux proposent tous l'utilisation d'un filtre notch pour

atténuer la première composante harmonique des perturbations.

La troisième partie de la thèse est dédiée à la construction d'un algorithme pour estimer la vitesse et l'accélération de la roue permettant d'éliminer les perturbations dues aux imperfections du codeur. D'abord, on introduit trois modèles qui capturent les effets que les imperfections des codeurs ont sur les signaux mesurés. Notre analyse montre que même si l'erreur qui est présente dans la position mesurée peut être négligée selon l'application, ce n'est pas le cas pour les autres signaux. Notamment, la vitesse mesurée contient un terme d'erreur qui est proportionnel à la vitesse réelle, tandis que l'accélération mesurée contient un terme d'erreur qui est proportionnel à l'accélération réelle et un autre qui est proportionnel au carré de la vitesse réelle. En combinant ces modèles avec les caractéristiques de la méthode connue en anglais comme « time-stamping algorithm », on propose un algorithme à trois étapes pour identifier et éliminer les perturbations introduites par les imperfections du codeur. Contrairement aux travaux précédents, dans lesquels juste la première composante harmonique des perturbations est filtrée, par notre approche nous identifions un certain nombre d'harmoniques et nous utilisons cette information pour récupérer des estimations plus fiables de la vitesse et de l'accélération de l'arbre de rotation. Dans la première étape on utilise un filtre passe-haut pour séparer les perturbations à haute fréquence des signaux réels. En utilisant les trois modèles développés et l'algorithme des moindres carrés récursifs, dans la deuxième on identifie les paramètres qui décrivent la sortie de la première étape. Enfin, dans la troisième on utilise ces paramètres pour construire nos estimations.

Nous avons testé la méthode sur un banc d'essai composé de deux moteurs brushless joints par un capteur de couple et un codeur de 60 impulsions-par-tour. Un deuxième codeur de 1024 impulsions-par-tour joint au même arbre de rotation est utilisé comme référence. Les résultats montrent que notre algorithme est capable de réduire de façon significative l'amplitude des composantes harmoniques dues aux imperfections et n'introduit pas des retards perceptibles, contrairement au filtre notch avec lequel seulement la première composante est significativement réduite et qui peut introduire un retard important en fonction du taux d'amortissement du filtre. En utilisant la méthode proposée, il est donc possible d'obtenir avec un codeur à basse résolution des signaux plus lisses et similaires à ceux obtenus avec un capteur à haute résolution.

Dans la partie finale de ce document on présente quelques remarques sur les travaux développés dans cette thèse, ainsi que des perspectives et recommandations pour des travaux futurs de recherche.

université PARIS-SACLAY
ÉCOLE DOCTORALE
Sciences et technologies de l'information et de la communication (STIC)

Titre : Quelques problèmes de commande et d'estimation liés aux systèmes d'antiblocage des roues

Mots clés : ABS, rigidité de freinage étendue, codeurs incrémentaux, systèmes commutés, observateur adaptatif, contrôleur hybride

Résumé : Cette thèse aborde trois problèmes liés à l'ABS dans le cadre de la dynamique de la roue : l'estimation de la rigidité de freinage étendue (XBS) des pneus lors du freinage d'urgence, la commande de l'ABS basée sur l'estimation de l'XBS, et l'estimation de la vitesse et de l'accélération angulaires de la roue à partir des mesures provenant d'un codeur avec des imperfections. L'objectif général de ce travail est de développer des outils visant à améliorer la performance des systèmes de freinage, en utilisant des techniques adaptées de l'automatique non linéaire.
La première partie de la thèse est consacrée à la construction d'un observateur adaptatif commuté pour l'XBS, c'est-à-dire un observateur adaptatif dont les gains d'estimation commutent entre deux valeurs possibles en fonction du signe de la sortie mesurée du système. La stabilité de l'observateur est analysée en utilisant des outils pour des systèmes commutés et en cascade, ainsi que des concepts tels qu'excitation permanente et transformations singulières d'échelle de temps.
La deuxième partie de la thèse est dédiée à la conception d'une loi de commande pour l'ABS. L'objectif de contrôle est formulé en termes de l'XBS et une loi de commande hybride est conçue afin de faire en sorte que les trajectoires du système satisfassent les conditions requises pour l'estimation de l'XBS. La stabilité du contrôleur est analysée en utilisant l'application de Poincaré.
La troisième partie de la thèse aborde la construction d'un algorithme pour estimer la vitesse et l'accélération angulaires de la roue et éliminer des perturbations qui sont introduites par les imperfections du codeur, et dont l'amplitude et la fréquence sont une fonction de la position, la vitesse, et l'accélération angulaires (réelles) de la roue. L'algorithme est basé sur la méthode connue comme « time-stamping algorithm », ainsi que sur des techniques de filtrage est d'estimation de paramètres.
Des essais expérimentaux et des simulations numériques illustrent la bonne performance des algorithmes d'estimation et de contrôle présentés dans cette thèse. Dans tous les cas nos résultats sont comparés par rapport à l'état de l'art.

Title: On control and estimation problems in antilock braking systems

Keywords: ABS, extended braking stiffness, incremental encoders, switched systems, adaptive observer, hybrid controller

Abstract: This thesis addresses three problems related to the antilock braking system (ABS) in the context of the wheel dynamics: the estimation of the tyre extended braking stiffness (XBS) during an emergency braking situation, the control of the ABS based on the estimation of the XBS, and the estimation of the angular velocity and acceleration of the wheel from the measurements of an incremental encoder with imperfections. The general objective of this work is to develop tools aimed at improving the performance of braking systems by using techniques adapted from nonlinear control theory.
The first part of the manuscript is devoted to the construction of a switched adaptive observer for the XBS, that is, an adaptive observer whose estimation gains switch between two possible values based on the sign of the system's measured output. The stability of the observer is analyzed using tools for switched and cascaded systems, as well as concepts such as persistency of excitation and singular time-scale transformations.
The second part of the manuscript is dedicated to the design of a control algorithm for the ABS. The control objective is formulated in terms of the XBS and a hybrid controller is designed so that the trajectories of the system satisfy the conditions required for the estimation of the XBS. The stability of the controller is analyzed using the Poincaré map.
The third part of the manuscript focuses on the construction of an algorithm to estimate angular velocity and acceleration of the wheel and remove perturbations which are introduced by the encoder imperfections and whose amplitude and frequency are a function of the wheel's (real) position, velocity, and acceleration. The algorithm is based on the method known as time-stamping algorithm, as well as filtering and parameter estimation techniques.
Experimental tests and numerical simulations illustrate the good performance of the estimation and control algorithms presented in this thesis. In all cases our results are compared with respect to the state of the art.

Université Paris-Saclay
Espace Technologique / Immeuble Discovery
Route de l'Orme aux Merisiers RD 128 / 91190 Saint-Aubin, France